Anuja Sahasrabudhe

Raman Scattering on α-$RuCl_3$ Under High Magnetic Fields

Suprises of the field induced phase

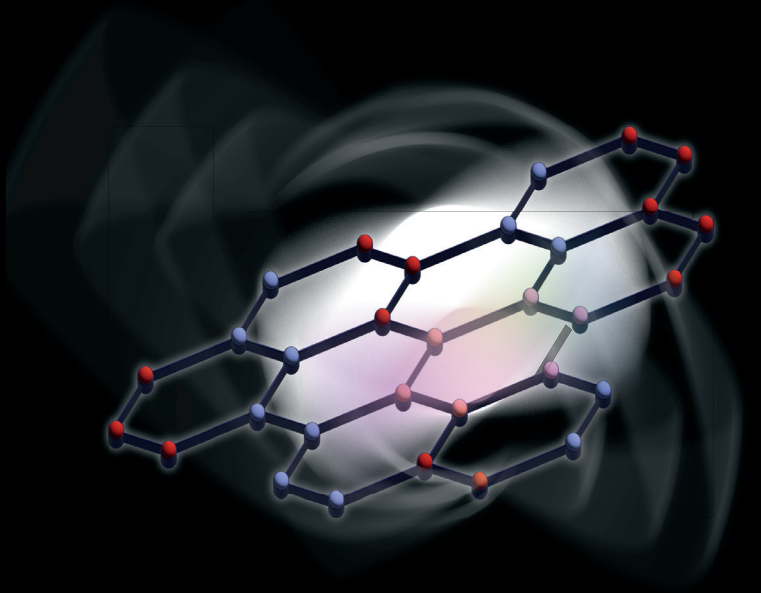

Raman scattering on α-$RuCl_3$ under High Magnetic fields

surprises of the field-induced phase

Inaugural-Dissertation

zur

Erlangung des Doktorgrades

der Mathematisch-Naturwissenschaftlichen Fakultät

der Universität zu Köln

vorgelegt von

Anuja Sahasrabudhe

aus

Ratlam, India

October 2023, Köln

Berichterstatter: Prof. Dr. Paul H. M. van Loosdrecht
Prof. Dr. Fulvio Parmigiani
Prof. Dr. Peter Schilke

Tag der Mündlichen Prüfung: January 19 2024

in memory of my dearest aunt
Alka Keshav Sahasrabudhe

"Nothing in life is to be feared; it is only to be understood."

- Marie Curie

CONTENTS

1 Introduction **1**
- 1.1 The Birth of Condensed matter . . . 1
- 1.2 Phase Transitions . . . 2
- 1.3 Kitaev Quantum Spin Liquid & α-$RuCl_3$ . . . 5

2 Kitaev Quantum Spin Liquid and α-$RuCl_3$ **11**
- 2.1 Kitaev Model . . . 11
- 2.2 Jackeli & Khaliullin's mechanism . . . 13
- 2.3 α-$RuCl_3$ . . . 17
  - 2.3.1 Structural properties . . . 17
  - 2.3.2 Electronic properties . . . 19
  - 2.3.3 Magnetic properties . . . 20
  - 2.3.4 Stacking faults . . . 22

3 Raman scattering **25**
- 3.1 Macroscopic introduction . . . 27
- 3.2 Microscopic introduction . . . 28
- 3.3 Group theoretical approach . . . 30
- 3.4 Excitations observed in Raman spectra . . . 32
  - 3.4.1 Phonons . . . 32
  - 3.4.2 Electrons . . . 33
  - 3.4.3 Magnons . . . 34
    - 3.4.3.1 Elliott-Loudon scattering . . . 34
    - 3.4.3.2 Fleury-Loudon scattering . . . 37
  - 3.4.4 Majorana fermions . . . 38

3.5 Raman scattering from chiral excitations . . . 39
3.5.1 Raman optical activity . . . 41
3.5.1.1 ROA in anti-ferromagnets . . . 42
3.6 Raman scattering from magnetically ordered systems . . . 43
3.6.1 Example: CrI_3 . . . 47
3.7 Experimental details . . . 49

4 Low temperature crystal structure of α-$RuCl_3$ 53
4.1 Group theoretical study . . . 55
4.2 Experimental details . . . 59
4.3 Results and discussions . . . 59
4.3.1 Polarization dependence . . . 59
4.3.2 Azimuthal dependence . . . 61
4.3.3 Magnetic point group . . . 62
4.4 Conclusion and summary . . . 65

5 The high-field quantum disordered state 67
5.1 Experimental details . . . 67
5.2 Results and discussions . . . 68
5.2.1 Low temperature ordered phase . . . 69
5.2.2 Excitations of the field polarized limit . . . 70
5.2.2.1 Spin-flip excitation M1 . . . 72
5.2.2.2 Multi-particle excitations M2 and M3 . . . 73
5.2.3 Exact Diagonalization . . . 74
5.2.4 Summary and conclusions . . . 76

6 Chiral excitations in the field-induced phase 79
6.1 Experimental details . . . 81
6.2 Results . . . 81
6.2.1 Helicity dependence . . . 82
6.2.2 Temperature dependence . . . 83
6.3 Discussions and conclusions . . . 85

7 Phonons in the field-induced phase 89
7.1 Results & discussion . . . 90
7.1.1 Chiral phonons . . . 90
7.1.2 Phonon-M3 hybridization . . . 94
7.2 Conclusion & Outlook . . . 96

8 Non-reciprocal excitations 99
8.1 Experimental details . . . 100

8.2 Experimental results 101
8.2.1 Phonon $\boldsymbol{\alpha}$ (116 cm^{-1}) 101
8.2.2 M1 103
8.3 Discussions and conclusions 103

9 Conclusions **107**

Appendix I **111**

Appendix II **113**

Appendix III **117**

Appendix IV **125**

Bibliography **129**

Acknowledgements **143**

Erklärung zur Dissertation **145**

1 INTRODUCTION

1.1 The Birth of Condensed matter

Ever since the dawn of humanity, light has been recognized as being an entity integral to our existence. It regulates our circadian rhythm, assists plants with photosynthesis, supports all life on earth, and through its interaction with matter makes the universe the colorful place that we know it to be. In the modern age it is a tool for the military, for espionage, for entertainment and for communication — a revolution that has been shaped by the insatiable human curiosity to understand the mysterious character of light. In fact, it is in no way an exaggeration to say that some of the biggest developments in physics have been motivated directly by considerations of light or its interaction with matter. The theory of mirrors and lenses was in this journey, to wit, merely a beginning — a beginning of what would ultimately unify the radiation from an antenna, to the radiation from the sun, to the cosmic microwave background radiation that fills out the eternal void of an ever expanding universe!

As the early practitioners quibbled over the particle vs wave character of light, it was only natural that the worldview of physicists see-sawed between the two extremes. Newton (1643-1727), the foremost authority in the early days of modern science, believed light to be composed of "corpuscles" or particles. Such was his dominance that it was not until the 19th century that the wave theory of diffraction received mainstream acceptance [1]. Once the wave theory did get universal acceptance, the subsequent investigations of the photoelectric effect and the blackbody radiation in the twentieth century took the wave theory by storm and resurrected the age old debate about the true nature of light. Indeed it was then that we saw the revolutions of *quantum mechanics and special relativity* reshape our understanding of light. In doing so we have now come to appreciate how wave-particle duality is at the very heart

of a quantum field, and that matter and photons are but mere manifestations of the oscillations of their respective underlying quantum fields.

Amidst these great conceptual developments that helped unravel the mechanism behind light matter interactions, the advances in spectroscopy firmly established light as an investigative probe to study excitations in matter. One of these techniques is *Raman scattering* [2], for which its inventor C. V. Raman was awarded the Nobel Prize in 1930. In contrast to Rayleigh scattering in which light scatters elastically, Raman scattering is essentially a technique of probing excitations in matter by observing the changes in frequency of the incident light. The Raman spectrum of the scattered light thus provides vital information about the existence of excitations, their energy and with some cleverness even the associated symmetries and the selection rules, and it is this technique that will be our workhorse.

Historically, quantum mechanics was born out of the necessity of explaining atomic phenomena. By design it excelled where the classical theory failed: in explaining atomic structure, the hydrogen spectrum, the photoelectric effect, the selection rules for dipole radiation etc., to name just a few. While the theory upset the deterministic worldview of the classical physicists, it lent itself as a promising alternative to explaining the properties of an assortment of bazillions of particles from microscopic principles and some clever phenomenological guesswork. This initial pursuit acquired the moniker *Solid State Physics* as quantum mechanics explained the electrical and thermal properties of crystalline objects, and even the nature of the simplest magnets. Soon, however, it was clear that the solid state physicists were dealing with more than just the "solid state". In particular, they were interested in uncovering different phases that a material could host in its phase diagram. While for water this could be the visually well-known solid, liquid and gas phases, for other materials it could be the metallic, insulating, superfluid or even the superconducting phase! The condensation of materials into different phases became such a rich study in its own right that one of the most prolific quantum many body theorists, Philip Anderson, eventually coined the term *Condensed Matter* to capture the diversity of the phenomena at hand [3].

1.2 Phase Transitions

Landau's Scheme

Understanding condensation phenomena has long been an exciting venture for quantum many body physicists. In the early days of the field, Lev Landau developed a scheme to explain second order condensation phenomena

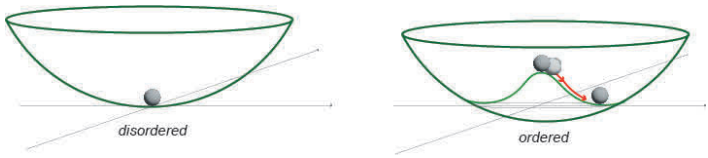

Figure 1.1: Sketch showing the dependence of free energy on order parameter. In the ordered phase the free energy of the system resembles a 'Mexican hat' or a 'wine-bottle bottom'. The shape of the potential compels the order parameter to take a non-zero value at the bottom of the valley. In the spontaneous symmetry broken state the ground or lowest-energy state does not share the symmetry of the underlying Hamiltonian. Instead, there exists a whole family of ground states represented by different points on the circle. The symmetry breaking is spontaneous in the sense that we cannot predict which of these ground states will be chosen.

from an ordered phase to disordered phase through the idea of a local *order parameter* [4]. The order parameter is expected to take non-zero values in the ordered phase while it averages to zero in the disordered phase. This simple observation unifies a multitude of seemingly disparate phenomena — ranging from crystallinity to superfluidity to superconductivity to ferromagnetism — with the view that the system develops long range order as it settles into a symmetry broken state. The ground state essentially breaks the global symmetries of the Hamiltonian and the system randomly chooses one of the energy minima. In quantum magnets this specifically allows for the possibility of different kinds of magnetic ordering, each one defined by its own broken symmetry (see Fig.1.1).

Beyond the Landau paradigm: Quantum Spin Liquids

While the Landau paradigm was a guiding star for understanding many order-disorder phase transitions, the possibility of the appearance of a different phase via a mechanism that would circumvent the Landau classification was merely a curiosity until Anderson came up with the idea of *Resonating Valence Bond* (RVB) theory (1973). In an attempt to guess the ground state of a spin-$^1/_2$ antiferromagnet on a triangular lattice (as shown in Fig.1.2(a)) [5], Anderson reasoned that much like the Benzene ring visualizations with alternating single and double bond structures (popularized by Linus Pauling), the frustration arising from the lattice structure could lead to a non-degenerate ground state of multiple spin configurations (see Fig.1.2). This would let the ground state retain the global symmetry of the Hamiltonian. Unfortunately for Anderson, this idea of a *quantum spin liquid* (QSL) is not realised in the

original model, as was shown later by Huse and Elser [6] (see Fig.1.2(b)). However, modifications of the original model, either by introducing additional neighbor interactions [7] or spin anistropy [8] can lead to quantum spin liquid states in theory. The distinguishing feature of these states is the lack of ordering in such a spin liquid down to zero temperatures, the high degree of entanglement in the resulting ground state and the fact that such massively entangled ground states can support truly non local excitations, e.g. *spinons*, with fractional spin excitations. Although one may accuse the hypothesis of such spin-liquid states to be highly conjectural and speculative, we already have an electronic prototype of these spin-liquid states — the quantum Hall states — that defy the Landau paradigm and possess emergent topological quasiparticles with anyonic statistics. It is thus only natural that the properties of the corresponding spin analogs and their experimental detection have now become a topic of intense scrutiny.

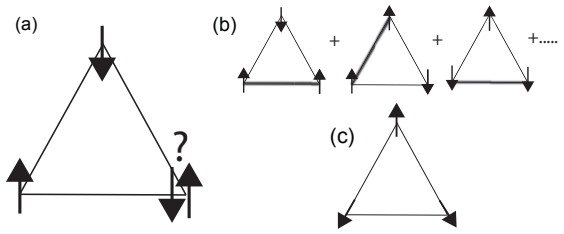

Figure 1.2: (a) System of $S = 1/2$ antiferromagnet on a triangular lattice. At first glance, the system exeplifies geometric frustration as the there is no trivial way in which the spin on the third site can be aligned while satisfying the requirement of antiferromagnetic nearest-neighbor interaction with the other two spins. (b) Anderson's idea of the ground state: a non-degenerate state of multiple spin configurations leading to a quantum spin liquid [5] (the thick line represents the frustrated bond). (c) Ground state identified by Huse and Elser: a magnetically ordered state with every spin oriented at an angle of 120° to one another [6].

One of the earliest analyses in this regard was by Anderson & Baskaran when in 1987 they revived Anderson's RVB theory in the context of Mott insulators as a model for high-Tc superconductors [9]. As the name suggests, in a Resonating Valence bond state, two valence electrons share a covalent bond and form a spin singlet with $S = 0$. This grouping of the electrons into pairs of two forming the singlets is not unique, and under certain conditions, the system switches back and forth (resonates) between different singlet configurations. In such a magnetic system, the net magnetization remains zero and the fluctuations persist to zero temperature resulting in a QSL. Kivelson,

Rokhsar, and Sethna investigated the excitations above the Resonating Valence Bond state and, to their surprise, they found that the excitations above the spin-liquid state had reversed charge-statistics relations in the form of neutral spin-1/2 fermions and spinless bosons with charge $\pm e$ [10]. These works led to an explosion of interest in ascertaining the theoretical validity of the idea of quantum spin liquids and soon afterwards models of $\mathbb{Z}_2$ spin liquids were constructed [11–13]. These models were shown to possess stable low energy effective field theory descriptions in terms of their emergent gauge groups. Additionally, Kitaev came up with two exactly solvable models of a $\mathbb{Z}_2$ spin liquid — the toric code [13] (1997) and the honeycomb model [14] (2006), based on which multiple subsequent works have further demonstrated the existence of many spin liquids with different group structures in both 2 and 3 space dimensions [15–17].

1.3 Kitaev Quantum Spin Liquid & α-$RuCl_3$

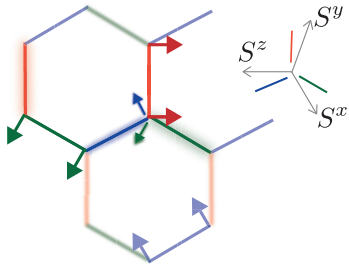

Figure 1.3: The $S = 1/2$ spins on a honeycomb lattice with bond dependent Ising interactions. The blue, green and red bonds have the Ising easy-axes parallel to the x, y or z axes respectively. Each site has six possible spin directions from three easy-axes of the Ising spins. For such a system, only one of the bonds is satisfied and other two bonds become frustrated.

Among the theoretical models for quantum spin liquids, the Kitaev honeycomb model [14] will be of special interest to us. It has the Hamiltonian:

$$\mathcal{H} = \sum_{\langle i,j \rangle} -J^x S_i^x S_j^x - J^y S_i^y S_j^y - J^z S_i^z S_j^z, \tag{1.1}$$

involving nearest-neighbor pairs $\langle i, j \rangle$ of $S = 1/2$ quantum spins on a 2D-honeycomb lattice (see Fig.1.3). Surprisingly, despite the anisotropic interac-

tions between nearest neighbors, there exists an exact solution of the spectrum of this Hamiltonian and the emergent excitations can be shown to be Majorana fermions and spinless bosons (visons). Moreover, the emergent Majorana fermions have anyonic statistics allowing them to be braided, i.e. the Majorana fermions can continue to retain information even as their worldlines are wrapped around one another like hair in a braid. Furthermore, due to the robustness of these excitations against local perturbations, they have been proposed as a viable means of implementing fault tolerant topological quantum computation.

We next turn to the question of being able to observe Kitaev physics in the laboratory. A promising avenue here is one proposed by Jackeli and Khaliullin for the realization of the Kitaev model using $j_{\text{eff}} = 1/2$ pseudospins in $SrIr_2O_3$ [18]. This work mobilized search efforts for a QSL phase and hidden Majorana fermions in a family of iridium and ruthenium compounds [19]. Subsequently, in the course of these studies, α-$RuCl_3$ was also identified as a potential candidate [20] for observing spin-liquid behavior. As it turns out, α-$RuCl_3$ is going to be the protagonist of this thesis — much of this thesis will be dedicated to elucidating the properties of α-$RuCl_3$ and its excitations with the aid of Raman scattering, and to find out to what extent the QSL dream is realised!

In the light of Jackeli and Khaliullin's seminal work, the following properties of α-$RuCl_3$ stand out and make it a promising candidate for the realization of spin-liquid physics:

- Lattice structure: α-$RuCl_3$ crystallizes in a layered honeycomb lattice structure, where each $RuCl_3$ layer consists of edge-sharing $RuCl_6$ octahedra arranged in a honeycomb lattice. The edge sharing arrangement is an essential ingredient of Jackeli and Khaliullin's recipe – it is responsible for suppressing the isotropic Heisenberg interaction and in supporting anisotropic, bond-direction dependent exchange. Furthermore, weak interlayer interactions can lead to the emergence of two-dimensional physics in the α-$RuCl_3$ layers and the octahedral crystal field can support the formation of an effective spin-$1/2$ honeycomb lattice.
- Effective $j = 1/2$: Kitaev's exactly solvable model [14] is a model of $S = 1/2$ spins on a honeycomb lattice. In α-$RuCl_3$, the combination of an octahedral crystal field, spin-orbit coupling, and electronic correlations lead to the emergence of effective spin-$1/2$ degrees of freedom on the Ru atoms' d-orbitals [21].
- Magnetic Frustration: The magnetic interactions between the ruthenium ions in α-$RuCl_3$ are dominated by exchange interactions that are bond-

dependent. The interactions are such that it is not possible for all the spins in the honeycomb lattice to align in a way that all the three bonds are simultaneously satisfied. At low temperatures, this could lead to a highly degenerate and disordered ground state capable of exhibiting spin-liquid traits.

It must be noted however that α-$RuCl_3$ does still possess isotropic Heisenberg and anisotropic Γ interactions. In fact, they are so strong that at extremely low temperatures they cannot be treated as perturbations to the Kitaev terms and must be explicitly listed in the Hamiltonian. These exchange interactions hinder a pure Kitaev spin liquid phase and make the system order antiferromagnetically below ∼7 K at field strengths lower than ∼7 T [22–24]. This is seemingly a ubiquitous issue that plagues most known Kitaev QSL candidates [25] and largely precludes the possibility of a pure QSL phase in real materials. With this caveat in mind, we can optimistically anticipate only a *proximate* Kitaev Quantum Spin liquid that does not extend down to zero temperatures.

The next challenge is the experimental identification of a QSL phase. Even if one could engineer a pure Kitaev system with no additional interactions, there is no well-established way of checking a unique signature to confirm the presence of a QSL or lack thereof. Therefore, the problem of detecting a Kitaev QSL phase is two-fold:

1. Stabilizing a proximate QSL by reducing the effects of other interactions.
2. To design experiments that might capture the signatures of a QSL phase.

In spite of these difficulties, several experimental studies have reported on signatures of fractionalized excitations in α-$RuCl_3$, potentially hinting towards the presence of an underlying quantum spin liquid phase. This has been achieved in at least two different ways: (a) temperature tuning and (b) magnetic field tuning.

The temperature tuning experiments (Fig.1.4(a)) have mapped the specific heat data of α-$RuCl_3$, which exhibits a two-stage release of magnetic entropy that is characteristic of localized and itinerant Majorana fermions [26, 27]. Additionally, neutron [26, 28, 29] and Raman scattering (Fig.1.4(b)) [30] experiments on α-$RuCl_3$ detect a broad continuum. The temperature dependence of this continuum has been found to be fermionic in nature [31] (Fig.1.4(c)). The continuum measured with neutron scattering resembles a star-like shape in momentum space, in agreement with the theoretically calculated spectrum of the Kitaev-Heisenberg model [29] (Fig.1.4(d)).

Remarkably, magnetic field tuning (Fig.1.5(a)) has emerged as the most effective tool in studying the elusive spin-liquid phase. Experiments like electron

spin resonance [32], neutron-scattering [24] and terahertz absorption [33] have detected a rich spectrum consisting of multiple excitations that emerge from the continuum upon suppression of the low temperature antiferromagnetic phase (see example in Fig.1.5(b)). Most notably, the spectrum exhibits a gapped continuum and multiple discrete excitations split-off from the continuum [32, 33]. Due to their conspicuously distinct field dependence, these emergent excitations have been interpreted as a signature of multi-particle excitations and/or bound states of fractionalized excitations. These speculations have been further bolstered by structure factor calculations that predict the emergence of Majorana bound states in the field-induced regime of a Kitaev Quantum Spin Liquid [34].

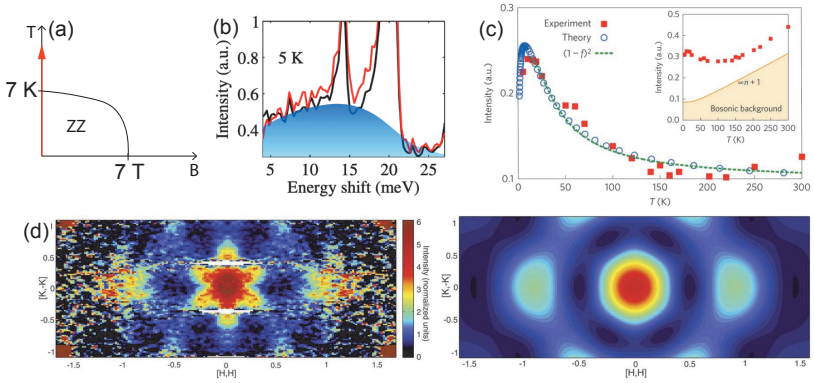

Figure 1.4: (a) Sketch of the phase diagram emphasizing temperature tuning. (b) Broad continuum observed in Raman scattering by Sandilands et al [30]. Reprinted with permission from the American Physical Society, Ref.[30] © 2015 American Physical Society. (c) Experimentally observed temperature dependence of the continuum and the theoretically calculated temperature dependence of the fermions by Nasu et al [35]. Reprinted with permission from Springer Nature, Ref.[35]. ©2016 Springer Nature. (d) Neutron scattering measurements by Banerjee et al [29]. The left plot shows a broad star shaped continuum measured at 5 K integrated between 4.5 meV to 7.5 meV. The right plot shows the expected scattering from an isotropic antiferromagnetic Kitaev mode from [29]. Reprinted with permission from AAAS.

The most striking among these experiments to this date – and also the most controversial – is the experiment by the group of Yuji Matsuda [36]. They report the observation of a half-integer Thermal Quantum Hall Effect (TQHE) in α-$RuCl_3$ between 7 and 9 T and up to ∼5.6 K (Fig.1.5(c)). The TQHE is a

phenomenon related to the behavior of heat conduction in a two-dimensional electron system subjected to a strong magnetic field. It is analogous to the conventional quantum Hall effect observed in the electrical conductivity of such systems. However, as α-$RuCl_3$ is a Mott insulator, transverse heat conductivity is measured instead of the electrical conductivity. The quantized conductance demonstrates that heat is carried by chiral edge modes ensuring that the heat flows in one direction along the edge of the sample, similar to the electrical current in the conventional quantum Hall experiment. The presence of the half-integer plateau in the TQHE signifies the fractionalized nature and the spin-1/2 character of its Majorana carriers. This observation for all practical purposes would settle the question in favor of the Kitaev spin liquid ground state [31, 37, 38]. Unfortunately, replication of the claimed Topological Quantum Hall Effect (TQHE) and the proposed explanations of the effect have forever remained embroiled in controversy, and there is still no consensus on the effect or its interpretation.

Nonetheless, the multitude of experiments described above demonstrate the existence of one or more phases that is/are unusual and filled with exotic excitations. In our experiments we will tune the external magnetic field in an attempt to engineer an encounter with at least one such phase. We already know that spectroscopic tools such as electron spin resonance [32] and terahertz absorption [33] have helped unveil a rich spectrum with a gapless continuum and sharp excitations in α-$RuCl_3$. Our hope then is that our spectroscopic workhorse – the Raman scattering technique – will further shed "light" on the phases that α-$RuCl_3$ can potentially host as we tune the external field. The novelty of our set-up would be in the choice of the polarizations of the incident and the scattered light – and as we shall see through the course of this thesis, tuning this experimental setting will provide irrefutable spectroscopic evidence in favor of chiral excitations within a certain range of magnetic fields.

In order to describe these findings, we provide an overview of the necessary technical background in Chapters 2 and 3, while Chapters 4-8 will encapsulate our main results. So, without further delay, we set course for a fascinating exploration of the exotic physics of α-$RuCl_3$!

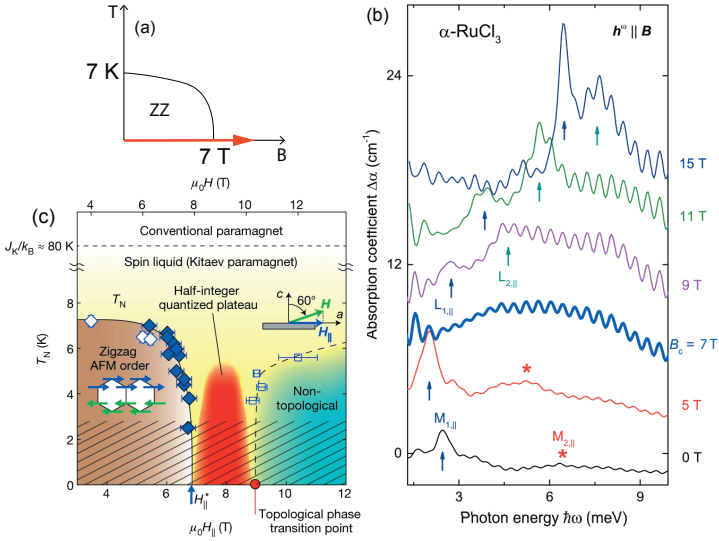

Figure 1.5: (a) Sketch of the phase diagram emphasizing magnetic field tuning. (b) THz absorption data from Zhe Wang et al [33]. The spectrum shows two antiferromagnetic magnons (M_1, M_2) for $B < B_c$ and unconventional features (L_1, L_2) for $B > B_c$. Reprinted with permission from the American Physical Society, Ref.[33]. © 2017 American Physical Society. (c) Phase diagram obtained from the thermal conductivity measurements by Kasahara et al [36]. Reprinted with permission from Springer Nature, Ref.[36]. ©2018 Springer Nature.

2 KITAEV QUANTUM SPIN LIQUID AND α-$RuCl_3$

The Kitaev model provides a route to realise the long sought after Majorana fermions in a quantum many body system [14]. We have already pointed out in the INTRODUCTION that in this context α-$RuCl_3$ holds great promise to replicate the physics of the Kitaev model in the laboratory [18, 21]. This chapter introduces the details of the Kitaev model and elucidates Jackeli and Khaliullin's mechanism to find materials with predominantly bond-direction-dependent interactions. Finally, we will introduce the material α-$RuCl_3$ by discussing its structural, magnetic, and electronic properties.

2.1 Kitaev Model

The setting for the Kitaev model [14] that we are interested in is as follows: the spin-$1/2$ reside at the lattice points of a 2D honeycomb lattice. In this model, every lattice site has three nearest neighbors resulting in three distinct flavors for the interactions, one along each bond direction. The interaction between the nearest neighbors is highly anisotropic and depends on the bond direction, i.e., along the bond the spins shows Ising like interactions. This results in the following Hamiltonian:

$$\mathcal{H} = \sum_{\langle i,j \rangle} -J^x S_i^x S_j^x - J^y S_i^y S_j^y - J^z S_i^z S_j^z \,, \tag{2.1}$$

where the summation extends over all nearest-neighbor pairs $\langle i, j \rangle$ on the lattice.

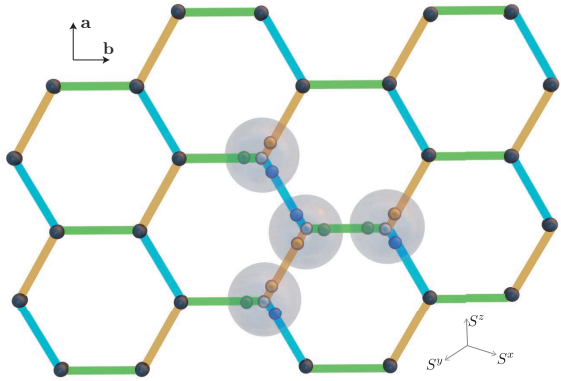

Figure 2.1: Kitaev's model on a honeycomb lattice. Each color represents a distinct coupling strength between the nearest neighboring spins (black dots). This model can be exactly solved by representing every spin by four Majorana fermions.

We can represent each spin in terms of four Majorana fermions $\{b^x, b^y, b^z, c\}$, such that $S^\alpha = ib^\alpha c$ where $\alpha = x, y, z$. It is easy to verify that this preserves the commutation relations between the spin operators. Fig.2.1 pictorially shows how the spin splits into four Majorana fermions and the different colored bonds show anisotropic bond-direction dependent interactions.

Upon performing the substitution, the Hamiltonian reduces to:

$$\mathcal{H} = \frac{-i}{4} \sum_{\langle i,j \rangle} \langle u_{ij} \rangle c_i c_j \tag{2.2}$$

where $u_{ij} = ib_i^\alpha b_j^\alpha$ represents the link between the sites i and j. As the u_{ij}'s are constants of motion, they can be replaced by their expectation values. The Hamiltonian in terms of Majorana fermions (c_i, c_j) is then a simple quadratic Hamiltonian and its spectrum can be found by exact diagonalization.

Fig.2.2(a) illustrates the phase diagram, as calculated by Kitaev, for different strengths of the interactions J^x, J^y, and J^z. Depending on these interaction strengths, the spin-liquid phase can be either gapless or gapped. The gapped phases ($\boldsymbol{A}_x$, $\boldsymbol{A}_y$, and $\boldsymbol{A}_z$) are associated with excitations that exhibit Abelian anyonic behavior. On the other hand, phase $\boldsymbol{B}$ is characterized by gapless fermions. Nonetheless, gapless phase $\boldsymbol{B}$ acquires a gap under an external magnetic field that breaks the time-reversal symmetry. Under these conditions, the emergent excitations in phase $\boldsymbol{B}$ transform into non-Abelian anyons [14].

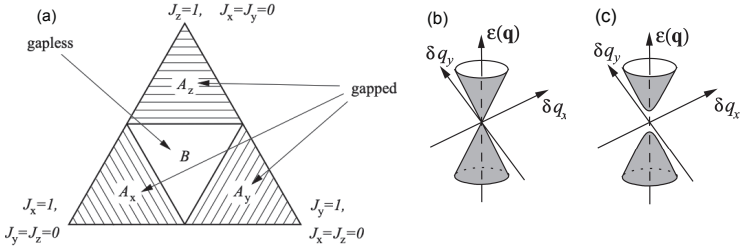

Figure 2.2: (a) Phase diagram of the model. Dispersion of Majorana fermions in (b) the gapless phase, and (c) the gapped phase. Figures are adapted and reprinted with permission from Elsevier, Ref.[14]. © 2006 Elsevier.

2.2 Jackeli & Khaliullin's mechanism

The most general exchange Hamiltonian in materials with dominant nearest neighbor spin interactions can be written as [39]:

$$\mathcal{H} = \sum_{<i,j>} J_{ij}\mathbf{S}_i \cdot \mathbf{S}_j + \mathbf{D}_{ij} \cdot (\mathbf{S}_i \times \mathbf{S}_j) + \mathbf{S}_i \cdot \mathbf{\Gamma}_{ij} \cdot \mathbf{S}_j \,, \tag{2.3}$$

where J_{ij} is the Heisenberg coupling, $\mathbf{D}_{ij}$ is the Dzyaloshinskii-Moriya vector and $\mathbf{\Gamma}_{ij}$ is the pseudo-dipolar tensor [39].

A pure Kitaev model necessitates the vanishing of J_{ij}, $\mathbf{D}_{ij}$, and all elements of $\mathbf{\Gamma}_{ij}$ except for the component $\Gamma^{\mu\mu}$ pertaining to a specific bond $\mu = \{x, y, z\}$. This condition places significant constraints on the couplings.

How can we streamline our search for materials that can come close to obeying these conditions? Here George Jackeli and Giniyat Khalliulin offer their insights and provide a plausible route. In order to identify candidate materials that could possess anisotropic Kitaev interactions, they consider the role of strongly spin-orbit coupled Mott insulators with octahedral crystal fields and d^5 electrons in enabling the Kitaev interactions. The energy level scheme of d^5 ionic systems under octahedral crystal fields and strong spin-orbit coupling is shown in Fig.2.3. Crystal field splitting lifts the degenerate energy levels of the d-orbital into $3t_{2g}$ and $2e_g$ levels. Spin-orbit coupling further lifts the t_{2g} level into states with angular momentum $j_{\text{eff}} = \frac{1}{2}$ and $j_{\text{eff}} = \frac{3}{2}$*. Strong elec-

*Due to its three degenerate energy levels, the t_{2g} orbital is treated as a p-orbital, but with $l_{\text{eff}} = -1$. The negative sign of the orbital angular momentum changes the energy

tronic correlations U open up a Fermi gap in the $j_{\text{eff}} = \frac{1}{2}$ state, transforming the material into a Mott insulator (see Fig.2.3).

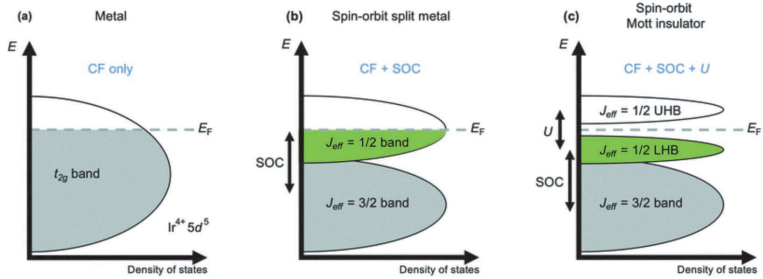

Figure 2.3: Band structure of spin-orbit coupled Mott insulators [41]. Reprinted from Ref.[41] under a Creative Commons Attribution 4.0 International (CC BY 4.0) license. ©2021 Browne et al.

The $j_{\text{eff}} = \pm\frac{1}{2}$ states can be expressed as as superposition of states involving orbital angular momentum $l^z = 0$ and $l^z = \pm 1$, as well as spin states $|\uparrow\rangle$ and $|\downarrow\rangle$. Within the t_{2g} orbital set, consisting of xy, xz, and yz orbitals, the states are defined as follows:

- $|l_z = 0\rangle \equiv |xy\rangle$
- $|l_z = \pm 1\rangle \equiv -\frac{1}{\sqrt{2}}(|ixz\rangle \pm |yz\rangle)$.

Therefore, the $j_{\text{eff}} = \pm\frac{1}{2}$ states can be represented as [18][39]:

$$\left|j_{\text{eff}} = +\frac{1}{2}\right\rangle = \frac{1}{\sqrt{3}}(-|xy,\uparrow\rangle - |yz,\downarrow\rangle - i|xz,\downarrow\rangle)$$

$$\left|j_{\text{eff}} = -\frac{1}{2}\right\rangle = \frac{1}{\sqrt{3}}(|xy,\downarrow\rangle - |yz,\uparrow\rangle + i|xz,\uparrow\rangle)$$

Fig.2.4 shows the density distribution of $|j_{\text{eff}} = +\frac{1}{2}\rangle$ state in real space.

The alignment of orbitals with spins leads to a peculiar distribution of spin densities in real space and transfers the bond-directional nature of the orbitals into that of the pseudo-spins. The bond-geometry therefore plays a significant role in determining the exchange-mechanism.

Next, we delve into the role of bond geometry. Of particular interest here are the octahedral structures, denoted as MO_6 (M : metal, O : ligand), that

of the $j_{\text{eff}} = \frac{1}{2}$ and $j_{\text{eff}} = \frac{3}{2}$ states. See Ref. [19] and [40] for more details.

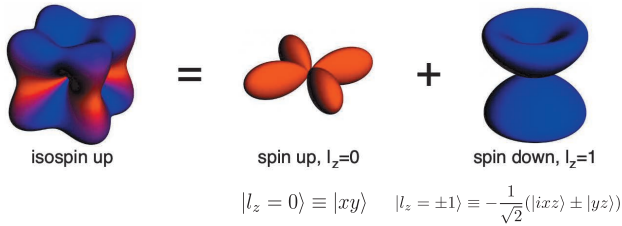

Figure 2.4: Spatial distribution of spins due to strong spin-orbit coupling [18]. Reprinted figure with permission from the American Physical Society, Ref.[18]. © 2009 American Physical Society.

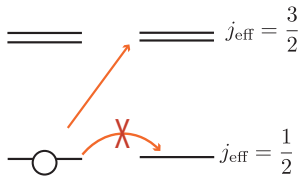

Figure 2.5: Direct hopping of hole between neighboring $j_{\text{eff}} = 1/2$ state is prohibited. Instead, hopping happens via the $j_{\text{eff}} = 3/2$ state.

can adopt edge, face, or corner-sharing arrangements. The choice of sharing geometry determines the degree of orbital overlap between the M-M or M-O-M orbitals and profoundly impacts the material's electronic band structure and magnetic exchange interactions by influencing spin-spin interactions

In the edge sharing geometry, there are two super-exchange pathways between the magnetic ions which interfere destructively and J_{ij} – the isotropic part of the Hamiltonian described in Eq.2.3 vanishes [18]. Furthermore, the primary terms in the interaction t^2/U (where t is the hopping parameter and U is the on-site correlation strength), exhibit a hidden symmetry: $\mathbf{\Gamma}_{ij} \propto \mathbf{D}_{ij} \otimes \mathbf{D}_{ij}$, [39]leading to $\mathbf{\Gamma}_{ij} \rightarrow 0$, for $\mathbf{D}_{ij} \rightarrow 0$ [18, 39]. This hidden symmetry is disrupted by higher order effects $\propto t^2 J_H/U^2$, with J_H representing Hund's coupling. These terms allow certain $\mathbf{\Gamma}_{ij}$ components to be active. Intriguingly, the active terms are the desired Kitaev terms [39].

In the edge sharing geometry, the quantum interference between the two hopping paths gives a selection rule $\Delta l^z = \pm 2$. [19]. This rule prohibits direct hopping and suppresses isotropic exchange. Consequently, the exchange process relies on hopping to neighboring $j_{\text{eff}} = 3/2$ state and subsequently to

$j_{\text{eff}} = 1/2$ state [19]. Hopping via the $j_{\text{eff}} = 3/2$ promotes the parallel alignment of the spins, leaving only bond-dependent Ising-like interactions of ferromagnetic nature active [19](see Fig.2.5). Therefore the effective Hamiltonian is expected to be given by:

$$\mathcal{H}_{ij}^{\gamma} = -\Gamma^{\gamma} S_i^{\gamma} S_j^{\gamma}, \tag{2.4}$$

where $\gamma = x, y, z$ and the Hamiltonian takes the form of a quantum compass. On the honeycomb lattice, Eq.(2.4) recreates the Hamiltonian of the Kitaev model [18], which can be written as:

$$\mathcal{H} = -\sum_{<i,j>} K_{ij}^{\gamma} S_i^{\gamma} S_j^{\gamma}, \tag{2.5}$$

where K^{γ} is defined as the Kitaev coupling along a bond γ and the negative sign indicates ferromagnetic coupling[†]. Strength of the Kitaev coupling is given as $K = \frac{J_H t^2}{(2U+3\lambda)^2}$ (λ is a term for spin-orbit coupling) [39].

To summarize, we can identify key prerequisites for materials that exhibit Kitaev's bond-direction-dependent interactions. These essential components include: (i) A honeycomb lattice structure, (ii) Octahedral crystal field environments, (iii) Edge sharing geometry, (iv) Substantial spin-orbit coupling strength, (v) An effective $j_{\text{eff}} = 1/2$ angular momentum, and (vi) Effective Hund's coupling.

Based on these requirements, iridium oxides, such as α-Na_2IrO_3 and α-Li_2IrO_3 were first identified as potential Kitaev candidates. Although these materials are found to magnetically order at low temperatures, they showed signatures of bond-dependent interactions in x-ray data [25].

Magnetic ordering naturally occurs in most of these real materials, as 4d and 5d transition metal ions occupy a large region in space. The large size of orbitals increases overlap between the orbitals of the neighboring sites, thus increasing the probability for direct hopping. Direct hopping between these ions reintroduces the isotropic J_{ij} back into the system. Similarly, interference between indirect hopping via the p orbital and direct d-d hopping via the xy orbitals generate an off-diagonal term $\mathbf{\Gamma}$. Therefore, for actual materials, a more general Hamiltonian of the following form is more realistic:

[†]Henceforth in this thesis K^{γ} will represent the bond-direction dependent coupling defined in Kitaev's model (Eq. 2.1) as J^{γ}.

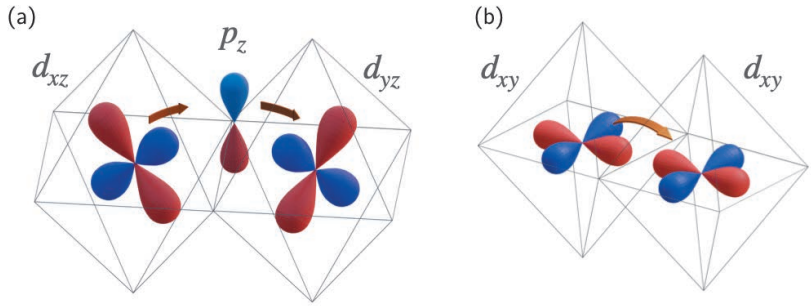

Figure 2.6: (a) Indirect hopping via ligand leads to dominant Kitaev K coupling. (b) Direct hopping via metal-metal transition contributes to Heisenberg J coupling. When both these processes (a and b) interfere they result in off-diagonal coupling Γ.

$$\mathcal{H} = K_{ij}^{\gamma} \sum_{\langle i,j \rangle} S_i^{\gamma} S_j^{\gamma} + J_{ij} \sum_{\langle i,j \rangle} \mathbf{S}_i \cdot \mathbf{S}_j + \Gamma_{ij}^{\gamma} \sum_{\langle i,j \rangle} (S_i^{\alpha} S_j^{\beta} + S_i^{\beta} S_j^{\alpha}); \qquad \alpha, \beta, \gamma \in \{x, y, z\}\,, \tag{2.6}$$

In this case not only do the extra terms in the Hamiltonian render it analytically unsolvable, but also prevent the possibility of a pure Kitaev-QSL phase.

2.3 α-$RuCl_3$

In the INTRODUCTION, we discussed briefly that α-$RuCl_3$ is supposed to have dominant Kitaev interactions. In the following subsections, we will delve deeper into the material's physical properties and elaborate how the material adheres to the prerequisites specified by Jackeli and Khaliullin. Finally we will discuss the low temperature magnetically ordered phase and the stacking faults that add to the controversies surrounding the system.

2.3.1 Structural properties

α-$RuCl_3$ belongs to the class of layered halides where the ruthenium ions that are sandwiched between two layers of halide ions form a honeycomb lattice. The sandwiched structures are only weakly connected to one another by van der Waals (vdW) forces. Within a strongly bonded layer, six chlorine ions

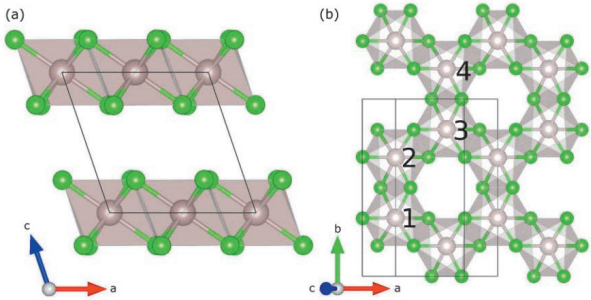

Figure 2.7: Monoclinic crystal structure of α-$RuCl_3$, showing the unit cell as a black outline, Ru as grey balls and Cl as green.(a) Projection onto the **ac**-plane. (b) Basal layer projected onto the **ab**-plane. Reprinted figure with permission from the American Physical Society, Ref.[22]. ©2015 American Physical Society.

form a perfect octahedron around a ruthenium ion. The chlorine octahedra are arranged in an edge sharing geometry. The material's structure fulfills two of the conditions specified by Jackeli and Khaliullin: the octahedral crystal field and the edge-sharing geometry of the chlorine octahedra.

Similar to other tri-halides, the weakly coupled layers result in stacking faults that can affect the structural and the magnetic properties. For high-quality single crystals of ∝-RuCl3, a three-layer stacking sequence has been identified. Early measurements on α-$RuCl_3$ had suggested a trigonal crystal structure with space group $P3_112$ [42, 43]. However, it is now widely accepted that the material adopts a monoclinic structure with space group C2/m at ambient temperature [22, 44, 45].

For temperatures below 100 K, conflicting results regarding the crystal structure have emerged. Some experiments have indicated a higher-symmetry $R\bar{3}$ space group below 150 K [45–47], while others observed the monoclinic structure persisting to very low temperatures [22, 23, 28, 48]. It is worth noting that like other vdW materials, α-$RuCl_3$ is susceptible to stacking faults, which significantly impacts its structural properties. Stacking orders can lead to either C2/m (No. 12) or $R\bar{3}$ (No. 148) space groups. As a result, a consensus has not yet been reached regarding the low-temperature space group. This matter is addressed in Chapter 4, where we utilize angle-resolved polarization-dependent Raman scattering to identify the space group of our sample at approximately ~ 4 K.

2.3.2 Electronic properties

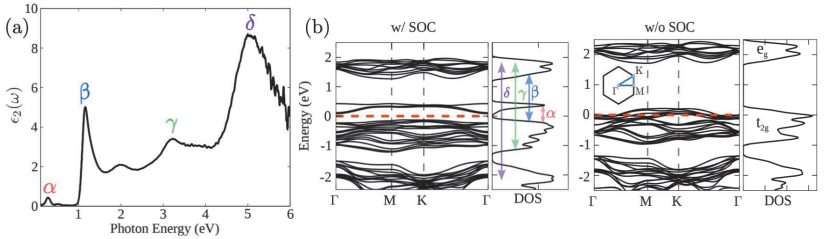

Figure 2.8: Electronic excitations observed in optical spectroscopy are explained by Linear Density of States (LDS) calculations that include spin-orbit coupling (SOC) and on-site electronic correlations (U). The agreement between the absorption data and the electronic band structure calculations supports the scenario favoring α-$RuCl_3$ as a spin-orbit coupled Mott insulator [49]. Reprinted with permission from the American Physical Society, Ref.[49]. © 2014 American Physical Society.

α-$RuCl_3$ possesses a partially filled $4d$-shell of Ru with a d^5 electronic configuration. The nearly perfect chlorine octahedra introduces crystal field splitting (CF = 2.4 eV [50]), which lifts the degeneracy of the d shell, creating $3t_{2g}$ and $2e_g$ levels. The $4d^5$ electronic configuration of Ru takes a low-spin state with $S = 1/2$. The ground state consists of a t_{2g} triplet with one hole. Early resistivity measurements by Binotto et al [51] and subsequent optical absorption measurements by Plumb et al [49] confirm α-$RuCl_3$'s classification as a Mott insulator. Spin-orbit coupling and onsite electronic correlations are found to be crucial in determining the material's electronic band structure (see Fig.2.8). The estimated values for spin-orbit coupling (SOC) are approximately $\lambda_{\text{eff}} \sim 150$ meV [21, 50, 52], while the onsite electronic Coulomb repulsion U is approximately $U \sim 1.5$ eV [21, 49] .

Spin-orbit coupling (SOC) has been shown to mix the spin and the orbital degrees of freedom and to split the t_{2g} level into $j_{\text{eff}} = 1/2$ and excited $j_{\text{eff}} = 3/2$ states. However, due to the relatively small spin-orbit coupling the bands near the Fermi level are mixtures of $j_{\text{eff}} = 1/2$ and $3/2$. Nevertheless, Kim et et al [21] have found that when the on-site Coulomb interaction U is introduced while fixing a paramagnetic state, the bands near the Fermi level take on a predominantly $j_{\text{eff}} = 1/2$ character and open a bad gap, characterizing the compound as an effective $j = 1/2$ compound. Additionally, the material exhibits significant Hund's coupling with $J_H \sim 0.34$ eV [49]. Significant spin-orbit coupling, effective $j = 1/2$ angular momentum, and effective Hund's coupling are some of the prerequisites for the observation of Kitaev-related

physics [18] These electronic properties make α-$RuCl_3$ a potential candidate to replicate the Kitaev model.

2.3.3 Magnetic properties

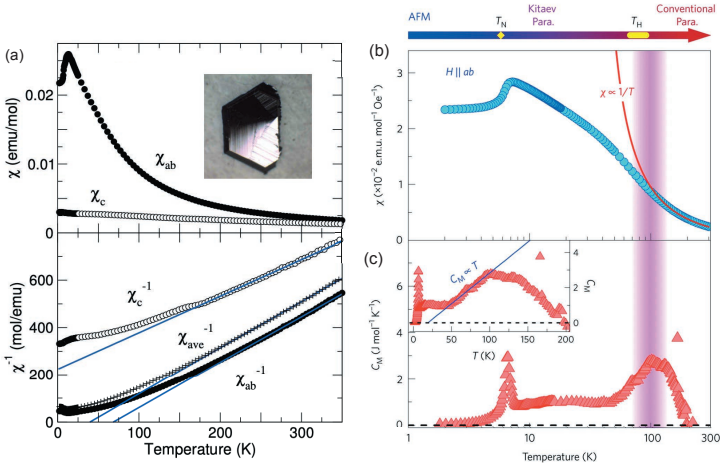

Figure 2.9: (a), (b) show magnetic susceptibility measurements of α-$RuCl_3$ measured by Sears et al [53] and Do et al [26] respectively with a small magnetic of $\sim 0.5\,\mathrm{T}$. In-plane susceptibility χ_{ab} in both the measurements shows a kink close to $T_N \sim 7\,\mathrm{K}$ indicating a magnetic phase transition. (c) Magnetic heat capacity measurements by Do et al [26]. The subset shows a bump between $T_N \lesssim T \lesssim 50\,\mathrm{K}$. (a) Reprinted figure with permission from the American Physical Society, Ref.[53]. ©2014 American Physical Society. (b), (c) Reproduced from Ref.[26] with permission from Springer Nature. © 2017 Springer Nature.

Several research groups have reported on the magnetic susceptibility of α-$RuCl_3$ [29, 53–56]. Early on the experimental studies have revealed a strong magnetic anisotropy in the compound, with χ_{ab} much larger than χ_c. At high temperatures, the magnetic susceptibility follows the Curie-Weiss law, with effective moments of 2.0-2.4 μ_B for fields applied in the honeycomb **ab**-plane, and 2.3–2.7 μ_B for fields applied out of the plane [39]. However, recent experimental [55] and ab-initio [57] estimates have suggested an even larger anisotropy in the g-values with $g_{ab} \sim 2.0-2.8$, and $g_c \sim 1.0-1.3$. The initial interpretation of the large magnetic anisotropy was based on the anisotropic Landé g factor [22, 55]. However, it was later demonstrated that off-diagonal $\boldsymbol{\Gamma}$ interactions could contribute to this anisotropy [56, 58, 59].

Remarkably, at intermediate temperatures ($\sim 140\,\mathrm{K}$), the magnetic susceptibility deviates from the Curie-Weiss law. This deviation has been linked to the onset of short-range spin correlations by Do et al [60]. The magnetic specific heat (C_M) data shows a peak at $T_N \sim 7\,\mathrm{K}$ and two broad bumps in $T_N \lesssim T \lesssim 50\,\mathrm{K}$ and around $T = T_H \simeq 100\,\mathrm{K}$. The two bumps have been associated with excitations of localized and itinerant Majorana fermions that emerge due to the Kitaev interactions in the system.

At lower temperatures, the kink in magnetization susceptibility χ_{ab} and the bump in the magnetic specific heat around $T_N = 7\,\mathrm{K}$[‡] show a phase transition to a zigzag antiferromagnet at low temperatures. The magnetically ordered phase emphasizes the role of Heisenberg exchange in the system. Overall, the thermodynamic measurements as well as the spectroscopy studies discussed in the INTRODUCTION indicate that the magnetic properties of α-$RuCl_3$ result from an interplay of the Kitaev, Heisenberg and the off-diagonal Γ interactions.

Zigzag phase

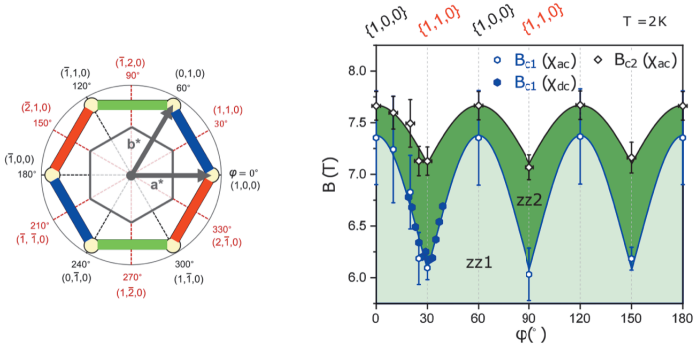

Figure 2.10: (a) Honeycomb lattice in the *ab*-plane. In real space (1, 1, 0) represents the direction perpendicular to the bond and (1, 0, 0) represents the direction parallel to bonds. (b) In-plane anisotropy of the zigzag phase [61]. Reprinted with permission from the American Physical Society, Ref.[61]. © 2021 American Physical Society.

[‡]The ordering temperature is related to the sample quality. See the section on stacking faults (Sec.2.3.4) for more information.

In the low-temperature regime the magnetic neutron scattering measurements observe magnons which confirms the long-range magnetic order [24, 29, 62]. Using the magnetic diffraction data the magnetic structure has been identified as a zigzag anti-ferromagnet. The zigzag runs parallel to the crystallographic **a**-axis of the material within the **ab**-plane with the spins oriented at about 35° out of plane [23]. The material shows an in-plane anisotropy with a 6-fold periodicity in the magnetization data as seen in Fig.2.10. This is reflected in the critical field of the magnetic order: For $H \parallel \mathbf{a}$ the zigzag is suppressed at 7.3 T, while for $H \parallel \mathbf{b}$ the system transitions into a second zigzag phase and the long-range order is suppressed at 7.8 T [61].

2.3.4 Stacking faults

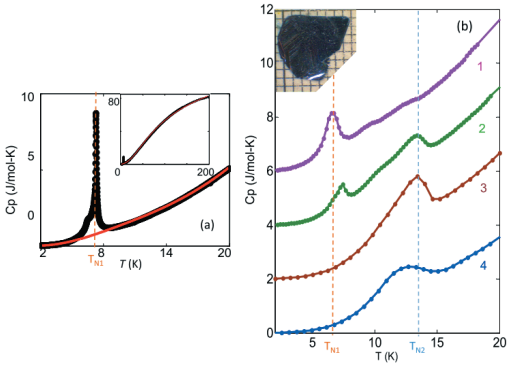

Figure 2.11: Specific heat measurements from Cao et al [23]. (a) The measurement shows data from a good quality crystal without stacking faults. (b) Sample in (a) subjected to deformation. Magnetic transitions at higher temperatures up to 14 K. Reprinted figure with permission from the American Physical Society, Ref.[23]. © 2016 American Physical Society.

Stacking faults play a crucial role in determining the structural and magnetic properties of α-$RuCl_3$. Therefore, sample characterization remains an issue for this material. Here specific heat measurements by Cao et al come to the rescue. Fig.2.11 shows the specific heat measurements from [23] that are taken by gradually introducing stacking faults in a high-quality single crystal of α-$RuCl_3$. The results show that the single crystals of α-$RuCl_3$ show a single, well-defined magnetic transition between $6 - 7$K, marked by a single sharp peak in the specific heat data. When the same sample is deformed by

stress, a second anomaly is observed around 14 K, while the anomaly at 7 K loses strength. On further deformation, the anomaly at 7 K fully vanishes leaving behind a broad anomaly at 14 K, similar to the specific heat data of the powder sample (blue line). Cao et al note that the high-quality single crystals show a three-layer stacking of ABCABC periodicity of the C2/m unit cells. In contrast, the deformed crystals show regions with a two-layer ABAB stacking sequence [23].

It is now accepted that high-quality single crystals of α-$RuCl_3$ show a single magnetic phase transition at 7 K. The samples used to collect the data presented in Chapters 4, 6-8, were checked for stacking faults using heat capacity and magnetic linear dichroism. These samples exhibit a single-phase transition at 7 K, indicating their single-crystal nature and a three-layer stacking periodicity (see Appendix I).

In this chapter, we presented the Kitaev model and discussed Jackeli and Khaliullin's mechanism for engineering the Kitaev interaction. While discussing the physical properties of α-$RuCl_3$, we saw how the structural and electronic properties of the material play a role in determining the spin-exchange. We also explored the interplay between the Kitaev, Heisenberg, and off-diagonal interactions, which results in the unconventional magnetic properties of α-$RuCl_3$. With the foundation laid for our focus compound, α-$RuCl_3$, in the next chapter, we will discuss our preferred experimental technique - Raman scattering.

3 RAMAN SCATTERING

"To an observer situated on the moon or on one of the planets, the most noticeable feature on the surface of our globe would no doubt be the large areas covered by oceanic water. The sunlit face of the earth would appear to shine by the light diffused back into space from the water-covered areas." -C.V. Raman

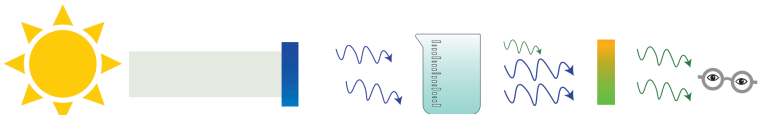

Figure 3.1: Sketch of the first Raman scattering setup, where C. V. Raman and K.S. Krishnan used sunlight as the source, and observed the scattered light with the naked eye.

During his 15-day voyage from London to Bombay, C.V. Raman became captivated by the deep blue of the Mediterranean. Unsatisfied with Lord Rayleigh's explanation that the sea reflected the color of the sky, Raman sought to answer the question, "Why is the sea blue?". By the end of his voyage, Raman had concluded that water molecules scattered light, which gave the sea its characteristic color. Interestingly, his conclusion mirrored the explanation Lord Rayleigh had provided to explain the blue color of the sky. Raman's fascination with the color of the sea led him to explore the phenomenon of inelastic light scattering in his laboratory in Calcutta together with his student, K.S. Krishnan. Their collaborative efforts culminated in a groundbreaking discovery, which they documented in a paper titled "A new

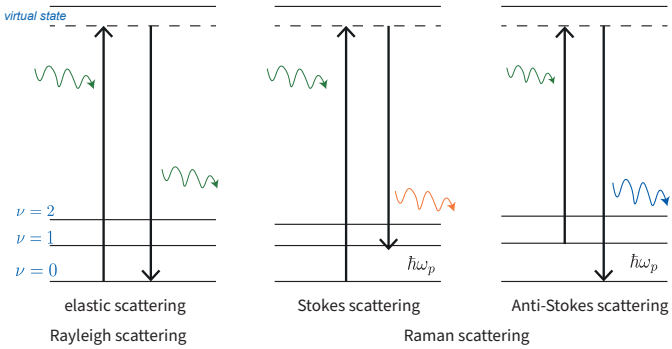

Figure 3.2: Raman scattering mechanism. The first process depicts elastic scattering, where the frequency of the incident and the scattered light is the same. The second and the third processes depict the Stokes and the anti-Stokes scattering . The energy difference between the two vibrational levels is denoted by $\hbar\omega_p$.

type of secondary Radiation" [2]. Inspired by Arthur Compton's hypotheses that electrons could inelastically scatter x-rays, Raman and Krishnan theorized a similar effect for visible light when interacting with atoms and molecules. In their experiment, they employed a blue-violet filter to isolate violet radiation from sunlight and then directed this violet light through a solution. As a result, they observed the appearance of green light alongside the violet beam. Although the green light was faint, they were able to filter it out using a yellow-green filter. The authors conducted experiments on approximately 60 different liquids and dust-free gas samples, and they found that this new type of secondary radiation was consistently present in all of them. This pivotal experiment laid the foundation for a novel spectroscopic technique known as "Raman scattering."

Raman scattering is an inelastic scattering process, where the energy of the incident light changes upon interacting with the matter. If the incident photon of frequency ω_i loses energy to the matter the process is called Stokes scattering, and the frequency of the scattered photon is $\omega_i - \omega_p$. In this process, matter gains additional energy $\hbar\omega_p$ usually in the form of vibrational energy in crystals. If the energy of the scattered light is greater than the incident light the process is called anti-Stokes scattering, and the frequency of the scattered photon is $\omega_i + \omega_p$ (see Fig.3.2). In this case, matter loses energy $\hbar\omega_p$.

In this chapter, the basic principles of Raman scattering are discussed using the macroscopic and the microscopic theory. This is followed by a short dis-

cussion on the use of group theory in analyzing the Raman spectra. After which, excitations that are interesting for this thesis and that can be probed by Raman scattering are discussed. A variation of Raman scattering, Raman optical activity is described as a probe of chiral excitations, specifically for magnetic excitations. We then discuss Raman scattering from magnetically ordered systems. The chapter closes with a general description of the experimental setup used in this thesis.

3.1 Macroscopic introduction

Light scattering can be understood on the basis of classical electromagnetic theory. When an electric field E is applied to a solid, it creates an induced oscillating dipole which emits the scattered light. If the frequency of the emitted light is same as the incident light, Rayleigh scattering is observed. If the frequency of the scattered light is different than the incident light, Raman scattering is observed. In the following, the process is described in detail*.

The polarizability α of a vibrating molecule can be given as:

$$\alpha = \alpha_0 + \frac{d\alpha}{dQ}\cos(\omega_p t) + ... \tag{3.1}$$

α_0 is the polarizability of the molecule at equilibrium and ω_p is the frequency of the molecular vibration (phonon) which induces a small change in the polarizability. Q is the normal coordinate for the vibration with frequency ω_p. The incident light induces a dipole $\mu = \alpha E$ in the molecule.

For an oscillating incident electric field described as $E = E_0\cos(\omega_L t)$, and using Eq.3.1 the electric field induced dipole is given as:

$$\mu = \left[\alpha_0 + \frac{d\alpha}{dQ}\cos(\omega_p t) + ...\right] E_0\cos(\omega_L t) \tag{3.2}$$

which can be written as:

$$\mu = \alpha_0 E_0\cos(\omega_L t) + \frac{1}{2}\frac{d\alpha}{dQ}E_0\left[\cos(\omega_p t + \omega_L t) + \cos(\omega_p t - \omega_L t)\right] \tag{3.3}$$

*This case is discussed for vibrational excitations which are usually probed with Raman scattering. A similar treatment can be applied to different excitations. For example, a similar treatment is performed for spin waves in Ref.[63].

Here the first term results in Rayleigh scattering and the second term results in sidebands arising from the change in the polarizability induced by the vibrational excitations. Therefore, a change in the molecular polarizability results in sidebands at frequencies $(\omega_L \pm \omega_p)$. The sideband at frequency $\omega_L + \omega_p$ is from anti-stokes scattering and the sideband at frequency $\omega_L - \omega_p$ is from Stokes scattering.

For crystals, the susceptibility tensor χ_{jl} can be used instead of the molecular polarizability α. The susceptibility can then be expanded with respect to the normal coordinates Q_k and one obtains:

$$\chi_{jl} = (\chi_{jl})_0 + \sum_k \left(\frac{\partial \chi_{jl}}{\partial Q_k}\right)_0 Q_k + \sum_{k,m} \left(\frac{\partial^2 \chi_{jl}}{\partial Q_k \partial Q_m}\right)_0 Q_k Q_m + ... \tag{3.4}$$

the sum runs over all normal coordinates. $\frac{\partial \chi_{jl}}{\partial Q_k}$ is a component of the derived polarizability tensor. This tensor is also known as the Raman tensor and is often written as χ_{jlk}. The intensity of the Raman mode can be easily derived in terms of the susceptibility tensor as $I \propto |\mathbf{e_s} \chi_{jlk} \mathbf{e}_i|^2$ [†].

Where $\mathbf{e}_i$ and $\mathbf{e}_s$ are the polarizations of the incident and the scattered light respectively.

3.2 Microscopic introduction

The microscopic theory is based on time-dependent perturbation theory. In this approach, an oscillating electric field perturbs the system by exciting an electron in the system. In large molecules and crystals, exciting one electron does not cause a significant change on the atomic configuration. In these cases third order perturbation theory has to be to considered in which the excited electron perturbs the atomic configuration by creating a phonon through an electron-phonon interaction [65].

In this picture the scattering process can be visualized as follows. The incident light from a laser with energy E_L excites an electron in initial state E_i to an excited state E_m by absorbing a photon of energy $E_L = E_m - E_i$. The electron deforms the atom and creates a phonon with energy E_p and relaxes to a virtual state with energy $E_{m'}$ $(E_p = E_m - E_{m'})$. From the state E'_m, the electron decays back to its initial state E_i by emitting a photon of energy $(E_m - E_p - E_i)$. The difference in the energy of the incident and the scattered light probes the energy of the phonon E_p.

[†] A complete derivation of this relation can be found in [64]

The transition probability of the entire process can be written as:

$$I(\omega_q, E_{laser}) = \sum_f \left| \sum_{m,m'} \frac{\langle i|\mathcal{H}_{eR}(\omega_s)|m'\rangle\langle m'|\mathcal{H}_{e-ion}|m\rangle\langle m|\mathcal{H}_{eR}(\omega_L)|i\rangle}{(E_{laser} - \Delta E_{mi})(E_{laser} - \hbar\omega_q - \Delta E_{m'i})} \right|^2 \quad (3.5)$$

The matrix elements $\langle m|\mathcal{H}_{eR}(\omega_s)|i\rangle$, $\langle m'|\mathcal{H}_{e-ion}|m\rangle$ and $\langle i|\mathcal{H}_{eR}(\omega_L)|m'\rangle$ describe the three steps of the Raman scattering process and are time dependent.

The microscopic theory helps in describing the resonant Raman process and accounts for the electron-phonon interaction in the system. This approach also provides quantitative information about the resulting intensity of the observed mode.

The intensity of excitations is an observable closely related to the scattering cross-section. This relationship is defined as:

$$I \sim \frac{d^2\sigma}{d\Omega d\omega} = \frac{\text{outward particle flux}}{\text{inward particle flux}}\,. \quad (3.6)$$

The Raman effect is an inelastic scattering process, and its intensity provides valuable insights into the correlation between two photons: one being the incident photon and the other the scattered photon. According to Fermi's golden rule, the Raman intensity can be expressed as the Fourier transform of a correlation function [4, 34, 66]:

$$I = \int dt \langle \mathcal{R}(t), \mathcal{R}(0)\rangle e^{i\omega t}\,, \quad (3.7)$$

In this equation, the intensity I is closely related to the correlation function of the Raman operator $\mathcal{R}$, which describes the interaction between the system and the probe. An example of a Raman operator is the Fleury-Loudon operator:

$$\mathcal{R} = \sum_{\langle i,j\rangle} J_{ij}\mathbf{S}_i \cdot \mathbf{S}_j(\mathbf{e}_i \cdot \mathbf{r}_{ij})(\mathbf{e}_s \cdot \mathbf{r}_{ij}). \quad (3.8)$$

where J_{ij} represents the coupling strength between $\mathbf{S}_i$ and $\mathbf{S}_j$. $\mathbf{e}_i, \mathbf{e}_s$ are polarizations of the incident and the scattered light, and $\mathbf{r}_{ij}$ is the unit vector connecting site i to j.

3.3 Group theoretical approach

In this section, we explore the use of group theory in determining the selection rules for Raman scattering from vibrational excitations. In Raman scattering, the perturbation Hamiltonian can be described by the equation provided in Ref.[65]:

$$\mathcal{H}'_{\text{Raman}} = \frac{\Delta\boldsymbol{\alpha}}{2}\mathbf{EE}\cos(\omega \pm \omega_\nu)t \tag{3.9}$$

where the transformation properties of $\mathcal{H}'_{\text{Raman}}$ are those of a second rank symmetric tensor, as the tensor $(\mathbf{EE})$ is external to the molecular system and it is only the polarizability tensor that pertains to the molecule.

For any process to be be Raman active, the transition matrix $\mathbf{M}_{ij}$ connecting the initial and final states must be non-zero, i.e,

$$\langle\psi_f|\mathcal{H}'_{\text{Raman}}|\psi_i\rangle \neq 0 \tag{3.10}$$

where ψ_f is the final state corresponding to the normal mode to be excited, ψ_i is the ground state, and $\mathcal{H}'_{\text{Raman}}$ is the Raman perturbation Hamiltonian.

At this point group theory can be invoked to determine the selection rules for Raman scattering. In order to do so consider: Γ_{f}, Γ_{i}, Γ_{Raman} are the irreducible representations of ψ_f, ψ_i and $\mathcal{H}'_{\text{Raman}}$, respectively. For any matrix element to be non-zero, direct product of $\Gamma_{\text{Raman}} \otimes \Gamma_i$ must contain the irreducible representation Γ_{f}. Out of which Γ_i is the irreducible representation of the ground state and contains the full symmetry of the group of Schrödinger's equation. Therefore, Γ_f must be contained in the irreducible representation of $\mathcal{H}'_{\text{Raman}}$. As the polarizability tensor $\boldsymbol{\alpha}$ is a second rank tensor, $\mathcal{H}'_{\text{Raman}}$ also transforms according to the quadratic basis functions xx, xy, zz, xy, xz, yz. Therefore, a vibrational mode is Raman active only if it has an irreducible representation with a quadratic basis [65].

The basis functions are listed in the character table of the point group and indicate the vibrational modes that would be Raman active [65]. As an example, the character table of the 2/m point group is shown in Fig.3.3[‡].

From the character table in Fig.3.3, it is clear that the modes A_g and B_g modes are Raman active and A_u and B_u modes are infrared active. The Raman tensors for the A_g and the B_g modes constructed using the functions in the character table are given as:

[‡]Character tables for different point groups can be obtained from [67]

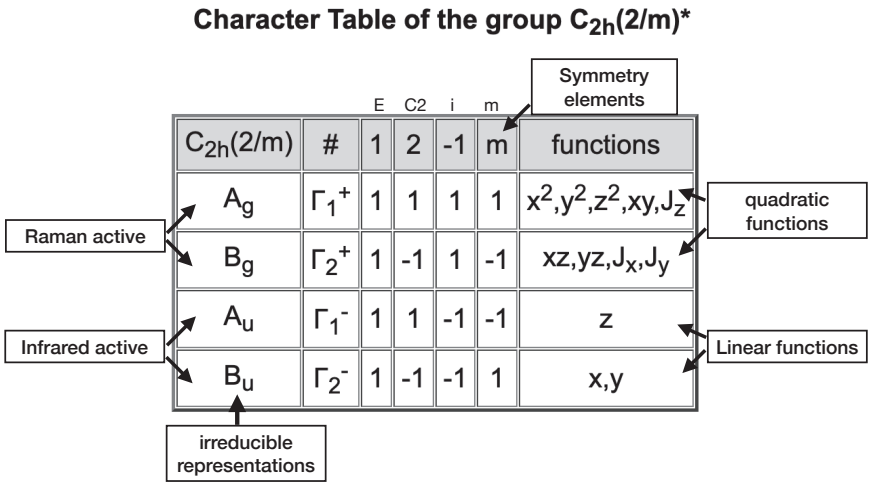

Figure 3.3: Character table of the crystallographic point group 2/m. The character table is constructed for the 2-fold axis along the **z**-axis and a mirror plane in the **xy** crystallographic plane [67]. Note that the functions $\frac{yz-zy}{2}$, $\frac{xz-zx}{2}$, and $\frac{xy-yx}{2}$ have transformations that correspond to angular momenta. The basis functions for the angular momenta are given in the character table as J_x, J_y, and J_z.

$$A_g = \begin{pmatrix} a & d & 0 \\ d & b & 0 \\ 0 & 0 & c \end{pmatrix} \quad B_g = \begin{pmatrix} 0 & 0 & e \\ 0 & 0 & f \\ e & f & 0 \end{pmatrix} \tag{3.11}$$

From Eq.3.11, it is clear that in backscattering geometry with light parallel to the **z**-axis, only the phonons with A_g symmetry can be probed. This example shows how the character table or the derived Raman tensors can be used to identify the polarization selection rules of the vibrational modes.

3.4 Excitations observed in Raman spectra

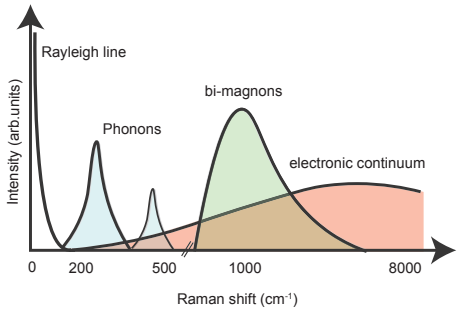

Figure 3.4: Sketch of commonly probed Raman excitations.

Raman spectroscopy serves as a versatile tool for investigating a wide range of excitations within a system. It enables the exploration of bosonic excitations such as phonons and magnons, as well as fermionic particles like electrons. Figure 3.4 shows a sketch of Raman spectra and the associated excitations. In this section, we will delve deeper into these excitations. Our primary focus will be on magnetic excitations and Majorana fermions.

3.4.1 Phonons

Phonons are the elementary excitations of the lattice of a crystal. The energy of the lattice vibrations make Raman scattering with visible light an ideal probe. The macro- and microscopic introductions describing the Raman effect are most often discussed for the phonons (as is done here in section:-

3.1, 3.2 and 3.3). In order to detect a structural phase transition, a typical Raman spectroscopy experiment measures the phonon parameters like its energy, intensity and linewidth as a function of a changing external parameter like temperature, pressure or magnetic field.

3.4.2 Electrons

Electronic Raman scattering provides information about energy levels, band gaps, and electronic transitions in a material. This technique is widely used to investigate the electronic properties of semiconductors, insulators, metals, and other materials. It is also used to study charge carriers, excitons, and other electronic phenomena in various systems. A detailed explanation about electronic Raman scattering and its applications can be found in Ref.[68].

In electronic Raman scattering, the Raman shift of the incident laser light is related to an electronic transition as opposed to a vibrational transition in conventional Raman scattering [69]. Electronic Raman scattering provides information on the two-particle correlation function, which is in close correspondence to the transport properties [70]. Here, we will briefly discuss electronic Raman scattering in superconductors.

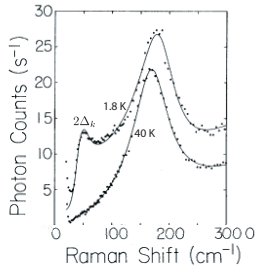

Figure 3.5: Raman spectrum of Nb_3Sn – a high T_c superconductor measured as a function of temperature. Gap opening can be observed in the superconducting phase of the compound. Reprinted with permission from the American Physical Society, Ref.[71]. ©2001 American Physical Society.

Superconductivity is the property of certain materials to conduct electricity without loss when they are cooled below a critical temperature T_c. A theory explaining superconductivity was given by Bardeen, Cooper, and Schrieffer also known as the BCS theory. A key conceptual element in this theory is the pairing of electrons close to the Fermi level into Cooper pairs

through interaction with the crystal lattice. According to the BCS theory, one finds that the pairing opens a gap $2\Delta_k$ in the continuous spectrum of the allowed energy states of the electrons, meaning that all excitations of the system must possess some minimum amount of energy. This gap for excitations leads to superconductivity, since small excitations such as scattering of electrons are forbidden.

Electronic Raman scattering has proven to be a useful experimental technique for studying superconductors as it provides a direct probe of the superconducting gap via the breaking of Cooper pairs by the incident light [72]. In the electronic Raman spectrum a coherence peak is observed at an energy of $2\Delta_k$ which results from the breaking of a Cooper pair into individual electrons. Fig.3.5 shows the temperature dependent Raman spectra of Nb_3Sn with $T_c = 18.3\,\mathrm{K}$. In the superconducting phase the lower energy region of the spectrum acquires a gap and a coherence peak is formed at energy $2\Delta_k$. As the temperature lowers the gap energy increases and the coherence peak sharpens [4].

3.4.3 Magnons

Magnons are spin wave excitations of a magnetically ordered state. Single- and multi-magnon excitations are visible in Raman scattering and are driven by different mechanisms. The two most common of these scattering mechanisms are discussed below.

3.4.3.1 Elliott-Loudon scattering

Elliott and Loudon have described a mechanism for inelastic light scattering from spin waves (see reference [73] for details). The authors initially proposed two possible processes:

1. A spin-flip transition driven by magnetic dipole interaction in ferromagnets. This mechanism requires second-order perturbation theory.
2. A spin-flip transition driven by electric dipole interaction via spin-orbit coupling.

Out of these two scattering processes, scattering by the electric-dipole interaction is more efficient. Although the electric field vector of the incident light does not directly interact with the electronic spins, there is an indirect interaction due to the mixing of spin and and orbital degrees of freedom. The scattering technique can be intuitively understood using the following example from [73].

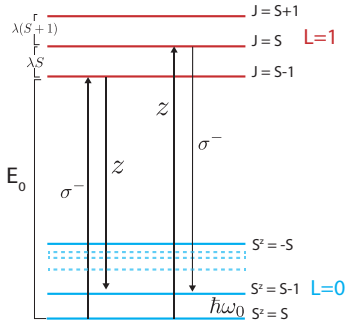

Figure 3.6: Elliott-Loudon scattering process. Raman process is a superposition of all the transitions between states S and $S-1$ [73].

Consider a ferromagnet, in which the ground state has a spin S and zero orbital angular momentum $L = 0$ (S - orbital). Suppose that the ion has an excited state P with orbital angular momentum $L = 1$ and the same spin S as the ground state. Exchange interaction removes the degeneracy of the ground state by introducing splitting between the magnetic spin quantum numbers[§]. Therefore, in the ground state the following states are present: $-S$, $S-1$,..., $S-S$, $S+1$,...,$+S$. In the $L = 1$ state (P - orbital), spin-orbit coupling lifts the degeneracy by splitting the levels into $S-1$, S, $S+1$ states. Fig.3.6 provides a sketch of the described electronic levels.

Creation of a one-magnon excitation reduces the total spin S of the system to $S-1$. Therefore, the magnon is a linear combination of all the excitations of the individual ions from the $S^z = S$ state to the $S^z = S-1$ state. The energy difference between these two states is denoted by $\hbar\omega_o$ which is the energy of the magnon. The transition between the two states is determined by the matrix elements which connect these two states. For matrix elements written in form $|J, J^z\rangle$, a process which creates the magnon and lowers the spin is written as $S^-|S, S\rangle = (2S)^{1/2}|S, S-1\rangle$. Similarly, a process which destroys the magnon and increases the spin can be written as $S^+|S, S\rangle = (2S+1)^{1/2}|S, S+1\rangle$.

Next, the procedure for determining the Hamiltonian for one-magnon scattering can be found in Cottam et al [74]. The Hamiltonian describing the interaction of light with the magnetic system can be expressed as:

[§]Splitting introduced by the overlap between the exchange orbitals.

$$\mathcal{H}_{\text{Raman}} = \sum_r \sum_{\alpha\beta} E_i^\alpha \chi^{\alpha\beta}(r) E_s^\beta \tag{3.12}$$

In magnetic materials the susceptibility is spin-dependent and can be expanded in powers of spin operators at point $\boldsymbol{r}$ as:

$$\begin{aligned}\chi^{\alpha\beta}(r) = \chi_0^{\alpha\beta}(r) + \sum_\mu K_{\alpha\beta\mu}(r) S_r^\mu \\ + \sum_{\mu,\nu} G_{\alpha\beta\mu\nu}(r) S_r^\mu S_r^\nu + \sum_\delta \sum_{\mu,\nu} H_{\alpha\beta\mu\nu}(r) S_r^\mu S_{r+\delta}^\nu + h.o\end{aligned} \tag{3.13}$$

The first term describes the susceptibility in absence of a magnetic excitation. The second term $K_{\alpha\beta\mu}$ contributes to one-magnon scattering or to the Elliott-Loudon effect. This term is also proportional to magnetic circular birefringence or the Faraday rotation. The second term $G_{\alpha\beta\mu\nu}$ represents the second-order scattering from the the Elliott-Loudon process. This term is connected to the magnetic linear birefringence, i.e, the Voigt effect and the third term $H_{\alpha\beta\mu\nu}$ represents the contribution from exchange scattering.

From the Elliott-Loudon process, one magnon scattering can be written in the form of a spin-operator Hamiltonian as:

$$\mathcal{H}_{1\text{M}} = \frac{K}{2} \sum_r [(E_i^z E_s^+ - E_i^+ E_s^z) S_r^- - (E_i^z E_s^- - E_i^- E_s^z) S_r^+] - iK \sum_r [E_i^x E_s^y - E_i^y E_s^x] S_r^z \tag{3.14}$$

Where E_i and E_s are electric field vectors of the incident and the scattered light determined at site r. K is a term which does not depend on the lattice site in ferromagnets and is therefore taken out of the summation and $S^\pm$ and $E^\pm$ are defined as $S_r^\pm = S_r^x \pm S_r^y$ and $E_\mu^\pm = E_\mu^x \pm E_\mu^y$ with $\mu \in \{i, s\}$[¶].

The relevant terms here are S_i^+ and S_i^- which correspond to the magnon annihilation and creation operators respectively and result in anti-Stokes and Stokes scattering of the spin-waves. The polarization selection rules for the one-magnon excitation can be derived from the associated electric field vectors. For the one-magnon scattering the term $E_i^z E_s^+ - E_i^+ E_s^z$ should be non-zero. From the polarizations of the incident and the scattered light it is clear that the one-magnon excitation carries a non-zero angular momentum, which is why when the incident light is circularly polarized the scattered light is linearly polarized and vice-versa.

[¶] $E_\mu^\pm$ defines circularly polarized light polarized in the xy plane

3.4.3.2 Fleury-Loudon scattering

According to the Elliott-Loudon theory, second order scattering processes should have a scattering intensity much weaker than their first-order counterpart. Surprisingly, experimental results on anti-ferromagnetic transition metal fluorides like CoF_2 and MnF_2 show otherwise, as a very strong two-magnon peak is observed in these materials [75, 76].

To explain this observation, Fleury and Loudon [73] proposed exchange-scattering mechanism in anti-ferromagnets,which appears as the term $H_{\alpha\beta\mu\nu}$ in Eq.3.13. Such a process can create excitations in pairs with momentum k and $-k$. To describe the process, consider a simple two sub-lattice anti-ferromagnet. Dispersion of such a magnet consists of two magnon branches with frequency $\omega^{\pm}(k)$. Physically these correspond to the excitations in which $\Delta S^z = \pm 1$. Let us denote the state function using the magnon momentum $\pm k$ and the spin-direction by $\uparrow$ or $\downarrow$, indicating the sub-lattice on which the magnon is excited.

Exchange-scattering requires creation or destruction of a pair of magnons on the neighboring lattice sites. As this process results in one magnon with wave vector k and another magnon with wave vector $-k$, four types of zero wave-vector magnon states are possible [73]:

	S^z
$\lvert A\rangle = \lvert\uparrow k,\uparrow -k\rangle$	2
$\lvert B\rangle = \lvert\uparrow k,\downarrow -k\rangle + \lvert\downarrow k,\uparrow -k\rangle$	0
$\lvert C\rangle = \lvert\uparrow k,\downarrow -k\rangle - \lvert\downarrow k,\uparrow -k\rangle$	0
$\lvert D\rangle = \lvert\downarrow k,\downarrow -k\rangle$	2

For anti-ferromagnets the states $|A\rangle$ and $|D\rangle$ involve scattering predominately from only one of the sub-lattices and can produce terms like $(S_j^+)^2$ or $(S_i^-)^2$ as a result of second-order electric-dipole scattering. States $|C\rangle$ and $|D\rangle$ involve a simultaneous one-magnon excitation on both the sub-lattices and a sub-lattice exchange term $S_i^+ S_j^-$ for their production. Out of these two states, the state $|C\rangle$ is parity odd and can not be observed in Raman scattering. Therefore, light-matter interaction and an exchange interaction between the spins can result in Raman scattering from the state $|B\rangle$.

The spin-operator to excite this state can be given as $S_i^+ S_j^- + c.c = 2(S_i^x S_j^x + S_i^y S_j^y)$.

As the exchange scattering mechanism produces magnons in pairs there is no

exchange-scattering mechanism for one-magnon scattering. Another observation here is that the two-magnons generated by this mechanism carry opposite angular momentum, such that the total spin-state of the system does not change ($S^z = 0$). In ferromagnets, as there are no distinct sub-lattice sites, two-magnon states corresponding to the state $|B\rangle$ are inoperative. Therefore, in ferromagnets, the second-order Elliott-Loudon process is required to generate two-magnon excitations. In anti-ferromagnets as the Fleury-Loudon scattering mechanism is completely different from the Elliott-Loudon scattering, the stronger intensity of the second-order excitation is not surprising.

3.4.4 Majorana fermions

A Majorana fermion is a fermion that is its own antiparticle. First predicted by Ettore Majorana in 1937, Majorana fermions have been sought after in high energy physics. These exotic excitations are predicted to emerge in the Kitaev quantum spin liquid phase[14].

In the spin-liquid phase, the excitations carry fractional quantum numbers relative to the local degrees of freedom and only multiple quasi-particles can couple to an external probe. Therefore, a multi-particle response is expected from Majorana fermions in the Raman spectrum of a Kitaev-Heisenberg magnet. The two possible scattering channels are shown in Fig.3.7. In process A, a pair of fermions with energy $\varepsilon_1 + \varepsilon_2$ is created by inelastic scattering. In process B, one Majorana fermion with energy ε_1 is created and one with energy ε_2 is annihilated [35].

The Fleury-Loudon operator, which describes a two-magnon excitation, is also used to derive the intensity of Raman scattering from Majorana fermions [34, 77]. The scattering is defined as $I(\omega) = \int dt \langle \mathcal{R}(t), \mathcal{R}(0) \rangle e^{i\omega t}$ where $\mathcal{R}$ is the Fleury-Loudon operator. For Heisenberg interactions, the Fleury-Loudon operator is defined as:

$$\mathcal{R} = \sum_{\langle i,j \rangle} \mathbf{S}_i \cdot \tilde{\mathbf{J}}_{ij} \cdot \mathbf{S}_j (\mathbf{e}_i \cdot \mathbf{r}_{ij})(\mathbf{e}_s \cdot \mathbf{r}_{ij})$$

$\tilde{\mathbf{J}}_{ij}$ contains the generic couplings between $\mathbf{S}_i$ and $\mathbf{S}_j$; $\mathbf{e}_i$ and $\mathbf{e}_s$ are the vectors defining the polarizations of the incident and scattered light $\mathbf{r}_{ij}$ is the unit vector connecting sites i and j. For bond-direction dependent Kitaev interaction, the Fleury-Loudon operator is written as:

$$\mathcal{R} = \sum_{\alpha \in \{x,y,z\}} J^\alpha S_i^\alpha S_j^\alpha (\mathbf{e}_i \cdot \mathbf{r}_{ij})(\mathbf{e}_s \cdot \mathbf{r}_{ij})$$

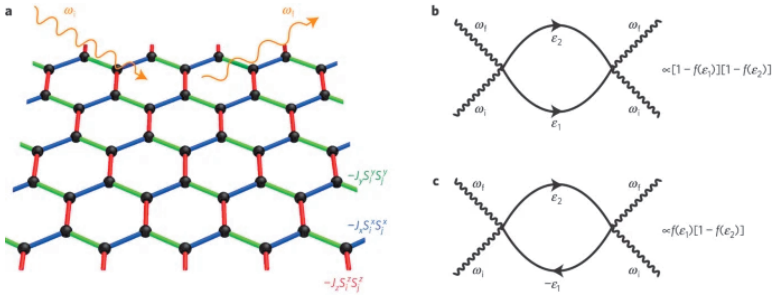

Figure 3.7: (a) Illustration of Raman scattering from Kitaev model. (b, c) Feynmann diagram showing Raman scattering from Majorana fermions, (b) shows creation of a pair of Majorana fermions with energy $(\varepsilon_1 + \varepsilon_2)$, (c) shows creation of one Majorana fermion with energy ε_1 and annihilation of the one Majorana fermions with energy ε_2. Reprinted with permission from Springer Nature, Ref.[35]. ©2016 Springer Nature.

The operator can be expanded in terms of Majorana fermions c_i and c_j, resulting in:

$$\mathcal{R} = \sum_{\langle i,j \rangle} J^{\alpha} \langle u_{ij} \rangle^{\alpha} c_i c_j (\mathbf{e}_i \cdot \mathbf{r}_{ij})(\mathbf{e}_s \cdot \mathbf{r}_{ij}).$$

where $\langle u_{ij} \rangle$ is the bond operator. Dynamical structure factor for the Kitaev-Heisenberg model has been calculated by Knolle [77] and is shown in Fig.3.8.

The results show a broad feature resulting from Majorana fermions along with a sharp excitation at the lower energy shoulder of the continuum. The sharp feature is identified as a bound state of the Majorana fermions. The expected broad continuum is observed in the Raman scattering measurements of α-$RuCl_3$, and is known to show temperature dependence on a scale much larger than the ordering temperature [30, 31] (see Chapter 1). The presence of the predicted continuum in the experimentally measured Raman spectrum of α-$RuCl_3$ confirms Raman scattering as a potential tool to study spin-liquid physics.

3.5 Raman scattering from chiral excitations

The word chirality emerges from the greek word for hand *kheir*. A simple way to think about chirality is to curl both our hands with the thumbs pointing

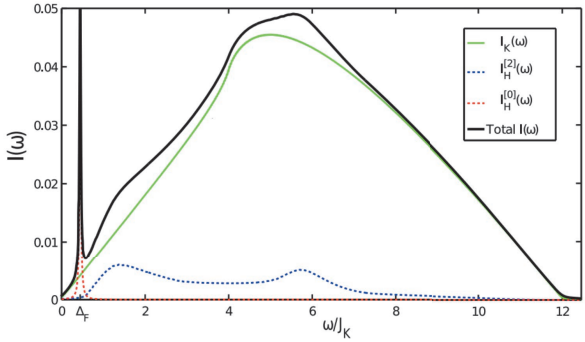

Figure 3.8: Calculated Raman scattering response from Majorana fermions from Ref.[77]. Reprinted with permission from the American Physical Society, Ref.[77]. ©2014 American Physical Society.

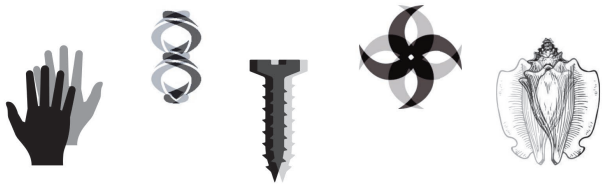

Figure 3.9: Chiral objects superposed with their mirror images.

towards the sky. The thumb represents the direction of motion of the particle and the curl of our fingers represents the chirality of the particle. The fingers of our left hand curl clockwise and the fingers of our right hand curl anti-clockwise forming mirror image of one another which cannot be exactly superimposed onto each other.

Chiral molecules come in pairs that are mirror images of one another known as *enantiomers*. Most of the biomolecules that are responsible for life are chiral, with 19 out of 20 amino acids being left handed and sugars being right handed. Even as the origin of homochirality in the molecules of life remains a mystery, in this section we will restrict ourselves to mostly worry about the chirality of the excitations in a magnetically ordered system.

In doing so, we will borrow a popular technique from biochemistry that is

routinely used to probe various chiral structures known as Raman Optical Activity (ROA).

3.5.1 Raman optical activity

Raman optical activity was developed in the 1980s, pioneered by the work of Laurence D. Barron at the University of Glasgow as an alternate means to x-ray diffraction, to study the structure of the molecules. During this time, techniques like circular dichroism and optical rotation were used to study the chirality of the molecules. However, at optical wavelengths, they probed the electronic transitions and did not provide any information on the structural details. Raman optical activity (ROA) emerged as a technique combining Raman scattering and circular dichroism. Raman scattering at optical wavelengths probed the vibrational energy levels of a molecule, which are sensitive to the structural details. Meanwhile the optical activity of vibrational excitations (phonons) provided information about the chiral cores and the percentage of enantiomers.

ROA probes the degree of circular polarization of the light scattered from the molecular polarizability and optical activity tensor to the incident light. ROA is expressed as a dimensionless quantity known as circular intensity differential which is the normalized difference in the scattered intensity of left and right circularly polarized light and is quantified as [78]:

$$\mathrm{ROA} = \frac{I_L - I_R}{I_L + I_R}$$

Depending on the geometry used, ROA can be classified as ICP - only the incident light is circularly polarized, SCP- only the scattered light is circularly polarized or DCP - dual circular polarization, i.e, incident and scattered light are both circularly polarized. In DCP two configurations are possible: $DCP\text{-}I$ - incident and scattered light have the same circular polarizations and $DCP\text{-}II$ where incident and scattered light have opposite circular polarizations. The different configurations probe different elements of the Raman tensor.

In biomolecules, the ROA signal is extremely weak, on the order of 10^{-3} to 10^{-5} times of the Raman intensity. Therefore, the routine use of this technique has only been possible due to the advances in measurement instruments which have increased the detection efficiency of the scattered light, like the Charge Coupled Devices (CCDs) and the double-grating spectrometers.

In the following, we consider circular dichroism and Raman optical activity in the context of magnetic excitations.

3.5.1.1 ROA in anti-ferromagnets

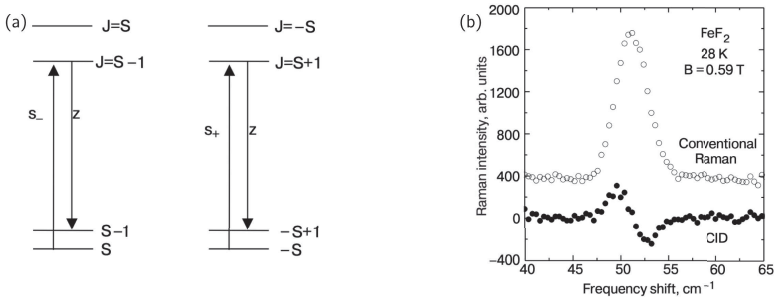

Figure 3.10: (a) Excitations on two sublattices of an antiferromagnet. (b) Spectrum of an antiferromagnetic magnon measured using conventional Raman and the energy resolved antiferromagnetic magnons measured using ROA. Reprinted with permission from AIP Publishing, Ref. [79]. ©2005 AIP Publishing.

A couple of experiments performed in early 2000s, have already studied ROA of magnons. Here, we discuss an example from Ref.[79], where ROA is studied in antiferromagnetic FeF_2.

FeF_2 possess antiferromagnetic order below the $T_N \sim 78\,\mathrm{K}$ and is made up of two sub lattices with spin up and spin down states. In the ordered phase, the magnet shows a one-magnon excitation governed by Elliott-Loudon scattering and a two-magnon excitation governed by Fleury-Loudon scattering. The single magnon is a spin-orbit coupled electric dipole excitation. When measured in Raman using circularly polarized incident light, the intensity of magnon depends on the helicity of the incident light and non-zero ROA is observed.

Magnetic Raman scattering can be understood as follows: Circularly polarized light $\sigma_\pm$ excites an electron by $\Delta m_j = \pm 1$. Therefore, an initial spin down is excited to an intermediate state with spin up by absorbing the left circularly polarized light. Second, the intermediate spin-up state relaxes to a spin-up final state by emitting a linearly polarized photon polarized along the **z**-direction. Similarly, a spin-down ground state couples with right circularly polarized light to create a spin flip.

In FeF_2 a small magnetic dipole-dipole interaction between the two sublattices slightly lifts the degeneracy of the two spin states leading to an effectively non-zero ROA. The splitting of these degenerate states is of the order $0.56\,\mathrm{cm}^{-1}$ at $0\,\mathrm{T}$ [79]. The splitting between the energy levels is evident in the difference

spectra of the line shape obtained by comparing the left and right circularly polarized light[‖]. When exposed to an external magnetic field the splitting between the two spin-states becomes more apparent (see Fig.3.10(b)).

Next section describes how group theory can be utilized to predict Raman optical activity in magnetically ordered systems.

3.6 Raman scattering from magnetically ordered systems

As magnetic-field dependent Raman scattering is discussed in this thesis, it becomes important to discuss the Raman response from magnetically ordered systems. In this section we will discuss magnetic point groups and describe a procedure to find the form of their respective Raman tensors.

Generally, crystallographic group is defined for a lattice made up of points. Points do not have any handedness associated with them and remain invariant under all the symmetry operations. When a point is replaced by a helix (for example), handedness is introduced into the crystal structure. A helix is no longer invariant under all the symmetry operations and can change its handedness on undergoing rotation, inversion or reflection (see Fig.3.11). The same is true for a magnetic spin.

Classically, magnetism can be thought of as originating from a current flowing in a closed loop. In the commonly thought right-hand rule, the curled fingers represent the flow of the current and the thumb represents the direction of the magnetic moment. That is, if the current moves in anti-clockwise direction the magnetic moment will point up and if the direction of the current is reversed to clockwise the magnetic moment will point down. Mirror planes can affect the direction of the current and can consequently reverse the magnetic moment. Therefore, the magnetic moment transforms as an axial vector. Figure 3.12 shows the effect of the mirror plane on the magnetic moment.

Furthermore, the magnetic moment is not symmetric under time-reversal operator $\mathcal{T}$ as reversing the direction of the current reverses the direction of the magnetic moment from up to down (see Fig.3.12). Therefore, in considering the symmetry of magnetically ordered systems, one has to take into account that the lattice is not made up of points, but rather of points with spins on it. The magnetic point group is found by multiplying every element of the

[‖]In the given example, ICP configuration is used as only the incident light is circularly polarized

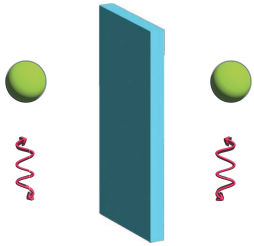

Figure 3.11: mirror plane on scalar and pseudo-scalar objects. Scalar objects like sphere remain invariant on reflection from a mirror plane. Pseudo-scalar object like a helix change handedness on reflection.

crystallographic point group with the time-reversal operator $\mathcal{T}$. The 32 crystallographic point groups result in 122 magnetic point groups, which can be sub-divided into 32 (colorless) crystallographic point groups, 32 grey groups, and 58 black-white groups [80, 81].

- **Type I** or $\mathcal{M}_I$ is a **colorless group**, without any additional antisymmetric elements, i.e. $\mathcal{M}_I = \mathcal{G}$. Where $\mathcal{G}$ is a ordinary point group without any anti-symmetric elements.
- **Type II** or $\mathcal{M}_{II}$ is a **grey group,** where the anti-symmetry version of every symmetry element is part of the group. This group can be mathematically defined as $\mathcal{M}_{II} = \mathcal{G} + \mathcal{T}\mathcal{G}$ where $\mathcal{T}$ is a time-reversal operator or $\mathcal{M}_{II} = \mathcal{G} \times 1'$, i.e as a direct product of group $\mathcal{G}$ with the point group $1'$. Where $1'$ is the time-inversion group containing the identity element E and time-reversal operator E'. In this group, all the symmetries of the parent crystallographic point group are preserved.
- **Type III** or $\mathcal{M}_{III}$ is a **black-white group** constructed of half of the symmetry operations H of purely unitary operations and of anti-symmetry versions of the remaining symmetry operations. H, should be subgroup of $\mathcal{G}$ with index 2. $\mathcal{M}_{III} = H + \mathcal{T}(G - H)$.

Ref.[82] provides 3D renderings and videos of all the 122 magnetic point groups and is an excellent tool for visualizing them.

Here, we consider an example of the monoclinic lattice belonging to the crystallographic point group 2/m. The point group has a mirror plane perpen-

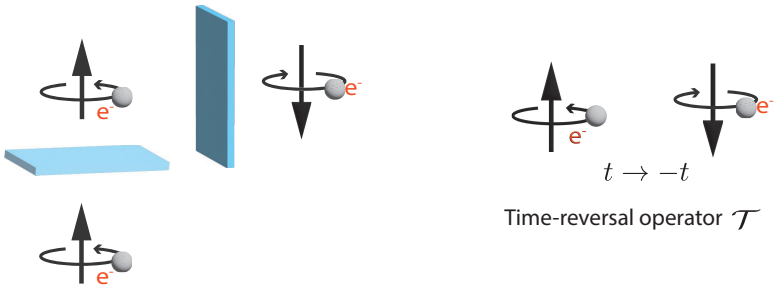

Figure 3.12: The magnetic moment is generated by the circular motion of an electron in a loop. Effect of a mirror plane and time-reversal on the magnetic moment.

dicular to the two-fold rotation axis. In this example, the spin is set to be parallel to the mirror plane (see Fig.3.13). The symmetry elements like the 2-fold axis and the mirror plane are colored blue. When the symmetry operation additionally flips the spin, it is multiplied with the time-reversal operator and is colored green. The paramagnetic phase is always represented by the grey group, which in this case 2/m1', as it is time-reversal invariant. The crystallographic group 2/m, and black-white groups 2'/m and 2/m' support antiferromagnetic ordering. The group 2'/m' is the only group that can host ferromagnetic order as all the spins point in the same direction.

If all the symmetries of the crystallographic group are maintained like for the point group 2/m, it belongs to the colorless group ($\mathcal{M}_I$). For this group all the operations remain unitary and the Raman tensors derived from the parent crystallographic group remain valid. Black-white ($\mathcal{M}_{III}$) group also known as the magnetic point group reduces the symmetry of the crystallographic point group and introduces anti-unitary elements from the time-reversal. The representations of a magnetic group that includes both the unitary and the anti-unitary operations are given by co-representations. The irreducible co-representation are related to the irreducible representations of the linear half group H. The irreducible representations of the unitary half group H are found from the irreducible representations of the grey group $\mathcal{G}$ by subduction [83].

The colorless magnetic point group 2/m, does not contain any elements that are combined with time-inversion operator. Therefore, the representations of its parent crystallographic point group remain unchanged. Same is true for the grey group 2/m1'. However, groups 2'/m, 2/m', and 2'/m'

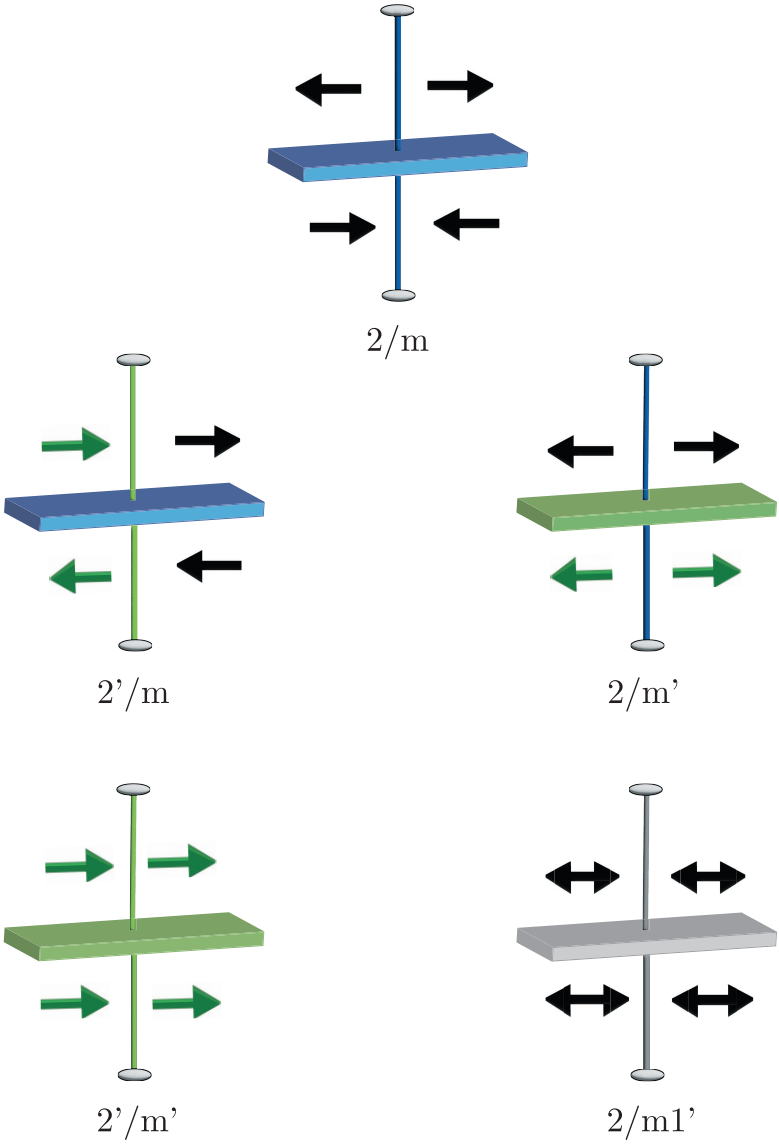

Figure 3.13: Representations of magnetic point groups for the parent crystallographic group 2/m. The vertical bar represents the two-fold rotation axis and the plane represents the mirror plane. Green represents that the symmetry operation additionally flips the spin.

contain symmetry operations that are combined with time-inversion. Time-inversion operator is anti-unitary and anti-linear in nature. Due to the presence of anti-unitary operators, representations of a unitary group are replaced by co-representations of the magnetic point-group following Wigner's co-representation theory. Cracknell & Bradley [84] describe a procedure to construct the co-representations for the magnetic point groups. The scattering matrices for black-white groups have been derived by Cracknell et al in [85].

As magnetic ordering breaks the time-reversal symmetry, it can lower the crystal symmetry, and introduce anti-unitary operations in the group. As a result, black-white magnetic groups can result in asymmetric Raman tensors that alter the selection rules compared to the paramagnetic phase. Thus, for analyzing the magnon spectrum the magnetic point group has to be considered. However, in presence of strong magneto-elastic coupling the reduced symmetry can also affect the phonon spectrum in the following ways [86] :

1. Polarization selection rules can change corresponding to the appearance of new components in the Raman tensor.
2. Normally inactive Raman modes can become observable.
3. Degenerate modes can split due to reduced symmetry.

In the following we will consider the example of CrI_3, in which the magnetic ordering has been shown to modify the selection rules [87].

3.6.1 Example: CrI_3

In CrI_3, the 127 cm^{-1} phonon shows helicity dependent scattering in the magnetically ordered phase, but not in the paramagnetic phase (see Fig.3.14). The different selection rules can be understood using group theory and by considering the magnetic point group of material.

The crystallographic point group of the material is D_{3d}. In the ferromagnetic phase, the magnetic point group of the material is given as $\bar{3}m'$ [87, 88] .

This means that the ordinary group $\mathcal{G} = D_{3d}$ and the unitary half group is $\mathcal{H} = C_{3i}$ and the magnetic point group can also be described as $D_{3d}[C_{3i}]$, where D_{3d} is the structural point group and C_{3i} is the unitary half-group. In

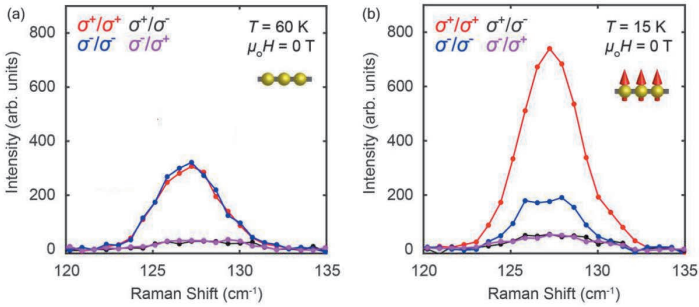

Figure 3.14: Helicity dependent scattering of the A_{1g} phonon in (a) the paramagnetic phase and (b) the Ferromagnetic phase. Reprinted with permission from Springer Nature, Ref.[87]. © 2020 Springer Nature.

the paramagnetic phase, the Raman active modes of the grey group D_{3d} are described as $\Gamma_{\mathcal{G}} = A_{1g} + E_g$.

The Raman tensors are given as [67]:

$$A_{1g} = \begin{pmatrix} a & 0 & 0 \\ 0 & a & 0 \\ 0 & 0 & I \end{pmatrix} \quad E_g = \begin{pmatrix} c & 0 & 0 \\ 0 & -c & d \\ 0 & d & 0 \end{pmatrix} \begin{pmatrix} 0 & -c & d \\ -c & 0 & 0 \\ d & 0 & 0 \end{pmatrix} \tag{3.15}$$

As can be seen from the Raman tensor, no helicity dependence is expected from the A_{1g} phonon.

The co-representations of the magnetic point group can be found using subduction of the grey group $\mathcal{G}$ to the unitary half group H [86]:

Following subduction $\mathcal{G} \rightarrow H$; $D_{3d} \rightarrow C_{3i}$

$$A_{1g} \rightarrow A_g \rightarrow DA_g$$

$$E_g \rightarrow^1 E_g +^2 E_g \rightarrow D^1 E_g + D^2 E_g$$

The corresponding Raman tensors for the magnetically ordered phase are taken from Cracknell et al [85].

The tensors are described as:

$$DA_g = \begin{pmatrix} a & ib & 0 \\ -ib & a & 0 \\ 0 & 0 & I \end{pmatrix} \quad D^1E_g = \begin{pmatrix} d & id & ic \\ id & -d & c \\ ig & g & 0 \end{pmatrix} \quad D^2E_g = \begin{pmatrix} e & -ie & -if \\ -ie & -e & f \\ -ih & h & 0 \end{pmatrix} \tag{3.16}$$

When measured using circularly polarized light in co-polarization geometry the intensity of the Raman mode can be derived as $|\sigma^{\pm}\mathcal{R}\sigma^{\pm}|^2$. For the co-polarized channel and left circularly polarized incident light the intensity of the mode is given as $I_{--} = (a-b)^2$ and for right circularly polarized light the intensity is given as as $I_{++} = (a+b)^2$. As $I_{++} \neq I_{--}$ helicity dependent scattering is expected as observed in Fig.3.14 [87].

3.7 Experimental details

Raman spectroscopy The experimental results in this thesis were measured in the High Field Magnet Lab, at Nijmegen in the Netherlands. All the experimental results that are recorded in this thesis were performed in the back-scattering geometry with the light parallel to crystallographic **c***-axis. For the measurements, we choose between a 532 nm and a 660 nm laser source. The beam path of the incident and the detected light consists of polarization inserts like the Glan Taylor polarizers and broad-band retardation plate. The back-scattered light is passed through a couple of volume-Bragg-filters (Optigrate, Oviedo, FL, USA) to reduce the contribution from Rayleigh scattering. These filters facilitate the detection of the low-energy excitations. A FHR-1000 spectrometer (HORIBA, Kyoto, Japan) equipped with 1200 g/mm grating in combination with a liquid nitrogen-cooled CCD PyLoN camera (Teledyne Princeton Instruments, Thousand Oaks, CA, USA) [89] is used for detecting the Raman scattered signal**.

At the HMFL, the Raman scattering setup spreads across two floors with two labs set above each other. In the top floor lab, all the optical elements are arranged and on the ground floor, sits a bath cryostat surrounded by a huge bitter magnet. The sample is placed in the optical insert with a microscope objective creates a tight laser spot of 2 µm radius, and a sample stage that consists of three Attocube piezo-positioners. The piezo-positioners provide a delicate XYZ positioning of the sample. The sample is placed in a bath cryostat and the sample temperature can be dropped to 1.2 K [90]. The magnetic field is created by large water-cooled Bitter magnets which can

**See Appendix II for a detailed illustration of the experimental setup.

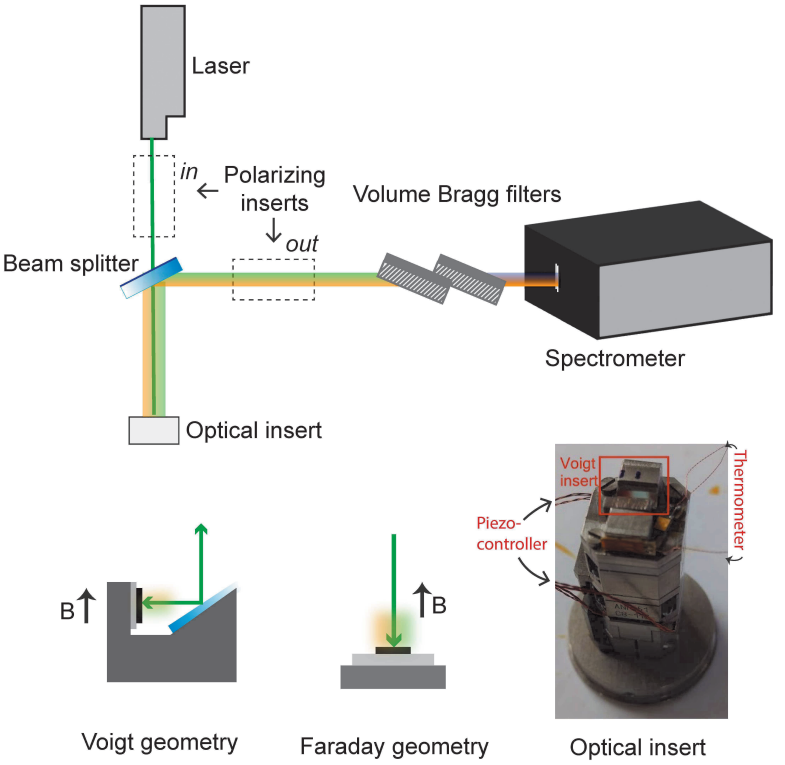

Figure 3.15: Sketch of Raman setup.

create a magnetic field upto 31 T. The sample insert is made up of titanium, to minimize the sensitivity for displacement at high magnetic fields.

Magnetic Raman scattering experiments can be set either in the Faraday or Voigt geometry. While designing the field-dependent Raman scattering experiment, we consider the following two experimental quantities:-

1. The direction of the applied magnetic field.
2. Polarization of the incident and scattered light.

Direction of magnetic field – in the crystallographic plane

As discussed in Chapter 2, α-$RuCl_3$ shows large anisotropy in the magnetic susceptibility measurement. The material shows an anomaly in the magnetic susceptibility χ_{ab} ($B \parallel \mathbf{ab}$) around $T_N = 7\,\mathrm{K}$, indicating a phase transition out of the magnetically ordered low temperature phase. However, such a feature is not observed in χ_c ($B \perp \mathbf{ab}$), suggesting that the phase transition out of the magnetically ordered phase only occurs when the magnetic field has an in-plane component [56]. Therefore, in order to reach the quantum paramagnetic phase we choose the magnetic field to be applied in the crystallographic plane.

Polarization of light – Circularly polarized light In the presence of strong magnetic fields, the objective lens, which is used to focus light onto the sample, may act as a Faraday cell and induce a rotation in the polarization of the light passing through it. Since the spectrometer is sensitive to polarization, this unintended Faraday rotation can potentially impact detection efficiency. To mitigate the effects of Faraday rotation on our experimental results, circularly polarized light is used.

To create circular polarization, the laser beam is passed through a linear polarizer and then through a quarter wave plate aligned with its fast axis at $\pm 45°$ to the fast axis of the linear polarizer. Similarly, the scattered light is passed through a quarter wave plate at $\pm 45°$ and a vertical polarizer to make sure, that the detection efficiency does not change with the magnetic field [††].

The basic setup for magnetic Raman scattering described here is used in Chapters 5 - 8. Meanwhile, in Chapter 4 the measurements are performed without an external magnetic field with linearly polarized light. To

[††] The scattered light can contain all possible polarizations. To make sure, that the intensity of the detected light is not sensitive to the magnetic field, a calculation is performed to estimate the effect of the experimental geometry on the detection efficiency of different polarizations. This can be found in Appendix II

configure the experiment, we replace the quarter-wave plates with half-wave plates as polarization inserts. Details about the experimental setup are presented in the experimental technique sections of the respective chapters.

In the following CHAPTERS, we will use Raman scattering to study the field-induced quantum paramagnetic phase in α-$RuCl_3$. Before proceeding to the field-induced phase, in the NEXT CHAPTER we will address the low-temperature crystal structure of α-$RuCl_3$.

Contributions

This chapter is written by me and represents my understanding of the topic based on all the references mentioned.

4

LOW TEMPERATURE CRYSTAL STRUCTURE OF α-$RuCl_3$

"Symmetry is what we see at a glance; based on the fact that there is no reason for any difference..." — Blaise Pascal, Pensées

Figure 4.1: a square, a rectangle, a trapezium

Humans and certain other species are inherently sensitive to symmetry. By looking at different shapes most of us can identify that certain shapes are "more symmetric" than the others. For example, a square appears more symmetric than a rectangle, which appears more symmetric than a trapezium. This measure of symmetry is captured in group theory, where a group constitutes all symmetry operations that leave an object unchanged. The selection rules for the Raman and infrared scattering are easily found using group theory, which implements the crystallographic symmetry to derive the allowed transitions. As the knowledge of crystal symmetry is crucial for analyzing the Raman spectrum, studying the low-temperature crystal structure provides an ideal starting point for this thesis.

In some of the initial Raman scattering studies on α-$RuCl_3$, D_{3d} point group of a single perfect honeycomb layer was used to label the phonons [30, 91]. However, now, the high-temperature crystallographic structure of the bulk crystal of α-$RuCl_3$ is established to be monoclinic using a combination of results from the x-ray diffraction [22, 23] and Raman scattering [44] experiments. Meanwhile, the low-temperature point group is still a subject of debate, with some studies suggesting that it remains monoclinic at low temperatures [23, 48], while others propose that it undergoes a structural phase transition to a trigonal system, similar to its sister compound $CrCl_3$ [43, 45]. As discussed in Chapter 2, the structure depends on the stacking order of the layers with respect to each other. The layers shifted by $(1/3, 0)$ correspond to a monoclinic lattice with space group C2/m, and the layers shifted by $(1/3, -1/3)$ correspond to a trigonal lattice with space group $R\bar{3}$ (see Fig.4.2)[43, 46]. The monoclinic lattice results in two-fold rotational symmetry along the **b**-axis [44], and the trigonal lattice has 3-fold rotational symmetry.

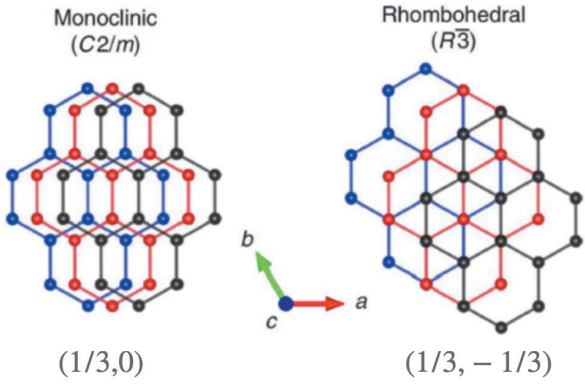

Figure 4.2: Stacking order of C2/m vs. $R\bar{3}$ space group. Reprinted from Ref.[43] under a Creative Commons Attribution 4.0 International (CC BY 4.0) license. © 2021 Loidl et al

This chapter addresses the low-temperature structure of α-$RuCl_3$. Group theory is used to derive the polarization selection rules and angle-resolved polarization dependence of the phonons observed in the two possible structural point groups. The obtained results are compared with the experimental observations to identify the crystallographic point group. At the end of this chapter, angle-resolved polarization dependence is used to verify the magnetic point group.

4.1 Group theoretical study

Usually, group theory is used to identify the symmetry of phonons and their selection rules. The essential input required for this calculation includes the crystallographic point group of the system as well as the Wyckoff positions. However, our task is to determine the low-temperature structural group from two possible choices: 1. Monoclinic (2/m) and 2. Trigonal (C_{3i}).

To begin, we derived the polarization selection rules for point groups 2/m and C_{3i}. Character tables for each of these point groups were obtained from Ref.[67], and are given in tables 4.1 and 4.2, respectively. From the character table, it can be understood that the A_g and B_g modes are Raman active for the 2/m crystallographic point group, and the A_g and E_g modes are active if the crystal belongs to the trigonal point group C_{3i}.

Table 4.1: Character table of 2/m for 2-fold rotational axes within the crystallographic plane.

$C_{2h}(2/m)$	E	C_2	i	m	functions
A_g	1	1	1	1	x^2, y^2, z^2, xz, J_y
B_g	1	-1	1	-1	xy, yz, J_x, J_z
A_u	1	1	-1	-1	z
B_u	1	-1	-1	1	x, y

Table 4.2: Character table of C_{3i}

$C_{3i}(-3)$	E	C_3	$(C_3)^2$	i	$(S_6)^5$	S_6	functions
A_g	1	1	1	1	1	1	x^2+y^2, z^2, J_z
${}^1E_g$	1	w^2	w	1	w^2	w	
${}^2E_g$	1	w	w^2	1	w	w^2	$(x^2-y^2, xy), (xz, yz), (J_x, J_y)$
A_u	1	1	1	-1	-1	-1	z
${}^1E_u$	1	w^2	w	-1	$-w^2$	$-w$	
${}^2E_u$	1	w	w^2	-1	$-w$	$-w^2$	(x, y)

The Raman tensors for these modes are derived from the character table and Ref.[67] as:

$$R(A_g) = \begin{pmatrix} a & 0 & f \\ 0 & b & 0 \\ f & 0 & d \end{pmatrix} \; R(B_g) = \begin{pmatrix} 0 & c & 0 \\ c & 0 & 0 \\ 0 & 0 & e \end{pmatrix} \tag{4.1}$$

$$R(A_g) = \begin{pmatrix} a & 0 & 0 \\ 0 & a & 0 \\ 0 & 0 & b \end{pmatrix} \quad R(E_g) = \begin{pmatrix} c & d & e \\ d & -c & f \\ e & f & 0 \end{pmatrix} \begin{pmatrix} d & -c & -f \\ -c & -d & e \\ -f & e & 0 \end{pmatrix} \tag{4.2}$$

The intensity of the Raman mode is related to the Raman tensor as:

$$I_{is} = |e_s \cdot \mathcal{R} \cdot e_i|^2, \tag{4.3}$$

where e_i and e_s are the polarization vectors of the incident and scattered light, respectively, and $\mathcal{R}$ is the Raman tensor. Tables 4.3 and 4.4 show the effect of the angle θ between the incident light polarization and the crystallographic **a** axes on the intensity of the detected modes for the 2/m and C_{3i} point groups.

Table 4.3: Intensities of the A_g and B_g modes in the parallel and cross polarization geometries for point group 2/m.

	A_g	B_g
parallel	$((a+b)+(a-b)\cos 2\theta)^2$	$(c \sin 2\theta)^2$
cross	$((a-b)\sin 2\theta)^2$	$(c \cos 2\theta)^2$

Table 4.4: Intensities of the A_g and E_g modes in the parallel and cross polarization geometries for C_{3i} .

	A_g	E_g
parallel	$(a)^2$	$((d-c)\sin 2\theta - (c+d)\cos 2\theta)^2$
cross	0	$((d-c)\cos 2\theta + (c+d)\sin 2\theta)^2$

From the polarization selection rules, the following features are observed:

1. For the C2/m space group, using the Wyckoff positions taken from Johnson et al [22], 12 Raman active modes, $6A_g + 6B_g$ modes are expected in the Raman spectrum. In the limit where the incident polarization is parallel to either the crystallographic **a** or **b** axes, the A_g mode is only visible in the parallel scattering geometry and is inactive in the cross polarization geometry. Similarly, in this limit, the B_g mode is only visible in the cross polarization geometry. The intensities of both these modes show angle dependence, as shown in Fig.4.3 for the parallel polarization geometry and in Fig.4.4 for the cross polarization geometry.
2. For the $R\bar{3}$ space group, using the Wyckoff positions obtained from Park et al [46], 8 Raman active modes, $4E_g + 4A_g$ modes are expected in the spectrum. A_g mode is only visible in the parallel polarization

geometry and does not exhibit any angle dependence (see Fig.4.5(a)). E_g mode is double degenerate and is visible in parallel as well as the cross polarization geometry. The E_g mode shows a four-fold angle-dependence in both polarization channels. Fig.4.5 compares the angle dependence of the A_g and E_g modes in the parallel and cross polarization geometries.

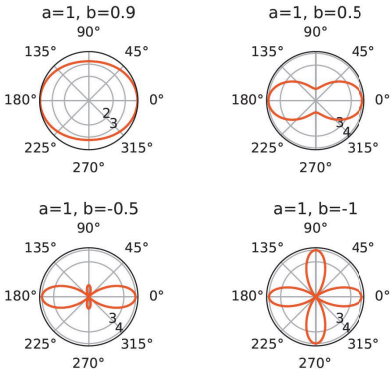

(a) A_g in parallel polarization

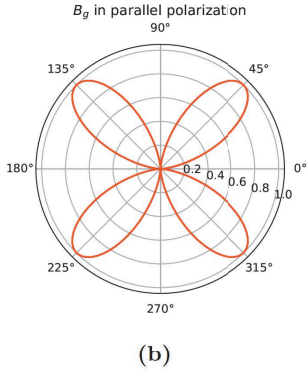

(b)

Figure 4.3: (a) Angle dependence of A_g mode for different values of tensor elements a and b in parallel-polarization geometry. The intensity of the A_g mode peaks along the crystallographic **a** and **b** crystallographic axes. (b) Angle dependence of B_g mode in parallel-polarization geometry. The intensity of the B_g mode peaks at 45° from the **a** and **b** crystallographic axes.

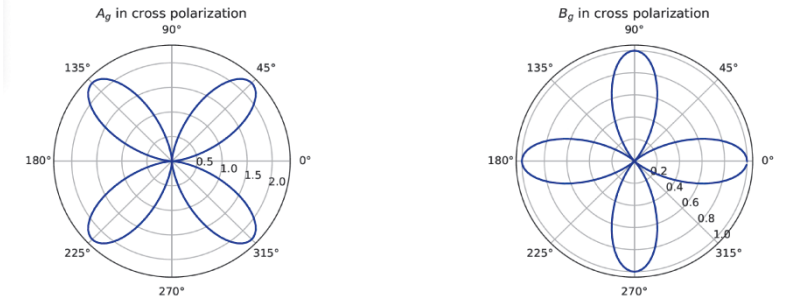

(a) **(b)**

Figure 4.4: (a) Angle dependence of the A_g mode in cross-polarization geometry for $a = -b$. For $a = b$, the intensity of the A_g mode drops to zero in the cross-polarization channel. The intensity of the A_g mode peaks at 45° from the **a** and **b** axes. (b) Angle dependence of the B_g mode in cross-polarization geometry. Intensity of the B_g mode peaks for incident light polarization along the **a** and the **b** axes.

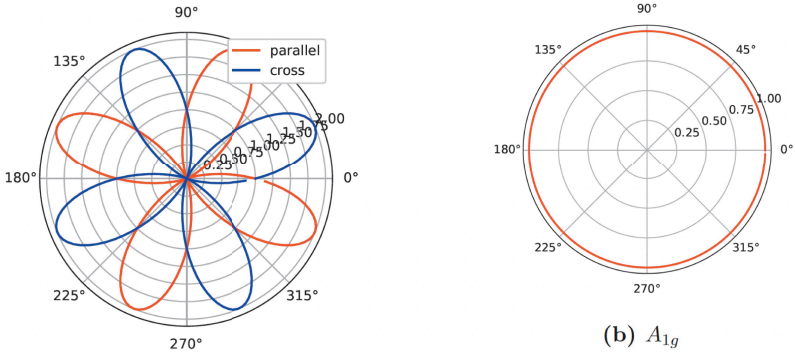

(a) E_g (for $c = 1$, $d = 0$, special case for D_{3d}) **(b)** A_{1g}

Figure 4.5: (a) Angle dependence of the E_g mode for parallel and cross polarization geometry. The E_g mode is visible in both the experimental geometries and shows a four-fold symmetry. (b) Angle dependence of the A_g mode in parallel and cross polarization geometries. The intensity of A_g remains zero in the cross polarization.

Based on the different polarization selection rules for the A_g, B_g modes of the space group C2/m and the A_g, E_g modes of the space group R$\bar{3}$, the angle-resolved polarization dependence of the excitations was found useful for

identifying the symmetry of the observed excitations.

4.2 Experimental details

Measurements were performed using linearly polarized light in parallel and cross polarization geometry using a 660 nm laser. A set of the polarization optics, appropriate for an excitation wavelength of 660 nm, including Glan polarizers and half-wave plates (Thorlabs, Newton, MA, USA), were used for azimuthally resolved measurements. Polarization of the light was rotated using half-wave plates controlled by a qudi code [89, 92]. For parallel polarization geometry, half wave plates were arranged to maximize the power of the transmitted laser light, and for cross polarization geometry, half-wave plates were aligned to minimize the power of the transmitted laser light.

The sample was helium cooled to 4 K to probe the sample in the zigzag phase, and the power of the incident light was limited to 10 µW to limit laser induced heating. Polarization dependent measurements were performed without an external magnetic field.

4.3 Results and discussions

4.3.1 Polarization dependence

The long range magnetic order in our sample is confirmed by a magnon of the antiferromagnetic phase, which is visible in the parallel polarization at 25 cm^{-1} (3.1 meV) [93]. Initially, the phonons α, β, γ and δ were identified as E_g modes while the phonon ϵ was identified as the A_{1g} mode [30, 94, 95] of a trigonal D_{3d} point group. However, as seen in Fig.4.6 small energy difference between the modes observed in the parallel and the cross polarization demonstrates that the E_g mode splits into modes with A_g and B_g symmetry. The splitting is suggestive of a monoclinic crystal structure.

The A_g mode at 312 cm^{-1} shows a four-fold angle dependence in parallel and cross polarization geometries. Figure 4.6 shows the Raman spectrum measured in the two polarization geometries, such that the intensity of the 312 cm^{-1} mode is zero in the cross polarization geometry and maximum in the parallel polarization geometry. All visible phonons are labelled as α-η. Table below compares the energies of the phonons observed in the two polarization geometries. We refer to phonons using their respective labels from α-η.

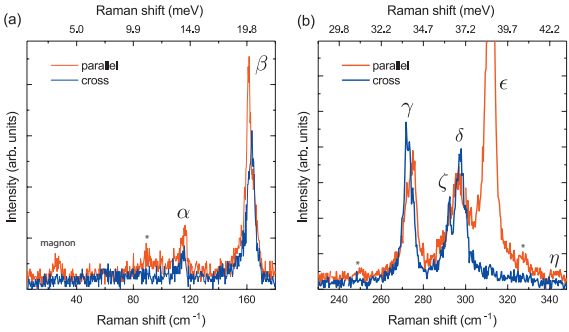

Figure 4.6: Phonons as observed in cross (xy) and parallel (xx) geometry, measured with a 660 nm laser at 4 K with 10 µW laser power. Spectra were measured in the following ranges: (a) 10 cm^{-1} to 180 cm^{-1}, and (b) 230 cm^{-1} to 350 cm^{-1}. Note: Phonons marked with (*) are not expected in the spectrum. All the labelled phonons are in agreement with the previous reports [44, 96].

Table 4.5: Energy of phonons in cm^{-1}

	α	β	γ	δ	ϵ	ζ	η
Parallel	116	162	275	297	312	-	345
Cross	115	164	273	298	-	292	-

In total 11 vibrational modes modes $6A_g + 5B_g$ are identified from the spectrum. A difference of $1 - 2$ cm^{-1} in phonon energies is observed between the previously labelled E_g phonons of the D_{3d} point group. Energy splitting of the same order has been observed in an independent Raman scattering study at room temperature and is understood to originate from the inter-layer stacking order or from a distorted honeycomb layer, such that two of the bonds of the hexagon differ from the other four [44].

4.3.2 Azimuthal dependence

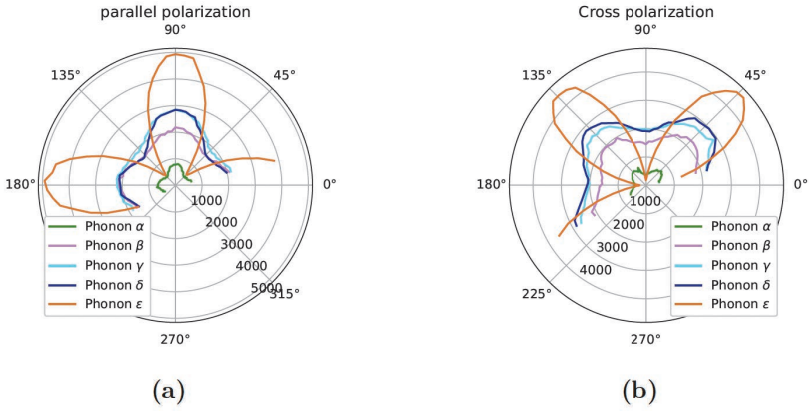

Figure 4.7: (a)Angle dependent intensities for different phonons in (a) parallel and (b) cross polarization geometries.

Another way to identify the crystallographic group is to check the angular dependence of the modes using the dependence calculated from the Raman tensor. In this section, we analyze the angle dependent intensity of the Raman mode to determine the symmetry of the crystal at low temperatures. The two potential point groups, 2/m (C_{3i}) have distinct Raman tensors representing the A_g mode. On taking the integrated intensity of the 312 cm^{-1} mode, very clear 4 fold rotational symmetry is observed with $\cos 4\theta(\sin 4\theta)$ angle dependence in the parallel(cross) polarization geometry (see Figs.4.7, 4.3, 4.4). This reconfirms that the structural point group is 2/m.

The intensities of all the other phonons show an angular dependence similar to that of the ϵ-mode at 312 cm^{-1}. However, unlike the intensity of phonon ϵ, which approaches zero for incident light polarization parallel to the crystallographic axes in cross polarization geometry, the intensities of the α-δ phonons remain at a non-zero value. As it is difficult to resolve the angle dependence of the A_g and B_g modes independently by fitting two Lorentzians, we simultaneously fit the total phonon intensity in both the parallel and cross polarization channels using the angle dependence of the sum of the $A_g + B_g$ phonons derived in table 4.3 (see Fig.4.9).

However, before fitting the intensity data to the angle dependence, the magnetic point group of the system must be considered. The magnetic ordering is

verified by the presence of a magnon at ~ 25 cm^{-1}. In case of strong magneto-elastic coupling, which is the case for α-$RuCl_3$, the low-temperature magnetic order can influence phonons. In this case, magnetic ordering can alter the azimuthal dependence by making the tensor asymmetric and by incorporating imaginary tensor elements as a result of broken time-reversal symmetry [85, 86].

4.3.3 Magnetic point group

In the paramagnetic phase, the magnetic point group of the crystal is given by the gray group 2/m1'. In the magnetically ordered phase, the possible magnetic point groups are 2'/m', 2/m', 2'/m, or 2/m .

Magnetic point group 2'/m' has a single co-representation and can be safely rejected from our choice.

The co-representations of magnetic point group 2/m' are given as [85]:

$$R(DA) = \begin{pmatrix} A & E & 0 \\ D & B & 0 \\ 0 & 0 & I \end{pmatrix} \text{ and } R(DB) = \begin{pmatrix} 0 & 0 & C \\ 0 & 0 & G \\ F & H & 0 \end{pmatrix}.$$

These tensors are defined for a unique c-axis. Given that α-$RuCl_3$ has a unique axis along the in-plane crystallographic y-direction, the co-representations of 2/m' are defined as:

$$R(DA) = \begin{pmatrix} A & 0 & E \\ 0 & B & 0 \\ D & 0 & I \end{pmatrix} \text{ and } R(DB) = \begin{pmatrix} 0 & C & 0 \\ F & 0 & G \\ 0 & H & 0 \end{pmatrix}.$$

From both these tensors, it is clear that the Raman tensors are no longer symmetric.

For point group 2'/m, the co-representations are defined as $DA \rightarrow DA'$ and $DB \rightarrow DA''$, that is, both of these magnetic point groups (2'/m and 2/m') show identical selection rules and are indistinguishable in this study. Table 4.6 tabulates the angle dependence of their respective intensities in the parallel and cross polarization channels.

In our experimental geometry, the pre-factors A, B, C, and F determine the polarization dependence. For magnetically ordered phases 2'/m and 2/m', the total intensity of the phonon observed in the parallel and cross polarization geometry is derived from table 4.6 and the data from the polarization channels are simultaneously fitted as a function of angle θ using Eq.4.4:

	DA/DA'	DB/DA''
parallel	$\lvert(A+B)+(A-B)\cos 2\theta\rvert^2$	$\lvert(C+F)\sin 2\theta\rvert^2$
cross	$\lvert(A-B)\sin 2\theta\rvert^2$	$\lvert(C-F)+(C+F)\cos 2\theta\rvert^2$

Table 4.6: Intensities of DA/DA' and DB/DA'' modes in parallel and cross polarization geometry.

$$I = (1-z)\times\left[((A+B)+(A-B)\cos 2\theta)^2+((C+F)\sin 2\theta)^2\right] + L\times z\times\left[((A-B)\sin 2\theta)^2+((C-F)+(C+F)\cos 2\theta))^2\right], \quad (4.4)$$

where

$$z = 0 \Longleftrightarrow \text{parallel polarization}$$
$$z = 1 \Longleftrightarrow \text{cross polarization}$$

L accounts for the difference between the detection efficiencies for the vertical and horizontal polarizations of light. Fig.4.8 shows the measured data in the two geometries fitted using Eq.4.4.

As shown in Fig.4.8, all our fits result in the value of $L \approx 1$ and, most importantly in $C \sim F$. Using this condition, Eq.4.4 take the form of Eq.4.5, which describes the angle dependence of the phonon modes of the colorless group, 2/m.

Therefore, the data can be fitted using Eq.4.5 which is derived from table 4.3.

$$I = (1-z)\times\left[((a+b)+(a-b)\cos 2\theta)^2+(c\sin 2\theta)^2\right] + L\times z\times\left[((a-b)\sin 2\theta)^2+(c\cos 2\theta)^2\right]. \quad (4.5)$$

Figure 4.9 shows the data fitted with Eq.4.5 and the extracted parameters. An interesting observation is the relation between parameter c of Eq.4.5 and parameters C and F of Eq.4.4. It is evident that $c = C+F$ in the fitting process, and that the Raman tensors of the colorless point group 2/m are sufficient to derive the angle dependence of the phonons even in the low temperature phase where magnetic order prevails. As the phonons at low temperature can be described using the irreducible representations of the paramagnetic point group, the magnetic symmetry should be that of a colorless group.

Our results therefore confirm the low temperature ordered zigzag phase to belong to the colorless magnetic point group group 2/m.

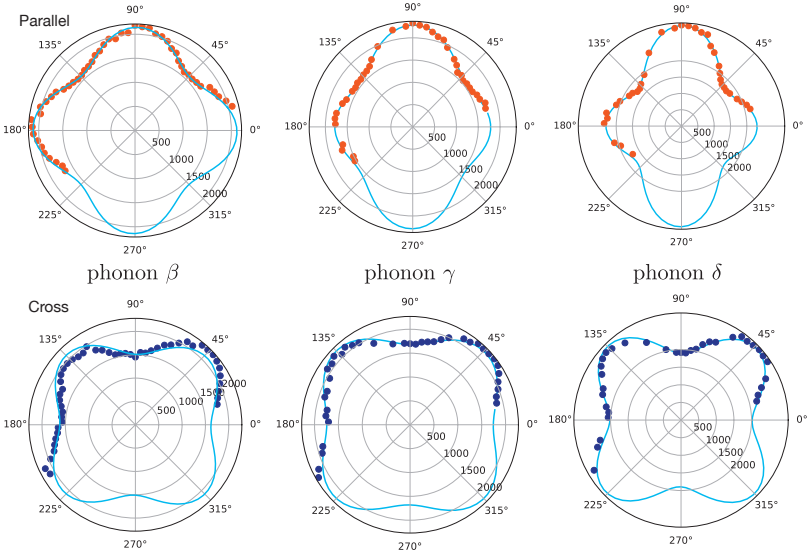

Figure 4.8: Total intensity of phonons β, γ and δ fitted usin Eq.4.4

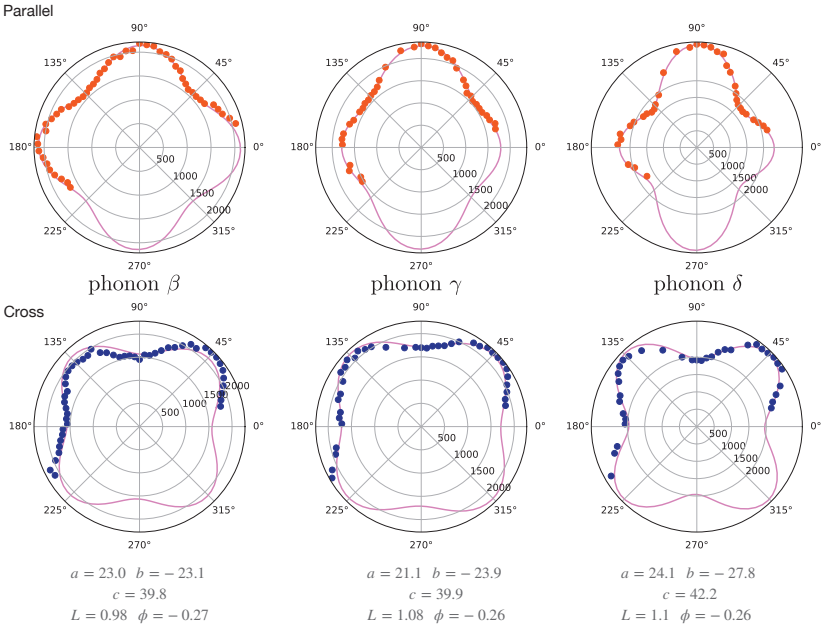

Figure 4.9: Total intensity of phonons β, γ and δ fitted using Eq.4.5

4.4 Conclusion and summary

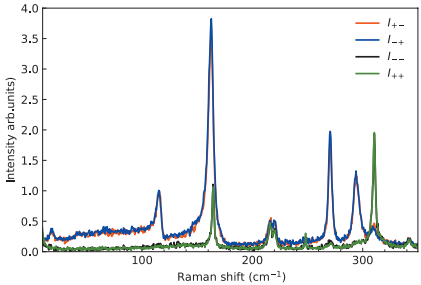

Figure 4.10: Helicity dependent scattering without an external magnetic field measured with a 532 nm laser at 1.7 K.

Using angle-dependent polarization-resolved Raman spectroscopy, we verified that the crystal structure is monoclinic with a 2/m point group. The magnetic point group is determined to be colorless. The identified magnetic group is consistent with the magnetic space group Cc2/m, as measured using inelastic neutron scattering by JOHNSON ET AL at 6 K [22, 97]. The colorless group 2/m preserves all the symmetries of the parent crystallographic point group and is described by the same irreducible representations. Therefore, no helicity dependence is expected in the low-temperature phase of the sample. As anticipated, none of the excitations showed helicity dependence in α-$RuCl_3$ without an external magnetic field (see Fig.4.10). Furthermore, we note that no splitting is observed between the four almost degenerate A_g and B_g phonons when probed with circularly polarized light in Fig.4.10. Therefore, we speculate that in previous studies use of circularly polarized light must have resulted in the modes being labelled as doubly degenerate E_g modes of the D_{3d} point group of the perfect honeycomb layer [30, 91].

Having studied the low-temperature crystal structure of the material, we are now all set to investigate the field-induced regime of α-$RuCl_3$.

Acknowledgements and Contributions

I thank Prof. Alois Loidl and Prof. Vladimir Tsurkan for providing the samples. The measurements were carried out at HFML, Netherlands with help of Mikhail A. Prosnikov, and at the university of Cologne with help of Omar Abdul-Aziz. The analysis and the text presented in this chapter is my contribution. I thank Prof. Paul H. M. van Loosdrecht, Hamoon Hedayat, Thomas C. Koethe, Vivek Lohani, and Philipp Stein for helpful discussions and inputs.

5 THE HIGH-FIELD QUANTUM DISORDERED STATE

In this chapter, we use magnetic-field dependent Raman scattering to investigate the presence of a Quantum Spin Liquid phase upon suppression of the long-range antiferromagnetic order at B_c. As discussed in CHAPTERS 1 & 3, Raman scattering is an excellent probe of Majorana fermions. Moreover, Raman scattering has resolved a zero-field low-energy broad continuum which is argued to be a signature of Majorana fermions [30, 35]. Raman scattering measurements are accompanied by terahertz spectroscopy measurements as a function of the in-plane magnetic field up to 33 T. The access to the high-field limit allows us to resolve the long-standing controversy regarding the strong field dependence of the energy of magnetic excitations, previously detected by terahertz [33] and electron spin resonance [32] (see CHAPTER 1). Supported by the exact-diagonalization calculations, we examine the character of the excitation modes to discuss the nature of the field-induced phase.

5.1 Experimental details

For this experiment, high quality α-$RuCl_3$ crystals were prepared using the vacuum sublimation method. The crystals exhibited a clear, single, phase transition at $T_N = 6.5\,\mathrm{K}$ [26, 27]. The sample was cleaved right before placing it into the cryostat to expose a shiny flat surface. High-field Raman spectroscopy was performed in a backscattering geometry with the crystal placed

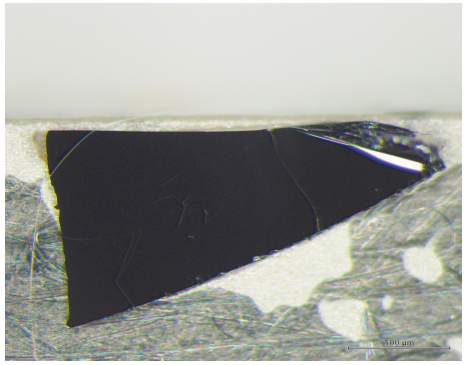

Figure 5.1: Shiny, flat surface of a cleaved α-$RuCl_3$ sample used in the experiment.

in a bath cryostat cooled to 1.7 K. Magnetic fields up to 30 T were generated using large Bitter magnets. The experiment was carried out in a Voigt geometry with B $\perp$ **k**, with the incident light vector **k** perpendicular to the **ab** -plane of the sample. The magnetic field was applied along the sample surface almost parallel to the crystallographic **a**-axis (10° away) perpendicular to the Ru-Ru bonds. A 532 nm laser was used to perform Raman spectroscopy. The light was focussed into a spot of about 2 µm on the sample surface. The laser power was restricted to 10 µW in the low-field ordered phase to avoid heating from the laser beam. The incident light was left circularly polarized, while right circularly polarized light was detected.

In order to get additional insights about the selection rules of the excitations, we compare our results with the terahertz spectroscopy experiment. These measurements were performed for fields up to 33 T with the magnetic field applied in-plane. Terahertz transmission spectra were recorded on samples with a typical **ab** surface of 3×3 mm^2 and thickness of 1 mm using a Fourier-transform spectrometer Bruker IFS-113v, with a mercury lamp as source and a silicon bolometer as detector [93].

5.2 Results and discussions

At zero-field the Raman spectra is characterized by a broad low energy continuum and higher energy phonons. In the following we will study the effect of the magnetic field on the Raman spectra.

5.2.1 Low temperature ordered phase

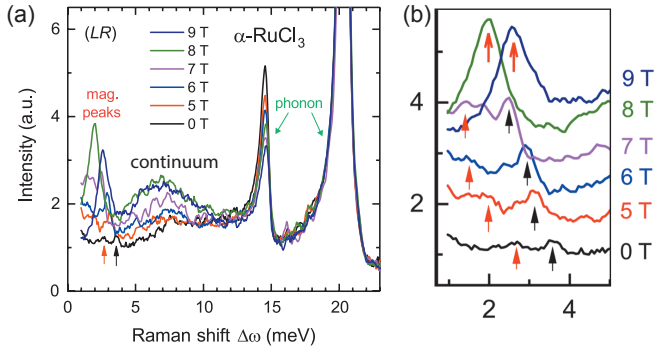

Figure 5.2: (a) Circularly polarized (LR) Raman spectra recorded at 1.7 K with low incident laser power of 10 µW in fields up to 9 T. (b) Magnetic excitations are resolved at low energies, as indicated by the arrows. The spectra of different fields are shifted upward by a constant for clarity.

To minimize the heating effects from the probe beam, the laser power was set to 10 µW. At zero field, the magnetic spectrum is dominated by a broad continuum. On top of this continuum two additional peaks at 2.7 meV and 3.6 meV are observed (see Fig.5.2). These modes are identified as excitations of the long-range order, which have been previously observed using inelastic neutron scattering [28], electron spin resonance [32], and terahertz spectroscopy [33]. These modes are single-magnon excitations at the Γ point of the zigzag (ZZ) ordered phase. Presence of these features confirm that the temperature is below T_N. On increasing the laser power to 100 µW these modes disappear which implies that the average heating from the laser is higher than 7 K. On increasing the magnetic field, these modes systematically shift to lower energies for fields up to 7 T. Above $B_c = 7.5$ T, only a single peak dominates the low energy Raman response. In particular, for 8 T, where evidence for a separate intermediate phase been reported in thermodynamic measurements [94], we find a sharp peak M1 at 2 meV in the Raman spectrum. Consistent with the terahertz results, this mode hardens continuously in higher fields above B_c (see Fig.5.2(b), 5.3(a)), without any obvious features indicating a second phase field-induced phase transition.

The effect of phase transition is also observed on the 15 meV phonon. On approaching $B_c = 7.5$ T from below, the spectral weight of the phonon at 15 meV starts to reduce. The line shape asymmetry quantified by the Fano

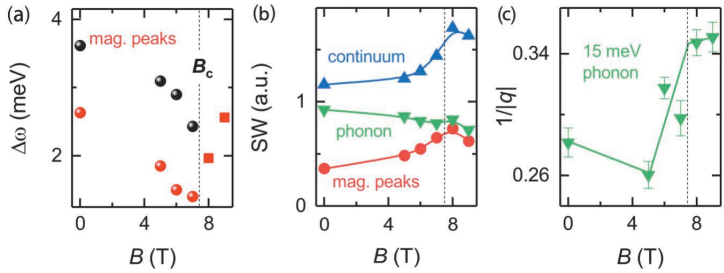

Figure 5.3: (a) Change in energy of the magnetic excitations shown in Fig.5.2(b) as a function of field. (b) Spectral weight for different frequency ranges as a function of field. (c) Fano parameter $1/|q|$ for the 15 meV phonon as a function of field. The solid lines are a guide to the eye. The dashed line in (a-c) indicates critical field $B_c = 7.5$ T.

parameter q, that is represented as $1/|q|$ of the 15 meV phonon abruptly increases close to $B_c = 7.5$ T (see Fig.5.3(c)). This represents that the 15 meV phonon modulating Ru-Ru bond is strongly coupled to the magnetic degrees of freedom. For higher fields, the continuum moves to higher energies leading to a further increase in the line-shape asymmetry, maximizing at 20 T. Above this field, the asymmetry of the phonon decreases as the spectral weight in the vicinity of the phonon energy reduces until the phonon becomes nearly symmetric at the highest field measured (see Fig.5.4(a)).

In addition to the higher energy phonons and the low energy magnons, the Raman spectrum is marked by an extended continuum, [26, 29, 30, 33, 91, 98] that shows a broad intensity maxima between 4 and 12 meV (see Fig.5.2(a)). Fig.5.3(b) shows the behavior of the spectral weight of the magnon peaks (1.2-4meV), continuum (4-12meV), and the phonon (12-15meV) in magnetic field. On approaching the phase transition, the spectral weight of the continuum and antiferromagnetic magnons is clearly enhanced while the spectral weight of the 15 meV phonon drops.

5.2.2 Excitations of the field polarized limit

From Fig.5.2, it can be observed that above the critical field, B_c, the magnons associated with the ordered phase disappear, giving way to the emergence of a new mode, denoted as M1. To enhance the signal-to-noise ratio for better resolution of high-field features, the laser power is increased to 100 µW. However, as the laser power is ramped up, M1 weakens in intensity. Notably,

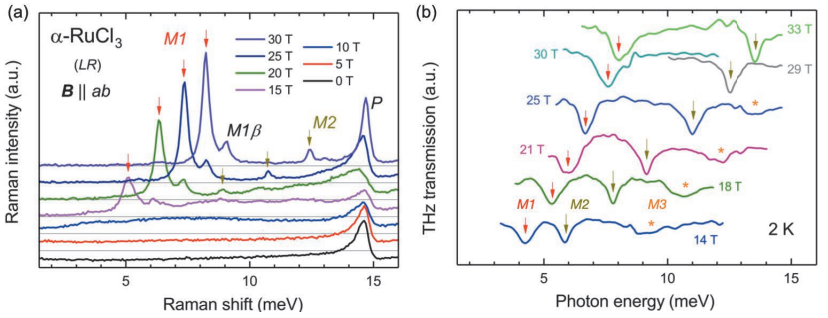

Figure 5.4: High-field (a) 100 µW LR Raman and (b) unpolarized terahertz-transmission spectra. A variety of field-dependent features are indicated (see text for details). P denotes phonon.

this mode gains strength with the application of a magnetic field and becomes more distinct beyond 15 T. Additionally, a satellite peak labeled as M1β appears at a higher energy level. With further increases in the magnetic field, both M1 and M1β peaks intensify and shift to even higher energies.

At a sufficiently high magnetic field, another sharp feature identified as M2 is resolved, located at 12.4 meV at 30 T. Notably, this feature exhibits a steeper increase in energy compared to the M1 mode.

Another feature that appears at B_c, is that the underlying continuum of excitations starts to open a gap as the lower edge of the continuum continuously shifts to a higher energy with increasing magnetic field. For instance at 15 T, the spectral weight just below 3 meV is fully depleted indicating a gap opening*. The lower edge of the continuum shows a steep increase in energy with field and the gap opens at about 14 meV at 30 T.

In Raman scattering, the continuum exhibits a somewhat broad maxima which is identified as M3 and has approximately twice the energy as M1. Similarly, a peak in the continuum energy is also observed in the terahertz measurements.

In the following, we will discuss the behavior of all the magnetic excitations observed and discuss their nature in detail.

*Gap-opening corresponds to the total depletion of the spectral weight below a certain energy. This effect has also been observed in the Raman spectra of superconductors[99, 100])

5.2.2.1 Spin-flip excitation M1

M1 is found to appear at B_c, thereby indicating a new feature. This mode is visible both in the terahertz response and in the Raman spectra which aids significantly in its identification. Based on a comparison with previous linear-polarized lower-field terahertz study [33], this mode is identified as a single particle excitation expected in the Quantum Disordered state (QDS), and is well described by the linear spin wave theory.

Assigning M1 as a single particle magnetic excitation appears surprising at first, as for conventional magnetic systems, a strong peak in Raman intensity usually occurs from the Fleury-Loudon scattering process [73] which typically results in a strong two-magnon excitation. Meanwhile, one-magnon scattering results from strong spin-orbit coupling, but usually is much weaker. Examples for this can be found in Heisenberg magnets like Sr_2IrO_4 and $Sr_3Ir_2O_7$ with strong spin-orbit coupling [101]. This happens, because the Heisenberg coupling, J_{ij} is isotropic such that the Fleury-Loudon(FL) operator $\mathcal{F}$ (see Eq:5.2) commutes with the total spin-projection $S^{\mu}_{tot} = \sum_i S^{\mu}_i$ along any direction μ. FL scattering then probes excitations with $\Delta S^{\mu}_{tot} = 0$, which corresponds to creation or annihilation of even number of magnons in a collinear magnetically ordered system (i.e $\Delta S^{\mu}_{tot} = \pm 2, \pm 4, ...$). For this reason FL is usually referred to as a two-magnon process, while Elliott-Loudon (EL) scattering which is activated by spin-orbit coupling is dominated by a one-magnon process.

The one-magnon response from the FL scattering can be understood as follows, in the field polarized limit, the Hamiltonian can be written for $|B| \to \infty$, in which case the exact ground state is an eigenstate S^{μ}_{tot}, with μ being the direction of $g \cdot B$. In this case, the terms in the Fleury-Loudon scattering operator like $S^{\mu}_i S^{\nu}_j$, with $\mu \neq \nu$, may create a spin-flip ($|\Delta S| = 1$) excitations, which correspond to single magnon excitation in the field-polarized limit. While terms like $S^{\nu}_i S^{\nu}_j$ can create up to two spin-flips. The presence of anisotropic couplings thus severely relaxes the symmetry-related restrictions for accessible excitations, generically enabling the access to single spin-flip excitations in FL Raman scattering (see supplemental material of [93]).

This makes α-$RuCl_3$ a striking example of this unusual response, where a spin-flip excitation can scatter strongly.

Large g^*- By tracing the energy of the excitation with magnetic field, an important quantity can be estimated, which is the g-factor. The slope of the energy of the excitation with the magnetic field can be defined as $g^* = \frac{1}{\mu_B}\frac{dE}{dB}$. In the large field limit $g^*|_{B\to\infty} = g_{ab}|\Delta S|$ where g_{ab} is the in-plane Landé-g

factor. Based on experimental[55] and *ab-initio* calculations[57], the value of the in-plane anisotropy is restricted between $2 \leq g_{ab} \leq 2.8$ [39, 57, 102]. The asymptotic slope therefore provides information about the character of the excitation in the high field limit.

On calculating the value of g^* for the M1 mode, close to B_c we find $g^* \geq 8$. This enormous value of slope in the intermediate field regime had been previously argued to be an evidence in favor of fractionalized excitations of the quantum spin liquid or as an apparent multi-particle bound state like character of this mode.

However, direct comparison of the slopes with the field polarized limit has two major caveats:

1. Level repulsion between M1 and the continuum can significantly increase the slope in vicinity of B_c .
2. Anisotropic coupling produces an effective easy-plane anisotropy in the quantum disordered state [58, 103]. Therefore, the slope of the single-particle excitations is expected to approach g_{ab} only asymptotically (see Ref. [104]).

On increasing the magnetic field, we found g^* continuously drops from 8 at around 10 T [33] to about 3 at 30 T. By analyzing the data over the full field range, we extract $g^*|_{B\to\infty} = 2.51 \pm 0.018$. Value of g^* in the high field limit, confirms M1 as a mode that evolves into a $\Delta S = 1$ spin-flip excitation in the infinite field limit.

M1β - Field dependence of M1β follows that of M1 with a nearly field independent energy separation of about 1 meV. It should be noted that a neutron-scattering study has revealed out-of-plane dispersion of single-particle excitation with a bandwidth of 1 meV [62]. The separation energy therefore, suggests that M1β could result from interlayer coupling.

5.2.2.2 Multi-particle excitations M2 and M3

For stronger magnetic fields, we observe that the higher energy continuum shows a somewhat broad maxima M3, which has approximately twice the energy as M1, i.e M3 $\approx$ 2M1. This identifies the lower band near M3 of the multi-particle continuum to consist predominantly of two-particle excitations.

By going to higher fields, a clearly separated M2 mode is observed, slightly below the multi-particle continuum and well above M1. The narrow linewidth of this feature with a slope little smaller than the multi-particle continuum

suggest this feature to be a two-particle bound state M2. The two-particle nature of M2 is consistent with its polarization dependence in the terahertz measurements [33, 105].

5.2.3 Exact Diagonalization

In addition to our experimental methods, exact diagonalization calculations were performed. For the numerical study, the following model of α-$RuCl_3$ was considered, containing bond-dependent, anisotropic and long-range couplings:

$$\mathcal{H} = \sum_{\langle i,j \rangle} J_1^{\gamma} \mathbf{S}_i \cdot \mathbf{S}_j + K_1^{\gamma} S_i^{\gamma} S_j^{\gamma} + \Gamma_1^{\gamma} (S_i^{\alpha} S_j^{\beta} + S_i^{\beta} S_j^{\alpha}) + \sum_{\langle\langle\langle i,j \rangle\rangle\rangle} J_3 \mathbf{S}_i \cdot \mathbf{S}_j + \sum \mathbf{g} \cdot \mathbf{B} \cdot \mathbf{S}_i \tag{5.1}$$

where $\gamma \in x, y, z$ corresponds to the type of bond connecting sites i and j and $\alpha, \beta = x, y, z/\gamma$. J_3 is the third nearest neighbor coupling. B is the external magnetic field and g the anisotropic g-tensor.

The calculations were performed on a 24-site cluster with parameters based on ab-initio studies [57, 106–109] (see supplemental material of [93]).

The Raman intensity $I_{\mathcal{F}}(\omega) = \int dt e^{-i\omega t} \langle \mathcal{F}(t) \mathcal{F}(0) \rangle$ was evaluated using the FL approach [73] with scattering operator

$$\mathcal{F} \propto \sum_{ij} \mathbf{S}_i \cdot \mathbf{J}_{ij} \cdot \mathbf{S}_j (\boldsymbol{\delta}_{ij} \cdot \mathbf{E}_{\text{in}})(\boldsymbol{\delta}_{ij} \cdot \mathbf{E}^*_{\text{out}}) \tag{5.2}$$

Where $\mathbf{J}_{ij}$ contains generic coupling between $\mathbf{S}_i$ and $\mathbf{S}_j$, $\boldsymbol{\delta}_{ij}$ is the distance between sites i and j and $\mathbf{E}_{in}$ ($\mathbf{E}_{out}$) corresponds to the direction of incident(outgoing) light. The model used in Fig.5.5 employs the broken C_3 symmetry ($K^x = K^y \neq K^z$), motivated by *ab initio* calculations [106] for a C2/m structure of the material. Results from the model capturing the strong field-dependence of g^* is presented in Fig.5.5, in this model the parameters are given as:

$(J_1, K_1^{x,y}, K_2^z, \Gamma_1, J_3) = (-0.5, -7.5, -5, 2.5, 0.5) \times 1.5\,\text{meV}$.

The ED study is found to reproduce the essential features of the Raman measurements: At $B < B_c$ a continuum of excitations extending over a wide energy range is observed. For $B > B_c$, the lower bound of continuum quickly rises in energy, and a strong single-particle mode M1 emerges, becoming the most intense excitation at the high-field. The multi-particle continuum is

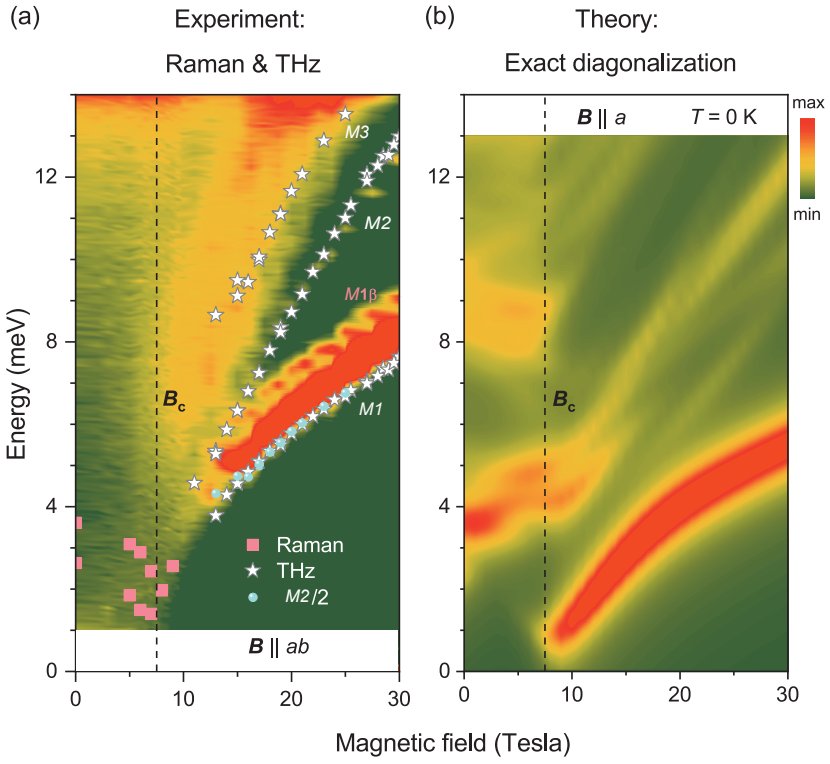

Figure 5.5: Contour plot of experimental 100 µW Raman intensity of α-$RuCl_3$ as a function of in-plane field [from Fig.5.4(a)]. Peak positions obtained in the low-field 10 µW Raman spectra ($B \leq 9$ T) [Fig.5.3(a)] and in the high-field terahertz spectra ($B \geq 10$ T) [Fig.5.4(b)] are shown by symbols for comparison. (b) Theoretical T = 0 Raman response within the Fleury-Loudon approximation [73] of a C_3-broken model for B ∥ a assuming $g_{ab} = 2.3$ (see supplemental material of Ref.[93])

also reproduced in ED; however, the existence of a distinct bound state M2 separate from the continuum is difficult to assess in ED, due to the discrete nature of the computed spectra on finite-size clusters.

As observed in the experiment a continuum extends throughout a wide energy range below B_c in the numerical results. For $B > B_c$ the continuum rises in energy. Above B_c, a strong, sharp mode emerges at the lowest energies, which shifts to higher energies and becomes the most intense excitation at high fields.

This mode follows the excitation-gap opening similar to the M1 mode. The contributions of the Heisenberg and the off-diagonal exchange terms have been studied separately (see Supplemental Material of Ref.[93]), and it confirmed that the Kitaev and the off-diagonal exchanges in $\mathcal{F}$ can explain the unusual strength of the single-particle excitation in the Raman response.

5.2.4 Summary and conclusions

We observe that the high-field phase which appears on suppressing the antiferromagnetic order is neither a quantum spin liquid nor a fully field-polarized phase, but rather a quantum disordered phase with partially aligned spin-orbital moments. In these experiments, no clear evidence of an intermediate field regime is observed around 7.5 T. The high-field phase is characterized by a strong and sharp single-particle excitation and a continuum of multi-particle nature, out of which a well-defined two-particle bound state emerges, best visible at higher fields. The g^* of the M1 mode asymptotically approaches the desired slope of the field polarized limit which confirms that the sharp single-particle excitation is identified as a spin-flip excitation of the field-polarized regime. A comparison of experimental and exact-diagonalization results clearly demonstrates the importance of Kitaev and off-diagonal interactions in α-$RuCl_3$. Similar results are expected in other Kitaev candidates such as the iridates.

The results obtained in this chapter are inline with the contemporary findings of the electron spin resonance experiment [110] which does not report of an intermediate field regime. However, in another experimental report on Raman scattering by Wulferding et al the authors report of a Quantum Spin Liquid phase in the intermediate field regime, based on the observation of an excitation, which they claim to be a Majorana Bound state. This excitation has not been observed in our results thus far. In the next chapter we investigate the chirality of the magnetic excitations. Through this study, we will establish the presence of a distinct intermediate field regime.

Contributions

The text written in this chapter derives from Sahasrabudhe et al (Phys. Rev. B 101, 140410(R))[93]. The contents can be categorized into three rather independent sub-projects which are described below:

1. Raman scattering

The high-field Raman scattering experiment was conceived by Paul H. M. van Loosdrecht and Markus Grüninger as a collaborative project under CRC1238. Petra Becker, Vladimir Tsurkan and Alois Loidl provided the samples. I along with Raphael German and Thomas Koethe performed the experiment at the High Field Magnet Lab (HFML), Netherlands with Jonathan Buhot. I, Raphael German, Thomas Koethe and Zhe Wang analyzed the Raman data.

2. Terahertz spectroscopy

terahertz spectroscopy data was provided by Stephan Reschke, Seung-Hwan Do, Kwang-Yong Choi, and Zhe Wang. The measurements were performed at the HFML, Netherlands with Dimitri Kamenskyi.

3. Exact Diagonalization

Exact diagonalization calculations were done by David Kaib, Stephen M. Winter and Roser Valenti at the Institute of theoretical physics Frankfurt and by Ciarán Hickey at the Institute of theoretical physics Cologne.

The manuscript was written by Zhe Wang with contributions from Markus Grüninger, Ciarán Hickey, Paul H.M van Loosdrecht, Roser Valenti, Stephen M. Winter, David Kaib, Thomas C. Koethe and me.

6 CHIRAL EXCITATIONS IN THE FIELD-INDUCED PHASE

> I call any geometrical figure, or group of points, 'chiral', and say that it has chirality if its image in a plane mirror, ideally realized, cannot be brought to coincide with itself. -Lord Kelvin 1893

The interest in α-$RuCl_3$ surged following Jackeli and Khaliullin's groundbreaking work, where they identified key material properties that mimic the Kitaev model. However, a distinct field regime conducive to the Kitaev Quantum Spin Liquid Phase above the antiferromagnetically ordered ZZ phase has so far remained elusive. In the field regime of $7.5(5) - 11$T thermal conductivity measurements [36, 111, 112] have displayed a direct signature of a chiral Majorana edge mode (and hence of a QSL) -- viz. a half-integer quantized plateau in the transverse heat conductivity [37, 38, 113]. However, half-integer quantisation of the thermal conductivity and consequently the role of Majorana fermions as heat carriers has been challenged [114–116]. Meanwhile, thermodynamic experiments like thermal expansion, magnetostriction, and the magnetocaloric effect provide conflicting conclusions about the presence of the QSL phase in the field regime of 7.5(5) T to 11 T for field applied parallel to the honeycomb plane [62, 117–119]. Recent evidence in favor of the QSL phase comes from the observation of oscillations of the thermal conductivity in this field regime [115].

When studied using spectroscopic experiments, α-$RuCl_3$ shows a low-energy multi-particle continuum proposed to be of Majorana fermions [30, 35, 44]. As presented in the previous chapter, upon suppression of the antiferromagnetic

ZZ phase in a large external magnetic field, the continuum acquires a gap and the spectrum exhibits a sharp excitation that is smoothly connected to a spin-flip excitation in the field-polarized limit [93]. Altogether, most of the spectroscopic data reported thus far do not provide any signature of a distinct Intemediate Field Regime (IFR) [32, 33, 93, 110, 120]between 7.5(5) T to 11 T . However, in yet another Raman scattering experiment performed at 2 K in magnetic field, Wulferding et al.[94] observed an excitation which they interpreted as a Majorana bound state. In this experiment, the field was tilted by 18° out of the honeycomb plane and the measurements were restricted to 10 T. Hence the data could not capture any possible difference between the high-field and the intermediate field regime.

Raman scattering is expected to be an effective probe for emergent Majorana fermions [34, 35, 77] and anyonic excitations. Experiments performed by Pinczuk et al. [121] have already demonstrated the strength of Raman scattering in probing the emergent anyonic excitations of the fractional quantum Hall effect [121–123]. Recently, it has been suggested that these anyonic excitations are chiral and may show fingerprints in helicity-dependent Raman scattering [124, 125]. Inspired by these ideas we performed helicity dependent Raman scattering on α-$RuCl_3$. The blueprint for this is to compare the Raman intensities for circularly polarized light [78] in the four different polarization geometries $I_{++}, I_{--}, I_{+-}, I_{-+}$, where the first (second) index denotes the circular polarization of the incident (scattered) light. As the continuum and the magnetic excitations in α-$RuCl_3$ do not scatter in I_{++} and I_{--} (see Appendix III), we focus on the Raman Optical Activity (ROA) defined as:

$$\mathrm{ROA} = \frac{I_{+-} - I_{-+}}{I_{+-} + I_{-+}} \tag{6.1}$$

ROA is a detectable quantity that is intimately connected with the chirality of excitations [78, 126, 127]. Chiral excitations possess handedness and are asymmetric under inversion. For example, let us consider magnons. Magnons in a ferromagnet are chiral and are right circularly polarized with respect to the direction of magnetization [128], while antiferromagnets have two degenerate magnon branches with opposite chirality. In the particular case of a ferromagnet, only one of the two incident polarizations σ^+ and σ^- yields a Raman signal and this shows ROA = 1 [88, 129, 130]. In antiferromagnets, an external magnetic field can lift the degeneracy of magnons which can again be detected using ROA [79].

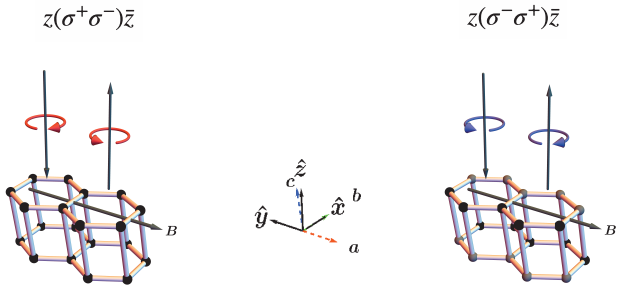

Figure 6.1: Schematic of experimental geometry for measuring the helicity-resolved Raman intensities in I_{+-} and I_{-+} channels.

6.1 Experimental details

For these experiments, high quality single crystals of α-$RuCl_3$ were prepared by the vacuum sublimation method [26]. A monoclinic C2/m structure is confirmed using polarized Raman spectroscopy (see Chapter 4). The sample is placed in a bath cryostat, and immersed in Helium gas to achieve a temperature of 1.7 K. The magnetic field is applied within the **ab**-plane, perpendicular to a Ru-Ru bond. The light polarization is defined with respect to the **z** axis. Left (right) circular light is represented as σ^+ (σ^-) as it projects spin angular momentum $+\hbar(-\hbar)$ onto the quantisation axis. To achieve the desired polarization, the incident light is passed through a linear polarizer followed by a quarter wave plate (QWP) at 45° (−45°) to create left (right) circularly polarised light. The back-scattered light is passed through a second QWP at 45° (−45°) and a vertical polarizer before the spectrometer to collect right (left) circularly polarised light. The experimental geometry is defined using the Porto notation as $z(\sigma^+\sigma^-)\bar{z}$ and $z(\sigma^-\sigma^+)\bar{z}$, see Fig.6.1. We refer to the corresponding Raman intensities as I_{+-} and I_{-+}, respectively. The data have been normalized in the range of the higher-energy phonons from 27 meV to 43 meV.

6.2 Results

Figure 6.2(a) shows the helicity-dependent Raman response for $B > B_c$ (= 7.5 T). Overall, the observed features agree with previous Raman results

[93, 94]*. The data show the magnetic modes M0, M1, M2, and M3, and a broad magnetic multi-particle continuum. The M0 peak has been observed by Wulferding *et al.*[94] for out-of-plane magnetic fields up to 10 T. They attributed this feature to a singlet Majorana bound state as its excitation energy remained insensitive to the magnetic field. In the fully spin-polarized limit, i.e., for infinite magnetic field, the M1 mode has been identified as a spin-flip excitation with $|\Delta S| = 1$, while M2 has been attributed to a two-particle bound state [93, 94]. The feature M3 has been interpreted either as a two-particle excitation since its energy at high fields roughly equals twice the energy of M1 [93] or as a three-particle bound state[94]. We emphasize that this picture applies to the high-field limit [93, 94, 110].

6.2.1 Helicity dependence

From the helicity dependence, it is immediately clear that the magnetic features M0, M1, M2, and M3 exhibit chirality. The effect of magnetic field on the chirality of these excitations allows us to distinguish different regimes. To this end, Fig.6.2(b) depicts the ROA on a color scale. We first focus on the ROA of M1, which can be continuously traced down to B_c. Values for ROA are obtained via Eq.6.1, using the integrated intensities obtained by fitting a Lorentzian to the M1 mode in I_{+-} and I_{-+} (see Appendix III). The result is depicted in Fig.6.2(c), which reveals three distinct trends in the ROA of M1. We find a clear plateau with ROA ~ 1 from 7.5 T to 10.5 T in the IFR, a continuous decrease in ROA in the transition regime from 10.5 T to 15 T, and ROA~ 0 in the high-field regime above 15 T.

Supporting evidence for the thus identified onset of the high-field regime at 15 T emanates from the behavior of M0, M2, and M3, see Fig.6.2. The ROA of M2 crosses zero around 15 T and undergoes a drastic change from ROA $= -1$ at 10.5 T to ROA $= +1$ at 18 T. Concerning M3, a clear peak is only identified above 15 T, while a consistent broad feature is visible from 10.5 T (see Fig.6.2(b).). In contrast, M0 is only detected below 15 T where it shows a negative ROA (cf. Fig.6.2(b), Fig.6.2(d).). As we do not observe any pronounced changes in ROA of these features from 15 T to 30 T (see Appendix III) we identify $B \sim 15$ T as the onset of the high-field regime.

Having identified the high-field regime, we now discuss the observations of the IFR. Apart from a fully chiral M1, the only other chiral excitation that is

*The features M1, M2, and M3 correspond to $m1\alpha$, $m2\gamma$, and $m2\alpha$ in Ref. [15] and to M1, 2M, and 3M in Ref. [31], while M0 corresponds to MB in Ref. [31]. Note that previous data were reported in I_{+-} [15] and I_{-+} channels [31]. Due to the pronounced ROA for intermediate fields, not all features are discussed in all previous studies

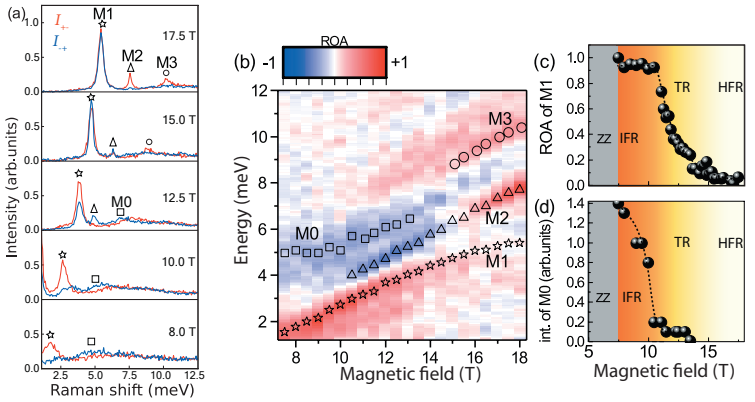

Figure 6.2: (a) ROA as a function of energy and field. Symbols denote the peak energies of M0, M1, M2, and M3. (b) ROA of the M1 mode. The different trends in the ROA of M1 can be used to determine the three distinct magnetic-field regimes. Orange region: IFR with ROA= 1; color gradient: transition regime (TR); white region: high-field regime (HFR) with ROA$\sim$ 0. The grey shaded region indicates the ordered ZZ phase. Dashed lines: guide to the eye. (c) Integrated intensity of the M0 mode as a function of magnetic field. In all three panels, error bars are smaller than or equal to the symbol size.

observed in this regime is M0. The energy (open squares) and the integrated intensity of the M0 mode are plotted in figures 6.2(b) and 6.2(d), respectively. From 7.5 to 10.5 T, the energy of M0 remains constant, while the intensity shows a pronounced decrease. Above 10.5 T, M2 starts to peak in the energy window of M0, requiring two Lorentzians to account for the presence of both peaks. Simultaneously, the excitation energy of M0 starts to increase linearly with B with almost the same slope as M2. In summary, all relevant excitations (M0, M1 and M2) show distinct changes at 10.5 T, providing clear spectroscopic evidence for the existence of an IFR.

6.2.2 Temperature dependence

After identifying the magnetic-field range of the IFR in our Raman data, we turn to the sensitivity of this phase to temperature, focusing on the properties of the chiral excitations M0 and M1. The temperature dependence is examined by varying the power of the incident light so as to avoid a mechanical drift of the sample. We estimate that 40 and 100 µW correspond to 7 and

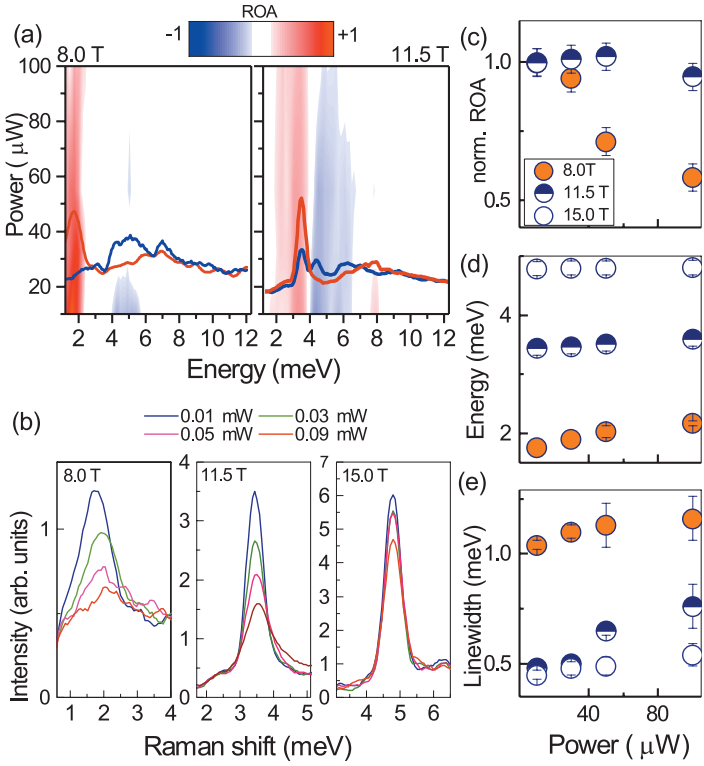

Figure 6.3: (a) Power dependence of ROA at 8 T and 11.5 T. Red (blue) areas represent larger scattering in I_{+-} (I_{-+}). As a reference, the red and blue solid lines show I_{+-} and I_{-+} at 10 μW. At 8 T, the M1 mode in the I_{+-} channel shows maximum power sensitivity around 40 μW (T $\sim$ 7 K), while M0 in the I_{-+} channel disappears around 20 μW (T $<$ 7 K). (b) Effect of laser power on M1 in I_{+-} in different field regimes. (c) Power-induced change in ROA of M1 at 8 T and 11.5 T. (d),(e) Power dependence of energy and linewidth of the M1 mode in I_{+-} channel.

13 K, respectively [†]. Measurements of the power-dependence of the spectra yield an insight into the temperature dependence of the observed ROA. Figure 6.3(a) exemplifies the power-dependent change of ROA at 8 T and 11.5 T, i.e., inside and just above the IFR, respectively. For ease of visualization, we have superimposed smoothened reference spectra taken at 10 µW. At 8 T, the spectra show M1 and M0 around 1.5 meV and 5 meV, respectively, cf. Fig.6.3(a). At 11.5 T, the peaks are shifted to around 3.2 meV and 6.0 meV while M2 appears around 4.5 meV. The color plot again pinpoints the opposite chiralities of M1 and M0. The power dependence reveals a further key difference between 8 T and 11.5 T. In the IFR at 8 T, the chiralities of both M1 and M0 rapidly decline with increasing laser power, i.e., sample temperature. In contrast, the ROA of both modes is less sensitive to the laser power at 11.5 T. This is highlighted in Fig.6.3(c), showing the normalised ROA of M1. At 40 µW ($\approx$ 7 K), the ROA of M1 is suppressed by more than a factor of two at 8 T but remains unaffected at 11.5 T.

Figure 6.3(b) shows the smoothened spectrum of M1 as observed in I_{+-}, while Fig.6.3(d) and 6.3(e) show the energy and the linewidth of M1 as a function of power for different fields, obtained by fitting M1 in I_{+-} with a Lorentzian. The energy of M1 hardens with increasing laser power at 8 T. Again, this behavior is found to be unique to the IFR. Furthermore, the linewidth of M1 is much larger at 8 T than at higher fields.

6.3 Discussions and conclusions

Previous Raman scattering studies on α-$RuCl_3$ in high magnetic fields, like the previous chapter, reported on I_{+-} [93] and on I_{-+} [94]. Due to the chiral character of the magnetic excitations, e.g., M0 and M1 showing opposite chirality, the key to a comprehensive picture of the magnetic Raman features and to a thorough understanding of the spectra lies in the comparison of the I_{+-} and I_{-+} channels, i.e., in the ROA. In particular the ROA data measured over a wide range of magnetic fields above B_c allow us to unravel the distinct spectroscopic characteristics of the intermediate-field regime and to elucidate its properties.

The IFR is characterized by the presence of the two excitations M0 and M1 for which we find an opposite chirality. Furthermore, ROA=+1 for M1 within

[†]We use a base temperature of 1.7 K. Via the suppression of the magnon intensity, we estimate the local sample temperature at the laser spot to be$T_N \sim 7$ K at 40 µW. Comparing Stokes and anti-Stokes scattering, we find $\sim$ 25 K at 250 µW. See Appendix III.

the IFR. To illustrate the importance of M0 and M1 being chiral, we consider the case of a simple paramagnet instead of a QSL above 7.5 T, where long-range zigzag order is suppressed by the magnetic field. The external magnetic field competes with exchange interactions. In this paramagnet scenario, it is feasible to neglect field-induced order at B_c and assume that the time-average of the local magnetic moments tends to zero. In this case, the Raman tensor R of the excitations is defined by the crystallographic space group C2/m [44]. The Raman intensity is given by $I_{is} = |e_s^\dagger \cdot \mathcal{R} \cdot e_i|^2$, where e_s and e_i are the electric field vectors of the scattered and the incident light. Since the crystallographic space group is achiral, we find $I_{+-} = I_{-+}$ and ROA = 0, see Appendix III. The pronounced ROA of the magnetic excitations M0 and M1 in the IFR indicate an unconventional ground state distinct from a conventional paramagnet.

Previously, M0 has been attributed to a singlet Majorana bound state [94]. While our results do not provide any direct evidence for a Majorana character, the large width of M0 speaks against a strict bound-state scenario but rather suggests a resonance within the continuum close to its lower edge.

The mode M1 has been identified as a spin-flip excitation in the high-field regime [93]. Above 15 T, the ROA of M1 nearly vanishes. The pronounced increase of the ROA with decreasing field and in particular the plateau with ROA=1 in the IFR are clear signatures of a change of character of this mode. Remarkably, the plateau is observed between 7.5 T to 10.5 T, consistent with the intermediate field regime where a QSL phase has been proposed to exist [36, 62, 111, 112, 115]. Remarkably, the linewidth γ of the M1 mode equals 0.5 meV in the high-field regime where it corresponds to a spin flip, see Fig.6.3(b). In the IFR, γ is enhanced by more than a factor of two. It is tempting to explain this increase of the linewidth in a scenario based on Majorana fermions, where the local spins decay into Majoranas and fluxes, giving rise to a substantial broadening of M1. However, at this point the role of other scattering channels, for example spin-phonon scattering, cannot be ruled out.

Lastly, we briefly comment on the nature of the M2 and M3 modes in the high-field phase. They both show a pronounced ROA, where the ROA of the M2 mode even changes sign at about 15 T. This observation is interesting in view of the prediction of the presence of topological magnons in the field-polarized phase of a Kitaev-Heisenberg magnet [131–133].

In conclusion, magnetic field and laser power dependent Raman optical activity experiments show the presence of distinct field induced phases for α-$RuCl_3$. In particular, the upper limit of our identified intermediate field regime is very close to the value of 11 T, above which the quantum oscillations intrinsic to

a QSL phase vanish [115]. The intermediate field regime shows intriguing spectroscopic features. The most salient features are a fully chiral response (ROA=1) of the strongest (M1) magnetic mode and the presence of a resonance mode (M0) on the lower edge of the magnetic Raman continuum which previously has been discussed in terms of a Majorana bound state [94]. The large width of both modes may suggest a fractional character of the fundamental magnetic excitations specific for the IFR but at the same time speaks against a bound-state scenario. The laser power dependence (i.e., temperature dependence) of the spectra indicates that the ground state in the IFR region is rather fragile as is demonstrated by the rapid decrease of the fully chiral response upon increasing temperature. In contrast, the ROA of the spectra in the high field regime is hardly affected by the increased temperature. Though it is clear from the present and earlier experiments that the IFR has an unconventional ground state which could very well be a quantum spin-liquid state, its exact nature remains elusive at this point. The present work shows the power of ROA experiments in materials showing unconventional magnetism and sheds light on the intriguing chiral magnetic properties of the Kitaev-Heisenberg magnet α-$RuCl_3$, inspiring future research to realize a field-induced spin-liquid phase in α-$RuCl_3$ and other Kitaev-like systems.

In summary, ROA of magnetic excitations provides a rough guide to resolve distinct field regimes in α-$RuCl_3$. Such a resolution is further corroborated by the onset(vanishing) of additional features. To the best of our knowledge, a theoretical study capturing these fascinating spectroscopic signatures of magnetic excitations beyond the low-field phase of α-$RuCl_3$ is still missing. We hope that our findings motivate future work to further explore the underlying physics that is reflected in the chirality of these excitations. In the next chapter, we will investigate the effect of magnetic field on the chirality of the phonons.

Acknowledgements and contributions

Main results of this chapter are presented in a preprint titled "Chiral excitations and the intermediate-field regime in the Kitaev magnet α-$RuCl_3$" by Sahasrabudhe et al [134]. This paper is published under a Creative Commons Attribution (CC BY 4.0) International License.

The conceptualization of this study was led by me and Paul H. M. van Loosdrecht. Vladimir Tsurkan and Alois Loidl provided the samples. The experiment was performed in December of 2020, when Corona was rampant and lead to travel bans. As a result, I could only join Mikhail Prosnikov virtually

to perform the experiment at the High Field Magnet Lab (HFML), Netherlands, with Mikhail Prosnikov leading the experiment. I analyzed the Raman data with inputs from Hamoon Hedayat and Paul H. M. van Loosdrecht. The presented manuscript is written by me, Markus Gruninger, and Hamoon Hedayat with inputs from Paul H. M. van Loosdrecht, Philipp Stein, Thomas Koethe, Mikhail Prosnikov, Fulvio Parmigiani and Daniel Khomskii.

I thank Jonathan Buhot and Clément Faugeras for supporting preliminary experimental measurements. I acknowldge insightful discussions with Roser Valenti, David Kaib, Aprem Joy, Ciarán Hickey and Vivek Lohani.

7

PHONONS IN THE FIELD-INDUCED PHASE

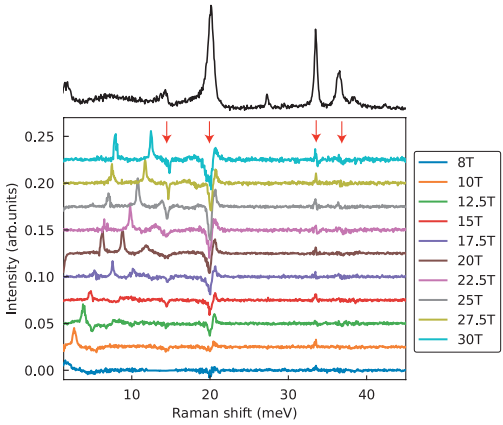

Figure 7.1: Difference spectrum ($I_{+-} - I_{-+}$) of α-$RuCl_3$ as a function of the magnetic field. The black line is a reference spectrum measured at 7.5 T. The red arrows show the positions of the phonons. The higher energy phonons do not show helicity dependence. The phonons at 14 meV and 20 meV show maximal difference.

In CHAPTER 5 we have seen that as the magnetic field suppresses the long-range zigzag order, the multi-particle continuum opens a gap and a new magnetic excitation M1 emerges. At higher magnetic fields, it is accompanied by spectral features M2 and M3, which are magnetic excitations of multi-particle nature. In CHAPTER 6 we saw that the these magnetic excitations exhibit

helicity-dependent scattering. Thus far, only the evolution of magnetic excitations have been discussed. In this chapter, we discuss the helicity dependence exhibited by the phonons*.

Fig.7.1 shows the differential intensity measured between the I_{+-} and the I_{-+} channel. From the difference plot it is clear that only the two lower energy phonons show helicity dependence, while the higher energy phonons remain insensitive to the incident helicity. The phonons at 116 cm^{-1} ($\sim$ 14.5 meV) and 160 cm^{-1} ($\sim$ 20 meV) that exhibit significant helicity dependence are referred to as phonon α and phonon β, respectively. When $B < B_c$ these phonons do not exhibit helicity dependence and show an identical spectrum in both helicity channels. However, upon cranking up the magnetic field, these two phonons begin to show helicity-dependent scattering, with the intensity, energy and lineshape depending on the measurement channel.

Next, Fig.7.2 shows the helicity resolved evolution of the phonons as a function of the magnetic field. As the magnetic field increases, significant changes appear in their lineshape. One striking observation is the lineshape of phonon α at 30 T, where it shows a pronounced double peak-like structure. We will address the origin of the double-peak lineshape in this chapter and speculate on the origin of chiral phonons.

7.1 Results & discussion

We observe that the phonons at 116 cm^{-1} ($\sim$ 14.5 meV) and 160 cm^{-1} ($\sim$ 20 meV) exhibit helicity dependence. Fig.7.2 shows the increase in the helicity dependence of the phonons with increasing magnetic field. Both the phonons show strongly suppressed intensity in the I_{+-} channel compared to the I_{-+} channel. The effects are particularly strong for phonon α, where the intensity of the phonon completely vanishes from the I_{+-} channel. The phonon eventually reemerges as a double-peak structure with a further increase in the magnetic field. In the following subsections we will discuss these two effects in more detail.

7.1.1 Chiral phonons

Chiral phonons are particularly interesting as phonons typically do no carry any angular momentum. Only recently, some experimental studies have verified chiral phonons in two dimensional hexagonal systems [127, 135–137]. In

*The experimental setting is identical to Sec.6.1

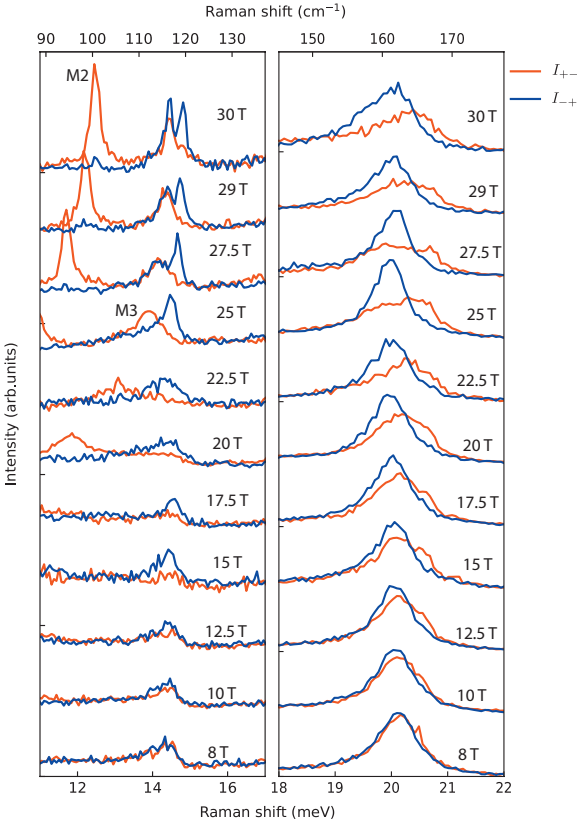

Figure 7.2: Effect of magnetic field on phonons at 116 cm^{-1} ($\sim$ 14.5 meV) and 160 cm^{-1} ($\sim$ 20 meV). The effect is compared between the two helicity channels I_{+-} and I_{-+} which are plotted using the red and the blue lines respectively. The phonons are shifted by a constant offset along the y-axis for better clarity. Both the phonons show a stronger helicity dependence for an increasing magnetic field. The data are measured at 1.7 K.

most of these systems, chiral phonons are linear combinations of the doubly-degenerate E_g phonons that exhibit clockwise and counterclockwise rotational vibrations corresponding to angular momenta of $l = \pm 1$.

However, as we saw in CHAPTER 4, the three-fold symmetry of α-$RuCl_3$ is reduced to two-fold and that the phonons of α-$RuCl_3$ are labeled as A_g and B_g phonons of the point group C_{2h}. The linearly polarized A_g and B_g phonons do not carry any angular momentum and cannot show chirality. Nevertheless, the nearly degenerate phonon modes with the A_g and B_g representations of the point group C_{2h} originate from the E_g representation of the D_{3d} point group that describes the perfect hexagonal layer [44, 48]. The phonons α and β are two out of the four almost degenerate pairs of the A_g and B_g phonons that are observed in the spectrum as a result a chiral response from these phonons seems unlikely.

Now we now know from CUI ET AL [138] that a coherent superposition of the nearly degenerate A_g and B_g modes with a phase factor of $\pm\pi/2$ can lead to chiral, circular phonons that carry opposite non-zero angular momenta given by $L^z_\pm = \mp\hbar|\epsilon_1 \pm i\epsilon_2|^2$, where ϵ_1 and ϵ_2 are polarization vectors of A_g and B_g phonons. Thus, we identify that the observed phonons are superpositions of the degenerate left and right circularly polarized phonons which carry non-zero angular momentum.

These circular phonons are expected to remain degenerate even under an external magnetic field due to their small orbital phononic magnetic momenta [138]. However, it is possible that coupling to continuum can effectively lift the degeneracy between the two circularly polarized phonons with opposite angular momenta under a finite magnetic field.

We next discuss the coupling between the chiral phonons and the continuum. As the phonons exhibiting chirality are in the vicinity of the continuum, we investigate the role of the continuum in splitting the degeneracy of the phonons and in inducing chirality in the phonons. Both the phonons (α and β) display a distinctive lineshape characterized by an asymmetric line broadening at the lower-energy edge and a concomitant dip in intensity at the higher-energy edge. This lineshape is indicative of an interaction between the vibrational mode and the multiparticle continuum. The asymmetric lineshape is described by the Fano model [139]:

$$I = I_0 \frac{(q+\epsilon)^2}{1+\epsilon^2}, \tag{7.1}$$

with Fano parameter q and reduced energy ϵ. The reduced energy ϵ quantifies the difference between the uncoupled phonon frequency (ω_{res}) and the

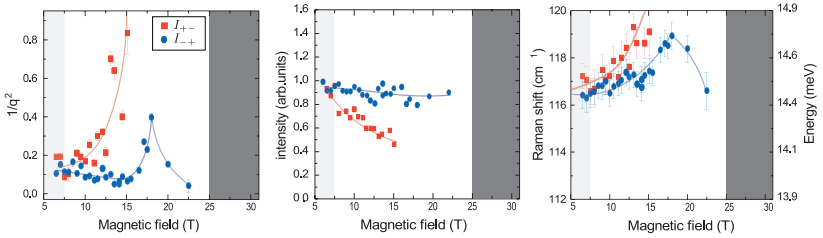

Figure 7.3: Fano parameters for phonon α. The phonon shows stronger coupling to the continuum in the I_{+-} channel, than in in the I_{-+} channel. Additionally, the intensity of the phonon drops as the coupling between the phonon-continuum increases. This observation indicates a chirality selective coupling between the phonon and the continuum. The field regime, where the double peak structure appears is colored with dark grey.

observed energy ω ($\epsilon = \omega - \omega_{\text{res}}$). The coupling strength to the continuum is given by $1/q^2$. A large value of $1/q^2$ represents larger asymmetry in the lineshape. As the value of $1/q^2 \to 0$, the peak becomes symmetric.

In order to investigate the role of the coupling to the continuum in the resulting helicity dependence, we fitted phonon α as observed in the I_{+-} and the I_{-+} channel using the Fano model described in Eq.7.1. The coupling strength obtained from fitting a Fano function to phonon α is plotted as a function of the magnetic field in Fig.7.3. The field dependent change in the coupling strength is found to be different for the two helicity channels. In the I_{-+} channel, the coupling peaks at 17.5 T before dropping to zero. In the I_{+-} channel, the Fano parameter strongly diverges with the magnetic field. Concomitantly, the intensity of the phonon in the I_{+-} channel washes out. As a result, it appears that the increase in phonon-continuum coupling is responsible for washing out the phonon in I_{+-} channel and in the resulting helicity dependence.

This is particularly interesting because the continuum by itself does not exhibit chirality, but the left and right-handed excitations of the continuum appear to selectively couple with the degenerate left and right-handed circular phonons.

In the next section, we will discuss the formation of a double-peak structure in the energy regime of phonon α.

7.1.2 Phonon-M3 hybridization

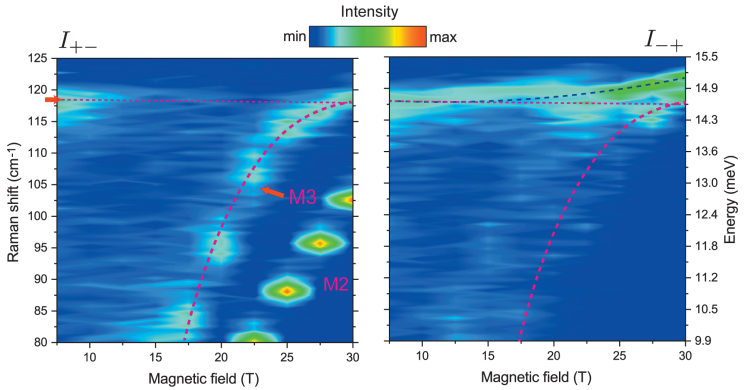

Figure 7.4: Color plots of phonon α in the I_{+-} and the I_{-+} geometry. The dotted line shows the energy of phonon A at 7.5 T. Hybridization between the phonon and the M3 mode is observed in the I_{+-} channel. As a consequence of hybridization the phonon gains intensity and an additional peak in the I_{-+} channel. Note: the seemingly discrete steps in plot are an artifact from our discretely spaced measurements. In the I_{-+} channel, the red dotted line is a guide to eye and shows the evolution of M3, as obtained from the I_{+-} channel. The blue dotted line follows the evolution of phonon α in the magnetic field.

Fig.7.4 shows the change in the intensity and the energy of the excitations with the magnetic field. The two subplots correspond to the response from the two helicity channels that are used in the experiment, i.e., I_{+-} and I_{-+}. The red thin dotted line shows the energy of the phonon at 0 T, and the thick dotted line shows the energy of M3 with the magnetic field. As $B \to 25$ T, the energy of the M3 mode reaches the energy of the phonon. As a result, in the I_{+-} channel the intensity in the energy range of the phonon starts to increase. Simultaneously, a new mode appears at 119 cm^{-1} in the I_{-+} channel. ROA of the M3 mode decreases, as M3 activates in the I_{-+} channel leading to a double-peak structure.

To discuss the nature of the double-peak response, we discuss the interaction between the phonon and M3 without considering the chirality of the excitations. In this aspect, the most striking change in M3 is that its evolution with the magnetic field slows down as its energy reaches the energy of the phonon (see also Fig.7.5).

The change in the slope of the M3 for $B \sim 25$ T adheres to the avoided crossing behavior similar to that exhibited by the plasmon and phonon in

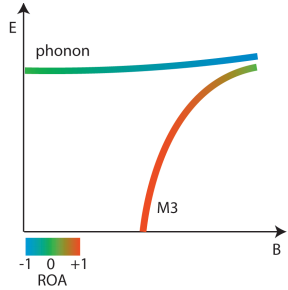

Figure 7.5: illustration of phonon coupling with M3. The color scheme shows the changing chirality of the excitations with the magnetic field. For $B < B_c$, phonon α does not show any chirality. Upon increasing the field further, the mode starts to show helicity dependence as its intensity in the I_{+-} channel starts to drop. When $B \to 15\,\mathrm{T}$ M3 starts to grow, and both its energy and intensity increase with the magnetic field. M3 is only visible in the I_{+-} channel. Remarkably, as the energy of M3 starts approaching the energy of the phonon, the ROA of the M3-phonon mode changes significantly.

GaAs[140] and by the the magnon and the phonon in $FePs_3$ [141]. The avoided crossing behavior indicates coupling between the phonon and the M3 mode. It must be noted that M3 is not a typical magnon, but appears at the lower edge of a multi-particle continuum populated by two-particle excitations (as known from Chapter 5) [93]. M3 has also been designated as the van Hove singularity of the gapped continuum or as a three-magnon bound state [94].

Nevertheless, the interaction between the phonon and the M3 mode can be described using a two-level system. The Hamiltonian of a system that describes the interaction between the phonon and the M3 mode can be written as:

$$\mathcal{H} = \begin{bmatrix} E_{\mathrm{ph}} & M_c \\ M_c^* & E_{\mathrm{M3}} \end{bmatrix}, \tag{7.2}$$

where E_{ph} is the energy of the phonon and E_{M3} is the energy of the M3 mode. The coupling between the phonon and the M3 mode is given by M_c. For non-zero coupling strength ($M_c \neq 0$), the eigenstates of the Hamiltonian take the form:

$$E^{\pm} = \frac{E_{\mathrm{ph}} + E_{\mathrm{M3}}}{2} \pm \frac{1}{2}\sqrt{(E_{\mathrm{ph}} - E_{\mathrm{M3}})^2 + 4|M|^2} \tag{7.3}$$

E^+ corresponds to the upper band and E^- corresponds to the lower band.

From the states, it is clear that when the energy difference $|E_{\mathrm{ph}} - E_{\mathrm{M3}}| \gg$

M_c, the upper and lower bands behave as bare excitations. However, as $E_{\mathrm{ph}} - E_{\mathrm{M3}} \to 0$, the upper and the lower bands have a mixed character and represent a hybridized excitation of the phonon and the M3 mode.

As we know from our measurements, at lower fields the energy of the upper band E^+ corresponds to the phonon (E_{ph}) and the lower band E^- corresponds to the M3 mode (E_{M3}). As the energy of the M3 ($E_{\mathrm{M3}} \propto B$) approaches the energy of the phonon, the two excitations hybridize to form a new quasi-particle. On further increasing the magnetic field, a reversal in ordering is expected between the two states. For $B \gg 30\,\mathrm{T}$, we expect the upper band E^+ to behave as M3 and lower band E^- to behave as the phonon.

Close to the hybridization point, we estimate the coupling strength M_c between the phonon and the M3 mode using the energy splitting between the bands E^+ and E^-. The energy difference between the E^+ and E^- bands corresponds to twice the energy of the coupling strength M_c. Since the minimum observed difference between E^+ and E^- is approximately $2\,\mathrm{cm}^{-1}$, the coupling strength M_c is estimated at around $1\,\mathrm{cm}^{-1}$ (29 GHz), which is approximately 0.9% of its resonance energy.

We finally address the chirality of the observed excitations. Fig.7.5 illustrates the change in the ROA of the excitations with the magnetic field. Both the bands E^+ and E^- exhibit magnetic field dependent chirality. At lower fields E^+ is identified as phonon α with ROA $\to 0$. As the magnetic field increases, E^+ develops negative ROA as the intensity of the phonon in the I_{+-} channel gets washed out as a result of coupling to the continuum. Meanwhile, the lower energy band E^-, which is identified as the M3 mode, starts to develop. The band appears fully chiral at lower fields with a positive ROA. As the energy of M3 approaches phonon α, ROA of the E^- mode drops and the mode becomes achiral. Therefore, on hybridization of phonon α and M3, we observe a double-peak structure from the E^+ and E^- modes in the I_{-+} channel and a single symmetric peak corresponding to the E^- mode in the I_{+-} channel.

7.2 Conclusion & Outlook

In conclusion, we speculate that the chiral phonons emerge as a result of helicity-selective coupling between the phonons and the multi-particle continuum. As seen in Chapter 5, the continuum opens a gap at B_c, and its energy starts to increase with the magnetic field. As the overlap between the energy of the continuum and the phonon grows, the helicity dependent response from the phonons gets stronger. Additionally, for phonon α the Fano

parameter increases faster in the I_{+-} channel, indicating a chirality selective coupling with the continuum.

For the phonon at 116 cm^{-1}, the effect of coupling to the continuum is stronger in the observed field range. This phonon hybridizes with the M3 mode, which is present at the lower edge of the multi-particle continuum. As $B \to 25\,T$, the increased frequency of M3 approaches the phonon frequency. Non-zero coupling between the phonon and M3 leads to avoided level crossing and reduces the slope $\frac{dE}{dB}$ of the M3 mode. Hybridization between the phonon mode and M3 is seen to change the selection rules of the M3 mode as it activates in the I_{-+} channel. Overall, the coupling between the phonons and the multi-particle continuum and the change in chirality of the excitations upon undergoing hybridization is nicely captured by helicity dependent Raman scattering. Understanding the hybridization between the phonon and the M3 mode can benefit from measurements that extend to higher fields. This observation demonstrates the power of helicity dependent Raman scattering in studying 2D materials [138, 142, 143].

We emphasize that the discussion presented in this chapter is still in its preliminary stage and the observed results demand a detailed independent study, performed at high-magnetic fields with smaller field steps. Nonetheless, we have shown here that Raman scattering in the high-field regime of α-$RuCl_3$ provides a direct visualization of the hybridization that occurs between two particles.

Acknowledgements and Contributions

The results presented in this chapter were a byproduct of the study designed to study the helicity dependence of magnetic excitations. The data was collected Mikhail Prosnikov and me. The analysis and the write-up presented here is my solo work. I would like to thank Vladimir Tsurkan and Alois Loidl for providing the sample, and also acknowledge helpful discussions with Paul H. M. van Loosdrecht, Hamoon Hedayat, Vivek Lohani, and Philipp Stein.

8 NON-RECIPROCAL EXCITATIONS

Non-reciprocal effect occurs when the motion of an object in one direction is different from that in the opposite direction. One example when one often encounters non-reciprocity is in p-n junction diodes. A p-n junction diode allows the current to flow only in the forward bias and breaks the directional symmetry. The directional reciprocity (non-reciprocity) is associated with the time-reversal symmetry (asymmetry). Directional reciprocity reverses the direction of propagation, like the time-reversal symmetry $\mathcal{T}$ which takes the system from $t \to -t$ [144].

A spectroscopic example of non-reciprocal phenomena is the Faraday effect. In Faraday rotation, an externally applied magnetic field rotates the polarization of linearly polarized light applied parallel to it by an angle $+\phi$. When the time-reversal operator is applied only to the direction of light propagation, polarization gains an additional angle, making the rotation angle $+2\phi$. Therefore, reversing only the direction of light propagation breaks the time-reversal symmetry of the system and its reciprocity. However, if time-reversal is applied on the entire system, including the magnetic field, then the polarization is rotated back to its initial polarization and the system remains time-reversal invariant and reciprocal. Time-reversal symmetry of the system has to be broken to observe non-reciprocity [144, 145].

Non-reciprocity occurs in materials with strong spin-orbit coupling and low crystal symmetry. Thus far, non-reciprocity has been encountered in multiferroics in the vicinity of electromagnons [146–148]. Another type of non-reciprocity is observed in chiral magnetic systems, where the light is applied parallel to the direction of the chiral axis and the magnetic field. Reversing the

direction of light propagation can result in different absorption and emission strengths [149–152]. This effect is also known as magneto-chiral dichroism.

In this chapter, we explore the possibility of using magneto-Raman scattering as a probe of non-reciprocal excitations. Reciprocity of the excitations is investigated by using its scattering intensity as a measure. Raman intensity of excitations is compared between two experimental configurations that are related to one another by time-reversal symmetry. If in an initial setting, the Raman intensity in cross-circular polarization channel is given as:

$$pI_{+-} = |e_s^{\sigma^-} \cdot R(B) \cdot e_i^{\sigma^+}|^2 \tag{8.1}$$

where in pI_{+-} term, I_{+-} denotes that the incident/scattered light impinges spin angular momentum σ^+/σ^- on the crystallographic $\hat{z}$ axis and p denotes that the external magnetic field is oriented parallel to the crystallographic $+\mathbf{a}$ axis. Under time-reversal symmetry, $\sigma^+ \rightarrow \sigma^-$ and $B \rightarrow -B$. That is, time-reversal pair is obtained by reversing the direction of the magnetic field and the polarizations of incident and scattered light. Therefore, the time-reversal symmetric pair of the initial experimental setting corresponds to:

$$nI_{-+} = |e_s^{\sigma^+} \cdot R(-B) \cdot e_i^{\sigma^-}|^2 \tag{8.2}$$

where in nI_{-+} term, I_{-+} denotes that the incident/scattered light impinges spin angular momentum σ^-/σ^+ on the crystallographic $\hat{z}$ axis and n denotes that the external magnetic field is oriented parallel to the crystallographic $-\mathbf{a}$ axis. An excitation for which $pI_{+-} \neq nI_{-+}$ is identified as non-reciprocal.

We observe that some excitations show non-reciprocity in the high-field regime. One such excitation is the 116 cm^{-1} phonon at 30 T, which at the given field is formed from hybridization of the phonon with the M3 mode (as seen in Chapter 7). Apart from it, the dominant spin-flip excitation M1 exhibits non-reciprocity.

8.1 Experimental details

To check the time-reversal symmetry, we utilize the same setup as described in the previous two chapters. The measurements are performed as a function of magnetic field at a base temperature of 1.7 K with 10 µW incident power of a 532 nm laser. The only difference is that instead of two sets of measurements from the two helicity channels, i.e, I_{+-} and I_{-+}, we now have four sets of measurements, two each from the direction of magnetic field set

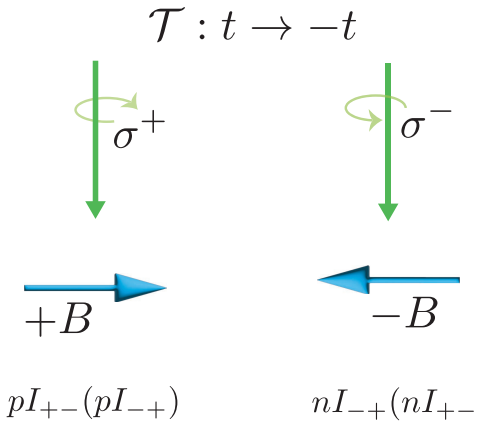

Figure 8.1: Time-reversal symmetric pair of the experimental configuration.

along the $+\mathbf{a}$ and the $-\mathbf{a}$ direction. Measurements with field along $+\mathbf{a}$ axis are denoted with the letter p and the measurements with field along $-\mathbf{a}$ axis are denoted with the letter n. This results in four experimental channels defined as $pI_{+-}, pI_{-+}, nI_{+-}$ and nI_{-+}. As previously discussed, pI_{+-} and nI_{-+} are time-reversal symmetric channels. Similarly, channels pI_{-+} and nI_{+-} are time-reversal symmetric (see Fig.8.1).

8.2 Experimental results

The measurements from all the four channels are plotted for different magnetic fields in the appendix. As expected, most of the excitations show identical scattering in the time-reversal symmetric channels. Only exceptions being the phonon α at 116 cm^{-1} and the M1 mode. In the following, these features are discussed in detail.

8.2.1 Phonon α (116 cm^{-1})

As we know from the previous chapter, as $B \to 30$ T, the phonon at 116 cm^{-1} acts a complex excitation formed by hybridization of the phonon and the M3 mode.

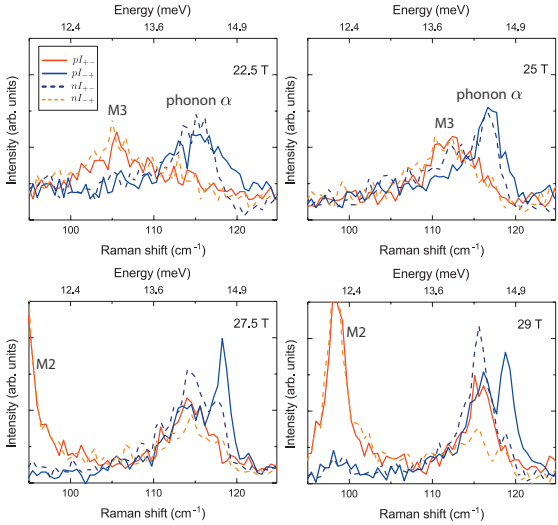

Figure 8.2: magnon-phonon hybridization from 20 T to 30 T.

Fig.8.3 compares the spectrum from channels pI_{+-} , nI_{-+} , pI_{-+} , and nI_{+-} with each other. It is clear, that the spectral response from all the four polarization channels is different. The double peak feature only appears in p-channels, but with a non-zero ROA. Similarly, in nI_{+-} and nI_{-+} channels, the phonon shows unequal scattering intensity, with nI_{+-} channel showing a symmetric phonon with a sharp edge towards its higher energy and nI_{-+} showing suppressed intensity.

To understand the role of hybridization between the phonon and the M3 mode in switching on the non-reciprocal response, we zoom into a field range from 20 T to 30 T. Fig.8.2 shows M3 approaching the vicinity of phonon α. Up to 25 T, both the features – M3 and phonon α are reciprocal. Nonetheless, at 27.5 T as M3 and phonon α approach hybridization, the higher energy peak of the double-peak feature shows non-reciprocity, and non-zero ROA which increases with the magnetic field.

Non-zero ROA indicates broken inversion symmetry, i.e, chirality. Meanwhile, difference in pI_{+-} and nI_{-+} (or nI_{+-} and pI_{-+}) indicates broken time-reversal symmetry. Both these features combined, highlight the complex nature of the phonon-multi-particle (M3) hybridized excitations.

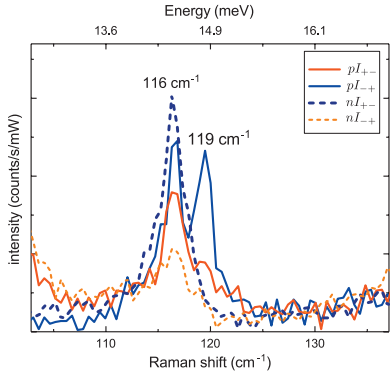

Figure 8.3: Spectrum in the energy window of Phonon A at 30 T, measured in the four possible experimental channels. Each of the four experimental channels show a unique spectrum and highlights the complex nature of the phonon-magnon hybridized mode.

8.2.2 M1

The dominant magnetic excitation of the spectrum shows difference in the scattering intensity between the two time-reversal symmetric pI_{+-} and nI_{-+} (nI_{+-} and pI_{-+}) channels. Fig.8.4 shows the difference spectra of the M1 mode measured between the pI_{+-} and nI_{-+} channel. The difference is plotted for an increasing magnetic field. Intensity of the difference spectra increases with the applied field. The M1 mode appears time-reversal symmetric for $B < 10\,\mathrm{T}$. As the field increases, the differential intensity of the M1 mode also increases. Above 15 T, differential intensity of M1 seems to plateau. In Chapter 6, 15 T has been identified as the onset of the high-field regime. It is also pointed out that the ROA of M1 remains small in the high-field regime. This indicates that, for $B > 15\,\mathrm{T}$, M1 exhibits symmetry under inversion, but shows non-reciprocity.

8.3 Discussions and conclusions

In this chapter, we studied the effect of the direction of the magnetic field on the Raman response of α-$RuCl_3$. Non-reciprocal excitations are observed in the high field regime. The M1 mode and the 116 cm^{-1} phonon (phonon

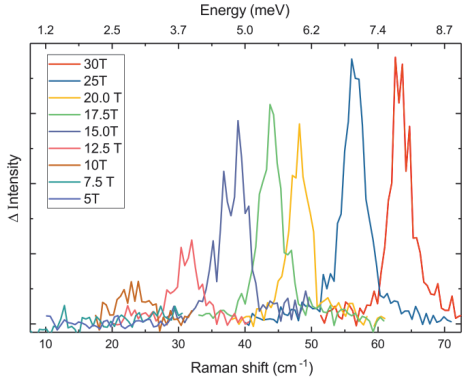

Figure 8.4: Differential intensity plot of M1 measured between the pI_{+-} and nI_{-+} channels, indicating its non-reciprocal response. Zero differential intensity below $B < 10\,\mathrm{T}$, indicates its reciprocal nature. The effect is quantified in Fig.8.5

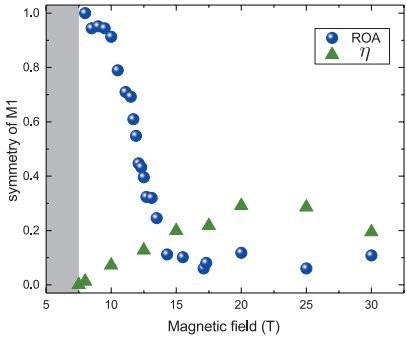

Figure 8.5: Effect of magnetic field on the inversion and time-reversal symmetry of the M1 mode. The blue spheres show Raman optical activity which measures the inversion symmetry and the green triangles show non-reciprocity of the M1 mode which results from the difference in intensity between the pI_{+-} and the nI_{-+}.

α) show non-reciprocity. Typical Raman-active excitations are not expected to show non-reciprocal behavior, as the scattering tensor only contains real elements as a result of time-reversal symmetry. As previously mentioned, non-reciprocity requires broken time-reversal symmetry of the system. In the high-field limit, magnetic ordering of the system can break the time-reversal symmetry, and allow for non-reciprocal excitations.

M1 mode has been previously identified as a $\Delta S = \pm 1$ excitation of the field polarized limit. The onset of this mode at B_c was initially taken as an evidence for the onset of field polarization [93]. As the magnetic field increases, the system reaches closer to field polarization. As this happens, intensity of the M1 mode also strengthens. Using ROA and directional dichroism, we extract information about the inversion symmetry and non-reciprocity (see Fig.8.5). Degree of non-reciprocity plotted in Fig.8.5 is quantified using the intensity differential η defined as:

$$\eta = \frac{pI_{+-} - nI_{-+}}{pI_{+-} + nI_{-+}}.$$

It is observed that the symmetry of the M1 mode changes drastically with the magnetic field. In the intermediate field regime, i.e close to B_c , the M1 mode is fully chiral and reciprocal. This changes on increasing the magnetic field, as in the high-field regime, the mode is achiral but non-reciprocal. Thus, we observe a complete reversal of symmetry from the intermediate-field regime to the high-field regime.

High-field regime and possible magnetic ordering in the system is also indicated by the non-reciprocal character of the phonon-M3 hybrid mode at 116 cm^{-1}. The excitation is not just non-reciprocal, but also shows non-zero Raman Optical Activity, indicating its chiral nature. In future, knowledge of these underlying symmetries can significantly aid in understanding of the hybridization mechanism between the phonon and the multi-particle excitation.

In the given experimental setting, non-reciprocal excitations are only allowed if the crystal symmetry does not render the direction of the applied magnetic field and its reversed direction to be equivalent. In this experiment, as the field is applied along the crystallographic **a**-axis, to observe non-reciprocity, the crystal symmetry must not render the $+\mathbf{a}$ and $-\mathbf{a}$ direction equivalent. However, α-$RuCl_3$ has a C_2 axis along the crystallographic **b**-direction [22, 44], which renders the $+\mathbf{a}$ and $-\mathbf{a}$ direction to be equivalent. This would mean that non-reciprocal excitations are only allowed if the 2-fold rotation symmetry is broken. Therefore, our observation of non-reciprocal excitations hints at a possible structural phase transition to the space group C_m, with only a mirror plane in the **ac** plane in the high-field regime of the material.

In future, this finding can be verified by a detailed field dependent structural study of the material.

All in all, the presence of non-reciprocal excitations in the high-field regime of α-$RuCl_3$ indicates a regime distinct from the intermediate field regime. Furthermore, they indicate a lowering of the crystallographic symmetry and a possible structural phase transition. Both these observations substantiate our claim of an intermediate field regime distinct from the high field regime ($B > 15\,\mathrm{T}$) in α-$RuCl_3$. Non-reciprocal excitations highlight the rich physics in the high field regime of α-$RuCl_3$. The next chapter reviews our experimental observations thus far and concludes the thesis by providing important insights on the field-induced phase of α-$RuCl_3$.

Acknowledgements and Contributions

I designed the study based on preliminary data collected at HFML in 2018 (shown in Chapter 5) with inputs from Paul H. M. van Loosdrecht. The preliminary data was collected with Jonathan Buhot and the data presented here was collected in December 2020 with Mikhail Prosnikov. I thank Vladimir Tsurkan and Alois Loidl for providing the sample. The chapter is written by me. I thank Philipp Stein for contributing to the preliminary analysis. I thank Paul H. M. van Loosdrecht, Hamoon Hedayat, Thomas Koethe, and Philipp Stein for helpful discussions.

9 CONCLUSIONS

The story of α-$RuCl_3$ in condensed matter physics is closely linked to the search for Kitaev spin liquids. Due to a unique combination of Kitaev, Heisenberg, and off-diagonal exchange interactions exhibited by this material, it has been the subject of numerous theoretical and experimental studies. Following these investigations, numerous controversies have arisen regarding the properties of α-$RuCl_3$ — some related to the reliability of experimental techniques [32, 36, 110–112, 114, 116, 153] and others focused on the theoretical interpretations of experimental observations [31, 34, 77, 105, 106, 154, 155]. At the center of this debate lies the quest to identify the signatures of a stable Quantum Spin Liquid phase. This very objective is the heart of this thesis.

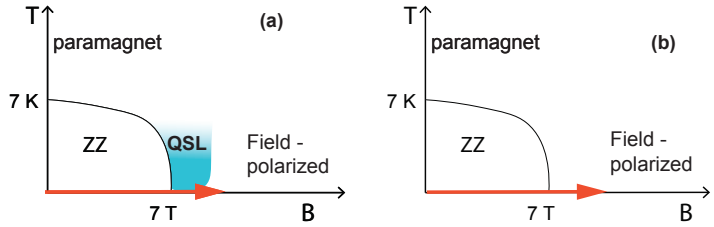

Figure 9.1: Two scenarios have been proposed for the intermediate field regime of α-$RuCl_3$: (a) With a stable QSL phase. (b) Without a QSL phase.

Experimental observations have established that α-$RuCl_3$ undergoes a field-induced phase transition in which an external magnetic field suppresses the zigzag magnetic order. However, it remains unclear whether a Quantum Spin Liquid (QSL) phase emerges as an intermediate phase between the zigzag magnetic phase and a field-polarized phase. Over the years, two scenarios

have been proposed for the field-induced phase of α-$RuCl_3$: (a) There exists a distinct QSL phase between the zigzag phase and a field-polarized phase. (b) There is no distinct QSL phase, and the system asymptotically approaches field polarization.

In this thesis, we embarked on addressing this critical question using Raman scattering. Initially, we confirmed that Raman scattering could detect the rich spectroscopic features of the field-induced phase previously observed through electron spin resonance and THz-absorption. By extending our scattering measurements to very high magnetic fields, we were able to characterize the nature of the observed excitations. Through exact-diagonalization calculations performed for a field-polarized ground state, we determined that the dominant spectral feature at high fields, referred to as M1, represents a $|\Delta S| = 1$ spin-flip excitation. Identifying the nature of M1 yielded two primary advantages: (i) It allowed us to characterize the nature of other observed excitations. (ii) It provided insights into the nature of the field-induced phase. The fact that M1 emerged at $B_c \sim 7.5\,\mathrm{T}$ helped us identify the field-induced phase as a partially polarized quantum disordered state (QDS), that is smoothly connected to the fully field-polarized limit.

If we had stopped at this conclusion, our understanding of the nature of the field-induced phase would have been significantly limited. Our next experiment, however, was poised to challenge this preliminary conclusion. For the next step, we aimed to probe the symmetries of the unconventional excitations which emerge in the field-induced phase. For our second magnet time at the HFML, the agenda was to tweak the experimental setting in order to gain insights into the symmetry of the observed magnetic excitations. We had hypothesized that by controlling two key experimental parameters, namely, the (i) helicity of light and (ii) the direction of the magnetic field, we could potentially acquire information about the chirality and non-reciprocity of these excitations. Both of these aspects offered valuable insights into the symmetry of the magnetic excitations and their underlying ground state in various field regimes.

Through helicity-dependent measurements, we discovered the chiral nature of the excitations. We observed that the magnetic field influences the degree of chirality, known as Raman Optical Activity (ROA), of these excitations. The most remarkable observation was the behavior of the dominant excitation, M1, which exhibited a plateau with ROA = 1 in the magnetic field range from 7.5 T to 10.5 T. This finding was particularly surprising since helicity-dependent scattering is not typically expected in the conventional paramagnetic phase of a monoclinic material. Interestingly, the ROA plateau of M1 also coincides with the magnetic field boundaries where other studies

have reported the presence of a Quantum Spin Liquid phase [115].

Another intriguing observation pertains to the non-reciprocal behavior of the M1 mode. We noticed that the degree of non-reciprocity for M1 exhibits a complementary trend to its ROA, indicating a complete reversal in the symmetry of M1. However, it's important to note that we did not observe any signature of a distinct intermediate field regime based on the degree of non-reciprocity of M1. Consequently, it appeared that our successive studies had arrived at diametrically opposite conclusions.

Now we must address the elephant in the room: 'Is there a Quantum Spin Liquid phase in the intermediate field regime of α-$RuCl_3$?'. Before we can answer this question, we must first be convinced that there is indeed a distinct intermediate field regime, which we had denied in the first part of our work. The reasoning for such a claim was based on the fact that the M1 mode, identified as the spin-flip excitation of the field-polarized limit, is smoothly connected to B_c. However, little did we know that if we had performed the exact same experiment with the reversed helicity of light, the M1 mode would have only appeared after 10.5 T (see Appendix III). This is exactly what the second experiment demonstrated and the subsequent analysis led us to conclude that the existence of a distinct intermediate field regime is undeniable. This brings us to a direct confrontation with the question as to weather this regime corresponds to a different phase. There is no easy answer to this question. We have already pointed out that there is no single, easy, definitive check to identify the presence of a Quantum Spin Liquid phase or lack thereof. One definitive methodology to confirm the presence of a QSL phase in α-$RuCl_3$ is to demonstrate that experimental observations align with the theoretical predictions for a pure Kitaev Spin Liquid. However, due to the intricate nature of Kitaev systems, other factors may yield similar results, introducing complexities in interpretation*. Due to the lack of a direct theoretical evidence, the appearance of a second phase transition observed at $B > B_c$ is interpreted as phase transition out of the Quantum Spin Liquid phase [115]. We note here, that a phase transition out of the QSL phase will be a topological phase transition and may or may not be associated with

*Example: (i) The broad continuum observed in neutron [29] and Raman scattering [30] is associated with fractionalized excitations of the Kitaev model [34, 35], although, it is has been argued that this continuum comes from magnons that decay rapidly as a consequence of frustrated interactions [105, 154]

(ii) The emergence of half-quantized thermal Hall conductivity in α-RuCl3 in the presence of in-plane magnetic fields has been considered strong evidence for the presence of the Kitaev spin liquid [111]. Nevertheless, this interpretation has faced challenges, as calculations have demonstrated that topological magnons with finite Chern numbers can produce the same results observed in quantum Hall experiments [133].

symmetry breaking. In this light, we can take two possible routes to establish the presence of a Quantum Spin Liquid phase in the intermediate field regime:

1. We can compare our experimental observations with the theoretical predictions for a pure Kitaev Spin Liquid.
2. We can identify the signatures of a topological phase transition out of the intermediate field regime.

Unfortunately, we currently face roadblocks on both of these routes. Firstly, theoretical work addressing the chirality of the emergent excitations in the Kitaev spin liquid phase is lacking. Secondly, it is premature at this stage to associate the change in the chirality of the excitations with a topological phase transition. We note that an effort is underway to probe the topological order using circular dichroism [156–158]. Interestingly, recent work has proposed Raman circular dichroism as a means to probe magnon topology in two-dimensional quantum magnets [159]. With these advancements, we are hopeful that in the near future, tabletop optical setups based on circular dichroism will enable the probing of topological order, greatly facilitating the detection of Quantum Spin Liquid phases. Thus, we find that our results regarding the existence of chiral excitations in the intermediate field regime of α-$RuCl_3$ are at the forefront of our current knowledge. This limitation prevents us from definitively classifying the intermediate field regime as a distinct Quantum Spin Liquid phase. We are optimistic that our findings will offer valuable insights into the nature of an unconventional ground state that exists in the narrow intermediate field regime of α-$RuCl_3$.

APPENDIX I

A. Sample Quality

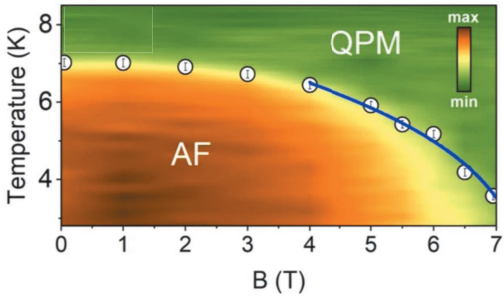

Figure 9.1: (a) Phase diagram of α-$RuCl_3$ in-plane magnetic field and temperature constructed from the rotation θ_{MLD} (color code from 0 to 70 mdeg) obtained by Magnetic Linear Dichroism measurements [48]. The crystal shows a single phase transition at 7 K from AF: Antiferromagnetic to QPM: paramagnetic phase. Reprinted from Ref.[48] under a Creative Commons Attribution 4.0 International (CC BY 4.0) license. ©2022 Wagner et al.

High-quality single crystals of α-$RuCl_3$, are sourced from the group of Alois Loidl and Vladimir Tsurkan from Augsburg. These samples are grown using the vacuum sublimation method [26]. Fig.9.1 shows the phase diagram of α-$RuCl_3$ from a sample sourced from the same batch as the samples used in our study. The phase diagram is measured by Wagner et al [48] using Magnetic Linear dichroism. The sample shows a single phase transition at 7 K, indicating its high quality [23].

APPENDIX II

A. Raman scattering setup at the HFML

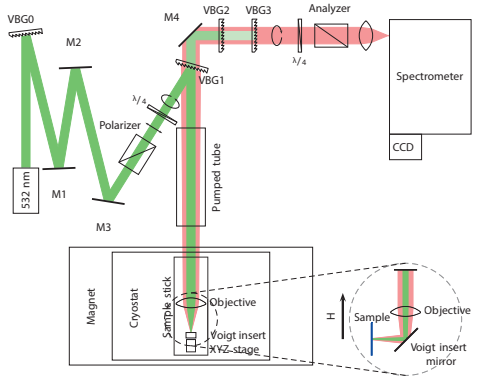

Figure 9.1: Sketch of the magneto-optic setup used in the experiment when using cross-circular polarization geometry. VBG: Volume Bragg Grating, M: Mirror. (Sketch by Mikhail Prosnikov*)

B. Contribution from Faraday rotation

To ensure that the observed variations in excitation intensity with the magnetic field are not attributed to experimental setup factors, we model the magnetic field's impact on the intensity of different polarizations of scattered light. Even when the probe is circularly polarized, scattering can alter the incident light's polarization. When linearly polarized light passes through the Faraday cell, it may experience rotation which can affect its detected intensity. In our micro-Raman setup, the optical objective used for focusing light on the sample can act as a Faraday cell in the presence of an external magnetic field.

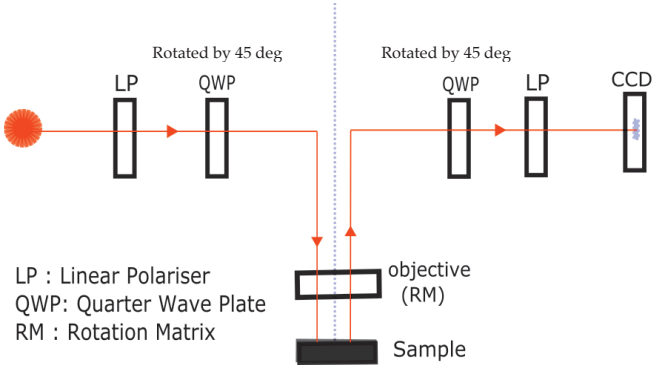

Figure 9.2: Raman setup with polarization changing optical elements.

The effect of Faraday rotation on the scattered light can be found by operating on the scattered light vector with a rotation matrix (RM) described in Eq.9.1

$$\mathrm{RM} = \begin{pmatrix} \cos\theta & -\sin\theta \\ \sin\theta & \cos\theta \end{pmatrix} \tag{9.1}$$

Rotation angle θ is field dependent and can be calculated using Eq.9.2:

$$\theta = \mathcal{V} B \cos\phi, \tag{9.2}$$

where $\mathcal{V}$ is a Verdet coefficient, B is the magnetic flux density in the direction of the travel and ϕ is the angle between the magnetic field B and the light propagation vector $\vec{k}$. The Verdet constant for the objective used is 1.55°/ T.

However, other optical elements in the detection scheme can modify the electric field of the scattered light. The effect of these elements can be accounted by operating on the rotated light with the Jones matrices of the polarization

inserts in the beam path of the scattered light. The optical elements considered are – a quarter wave plater (QWP), and a linear polarizer (LP) as shown in Fig.9.2.

Jones matrix for a quarter wave plate rotated by 45° is given as:

$$\text{QWP} = e^{i\frac{\pi}{4}} \begin{pmatrix} 1+i & 1-i \\ 1-1 & 1+i \end{pmatrix}$$

the Jones matrix for a vertical linear polarizer is given as:

$$\text{LP} = \begin{pmatrix} 1 & 0 \\ 0 & 0 \end{pmatrix}$$

Therefore, the detected electric field is described using Eq.9.3:

$$E_d = \text{LP} \cdot \text{QWP} \cdot \text{RM} \cdot E_s \tag{9.3}$$

where E_s is the polarization of the scattered light. The detected Raman intensity is related to the electric field by the relation $I_d = |E_d|^2$. The effect of the magnetic field on the detected light is simulated using Eq.9.3. Fig.9.3 plots the detected intensity I_d as a function of the magnetic field B for the linear, circular and elliptical light polarization. We observe the following:

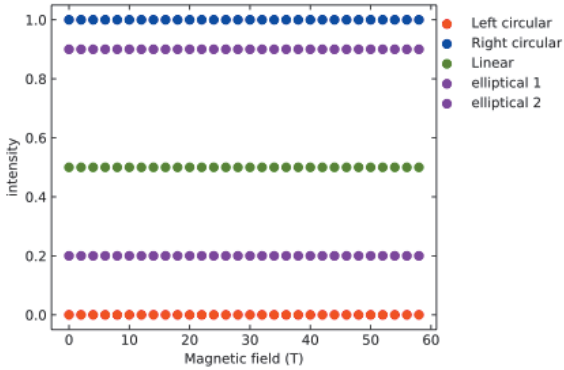

Figure 9.3: Detection efficiency as a function of magnetic field for different polarizations of the scattered light.

1. Circular light of one handedness (Left Circularly Polarized σ^+) is detected with maximum sensitivity while of opposite handedness (Right Circularly Polarized) is completely blocked. The selection of helicity is made by setting the fast-axis of the QWP to either $+45°$or $-45°$ of the following linear polarization axis.
2. The detection sensitivity to other polarizations remains in between these two values.
3. linearly polarized light is detected by 50% efficiency.
4. The detection sensitivity for elliptical polarized light lies somewhere in between 0 and 1 depending on the phase and amplitude.
5. Irrespective of the polarization, the scattered light does not show any dependence on the magnetic field.

APPENDIX III

A. Helicity resolved Scattering

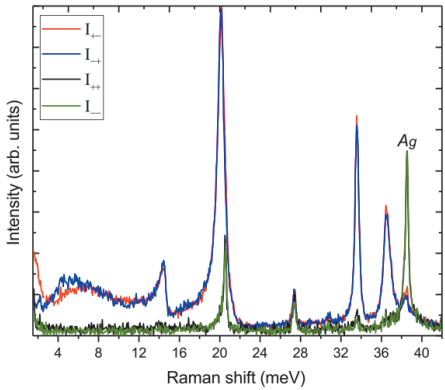

Figure 9.1: Polarization dependence at 7.5 T. Spectra is measured with a 532 nm laser at 1.7 K.

Figure 9.1 is a reference scan taken at 7.5 T in the IFR. It shows that the magnetic excitations and the multi-particle continuum are absent in the (co-circular) I_{++} and I_{--} geometries. The co-circular polarization geometry is characterised by Raman active A_g phonons (green and black lines).

Helicity dependent Raman scattering resolves the development of the magnetic excitations in two separate polarization channels - I_{+-} and I_{-+}. In the I_{+-} channel, M1 is visible immediately above the zigzag phase. In the I_{-+} channel, M1 only appears above 10.5~T. This shows that M1 is fully chiral in the field regime of 7.5~T to 10.5~T. M2 can be seen to interchange between the two channels at 15~T (cf. Fig.9.2).

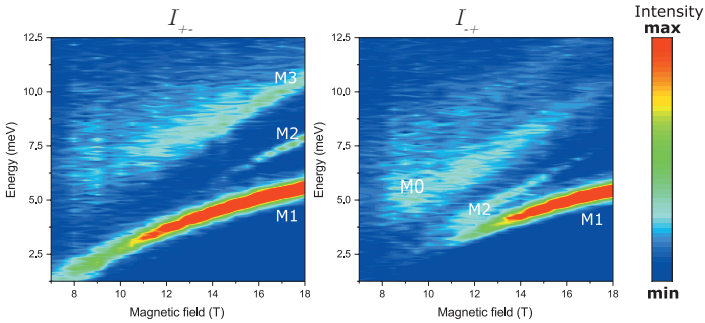

Figure 9.2: Color plot shows the change in intensity and energy of excitations with the field, as observed in the I_{+-} and the I_{-+} channels. Both plots are constructed using the same color scale to compare the intensities.

Figure 9.3 provides an overview of our Raman spectra measured in the different field regimes. No significant changes of ROA of the magnetic excitations are observed above 15 T.

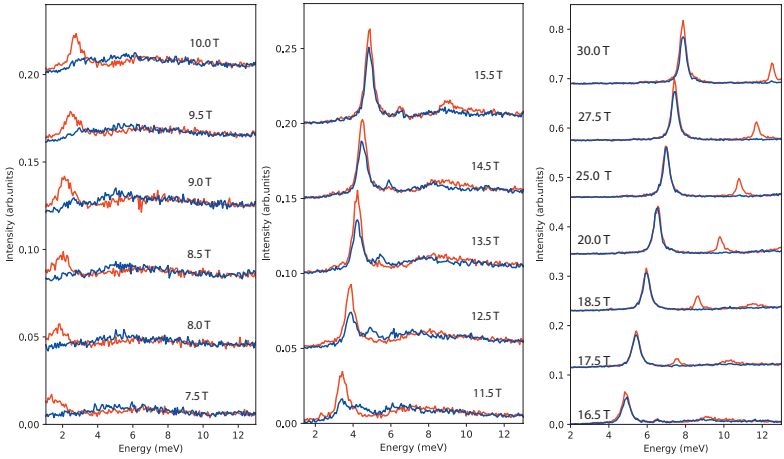

Figure 9.3: Helicity dependent scattering from the different field regimes

B. Procedure to Extract ROA

B.1. ROA of M1

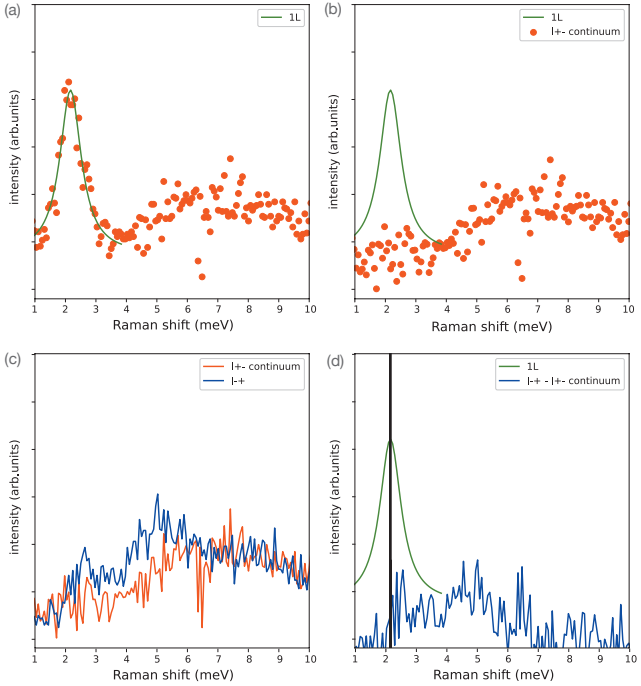

Figure 9.4: (a-d) Steps to extract the ROA of M1. (a) The dominant peak M1 of the spectrum measured in the I_{+-} channel (red dots) is fitted with a Lorentzian (green curve). (b) The Lorentzian fit (green curve) obtained from (a) is subtracted from the I_{+-} spectrum to isolate the background continuum (red dots). The I_{-+} spectrum is compared with the background continuum extracted in (b) from the I_{+-} spectrum.(d) The black line indicates the energy at which the M1 is expected to appear in the I_{-+} channel.

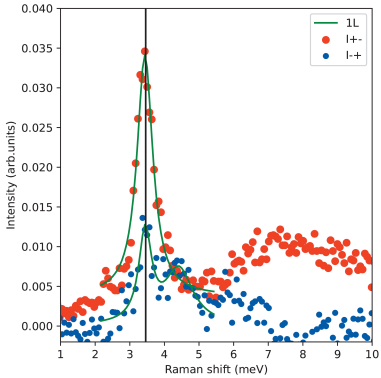

Figure 9.5: ROA of M1 in the transition regime.

To find the ROA, areas obtained from fitting a Lorentzian peak are compared. The following procedure has been followed to subtract the contribution from the continuum that is present beneath the mode.

1. M1 as observed in the I_{+-} channel is fitted with a Lorentzian with a constant background (Fig.9.4(a)).
2. The obtained fit is subtracted from the I_{+-} spectrum to obtain the shape of the continuum (Fig.9.4(b)).
3. The continuum is then compared to the I_{-+} spectrum, to reveal a peak if any in I_{-+} channel (Fig.9.4(c-d)). The obtained curve is then fitted by a double Lorentzian to obtain the area of peak corresponding to M1. For 8 T no peak is observed at the same energy as M1 (Fig.9.4(d)) resulting in ROA = 1. Meanwhile M1 is observed in I_{-+} channel at 11.5 T (Fig.9.5).
4. The areas of M1 obtained from fitting in the two channels, I_{+-} and I_{-+}, are used to calculate ROA as follows: $ROA = \frac{I_{+-} - I_{-+}}{I_{+-} + I_{-+}}$

B.2. Intensity of M0

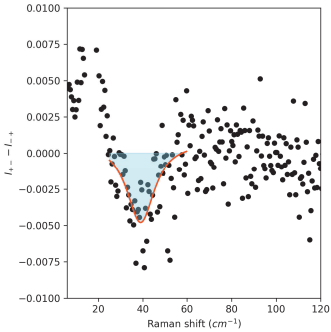

(a) M0 in IFR, sample measurement from 8 T

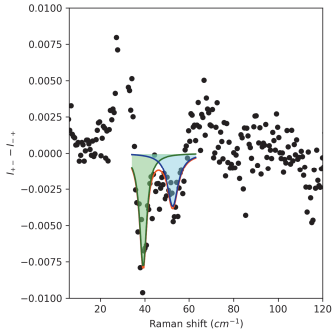

(b) M0 in TR, sample measurement at 12.5 T.

Figure 9.6: For $B \geq 10.5\,\mathrm{T}$ double Lorentzian is needed to fit the emerging M_2 with $M0$. The green area represents area under M_2, and the blue area represents area under M0.

In the ROA spectra, there appears a broad energy regime close to 5 meV which is consistently stronger in the I_{-+} channel. In this section we will estimate the energy and intensity of this mode. We will first try to evaluate the shape of this feature at 8 T, in the IFR. On taking the difference spectra between $I_{+-} - I_{-+}$ a broad feature is revealed around 5 meV. This broad feature is fitted with a Lorentzian (see Fig.9.5(a)). Fitting by a Lorentzian produces a decent fit with $\chi_r^2 = 1.233$. Peak energy using this fitting is found to be at (4.9 ± 0.1) meV. On increasing the field to 10.5 T, a new mode M2 starts to grow exclusively in the I_{-+} channel. Thereby, at $B = 10.5\,\mathrm{T}$ and above, the spectra in vicinity of 5 meV cannot be fitted with a single Lorentzian and instead needs two Lorentzians to fit (see Fig.9.5(b)). Out of the two Lorentzians, the defined bounds sets the lower energy peak at M2 and the higher energy peak as M0. A test fit to the data, at 12.5 T yields $\chi_r^2 = 0.883$.

C. Power-temperature relation

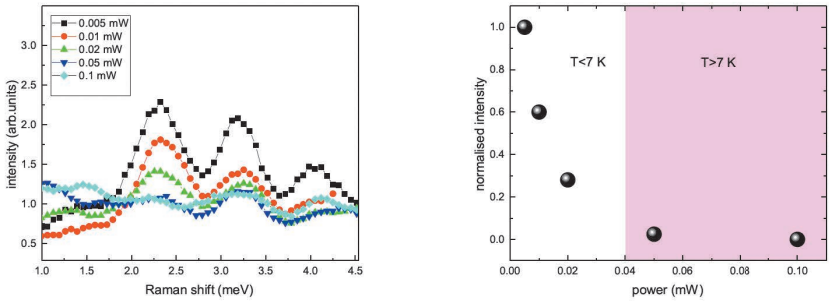

(a) (b)

Figure 9.7: (a) Power dependent measurements qualitative. (b) Power dependent measurements quantitative

At a base temperature of 1.7 K, at $B = 0$, two AFM magnons are observed at 2.3 and 3.2~meV. Magnons reduce in intensity with no noticeable broadening. On increasing the power of the incident beam, the magnons melt into the multiparticle continuum (cf. Fig.9.7(a)). The decrease in scattering intensity results from the heating induced by the probe beam. Above 40 µW the magnons are no longer resolved, this indicates a local temperature of ∼7 K (cf. Fig.9.7(b)). For larger powers of the incident beam, the temperature is estimated using the ratio of anti-Stokes to Stokes intensity of the M1 mode at 30 T, which yields 25 K at 25 µW and 41 K at1000 µW. Based on these results, we estimate a temperature of ∼3 K at 10 µW and ∼13 K at 100 µW.

D. ROA estimates in different field regimes

The Raman intensity is given by $I = |e_s^\dagger \cdot \mathcal{R} \cdot e_i|^2$ where $\mathcal{R}$ is the Raman tensor and $e_i(e_s)$ are the vectors of the incident(scattered) light. ROA is calculated as:

$$ROA = \frac{I_{+-} - I_{-+}}{I_{+-} + I_{-+}}$$

for cross- circular polarization channels, similarly, it can be calculated for co-circular channel by replacing $I_{+-} \rightarrow I_{++}$ and $I_{-+} \rightarrow I_{--}$

Polarization vectors for the co- and cross-cirlcular polarization channels are given as:

$$I_{+-} : e_s = \tfrac{1}{\sqrt{2}}\begin{pmatrix}1\\-i\\0\end{pmatrix} \text{ and } e_i = \tfrac{1}{\sqrt{2}}\begin{pmatrix}1\\i\\0\end{pmatrix} \quad I_{-+} : e_s = \tfrac{1}{\sqrt{2}}\begin{pmatrix}1\\i\\0\end{pmatrix} \text{ and } e = \tfrac{1}{\sqrt{2}}\begin{pmatrix}1\\-i\\0\end{pmatrix}$$

$$I_{++} : e_s = \tfrac{1}{\sqrt{2}}\begin{pmatrix}1\\i\\0\end{pmatrix} \text{ and } e_i = \tfrac{1}{\sqrt{2}}\begin{pmatrix}1\\i\\0\end{pmatrix} \quad I_{--} : e_s = \tfrac{1}{\sqrt{2}}\begin{pmatrix}1\\-i\\0\end{pmatrix} \text{ and } e_i = \tfrac{1}{\sqrt{2}}\begin{pmatrix}1\\-i\\0\end{pmatrix}$$

ROA in co-and cross-cirlcular polarization channels can be calculated once the Raman-tensor $\mathcal{R}$ is known.

For crystallographic space group - C2/m, the magnetic point groups of the antiferromagnetic, paramagnetic, and ferromagnetic field-polarized phases are determined and their ROA is estimated.

D.1. ROA in paramagnetic regime ROA of the excitations in the paramagnetic regime of the crystallographic space groups - C2/m.

The Raman tensors for C2/m space group in the linear basis are given as:

$$R(A_g) = \begin{pmatrix}a & 0 & d\\0 & b & 0\\d & 0 & c\end{pmatrix} \quad R(B_g) = \begin{pmatrix}0 & a & 0\\a & 0 & e\\0 & e & 0\end{pmatrix} \tag{9.1}$$

In cross-circular polarization geometry, this yields an intensity of $I_{+-}(B_g) = I_{-+}(B_g) = a^2$ for $C2/m$. Therefore $\mathrm{ROA}(B_g) = 0$. Similarly, it can be shown that $\mathrm{ROA}(A_g) = 0$ in co- and cross-circular geometry. Thus ROA = 0 is expected in a simple paramagnetic phase. The observation of pronounced ROA in the IFR, just above B_c, corroborates its particular character that is compatible with a quantum spin liquid.

D.2. ROA in zigzag phase According to Chapter 4, magnetic point group is identified to be colorless $2/m$. Therefore, the Raman tensors are described by Eq.9.1. Similar to the paramagnetic grey group, no Raman optical activity is expected.

D.3. ROA in field polarized phase For a monoclinic $C2/m$ crystal, the field polarized magnetic field applied along the crystallographic a- axis should have a magnetic group $2'/m'$. However, as non-reciprocity is observed in the high field phase (see Chapter 8), the 2-fold rotation axis might be broken. In that case, the magnetic point group will be m'. Fortunately, following Cracknell et al both $2'/m'$ and m' have an identical Raman tensor with a single irreducibe represntation. The Raman tensor is given as:

$$DA(DA_g) = \begin{pmatrix} A & B & iC \\ D & E & iF \\ iG & iH & I \end{pmatrix}$$

For this tensor, the quantization is set along the z-axis. Given that in our experimental setup, the magnetic field is along the y axis, the Raman tensor has to be transformed to:

$$DA(DA_g) = \begin{pmatrix} A & iC & B \\ iG & E & iH \\ D & iF & I \end{pmatrix}$$

In cross-circular polarization geometry, this yields an intensity of $I_{+-} = A - \zeta$ and $I_{-+} = A + \zeta$; where $\zeta = C + G + E$

Therefore, non-zero ROA, and chiral excitatations can be observed in the cross-circular polarization geometry.

Similarly, ROA can be calculate for the co-polarization channel as $I_{++} = r - k$ and $I_{--} = r + k$; where $r = A + E$, $k = C - G$

APPENDIX IV

A. Non-reciprocity in Raman spectrum

In the high-field phase, the dominant excitation M1 and the hybridized mode of phonon α and M3 show non-reciprocity.

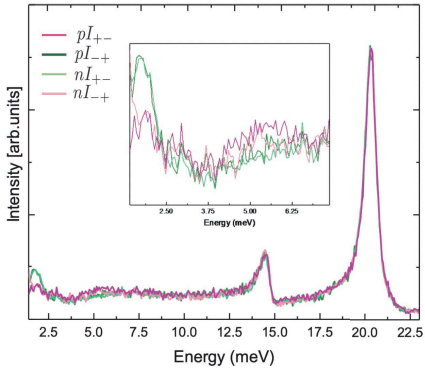

Figure 9.1: Raman spectra measured with all four polarization channels at 5 T in the zigzag phase. The subset zooms in to the low energy region where the antiferromagnetic magnons are found.

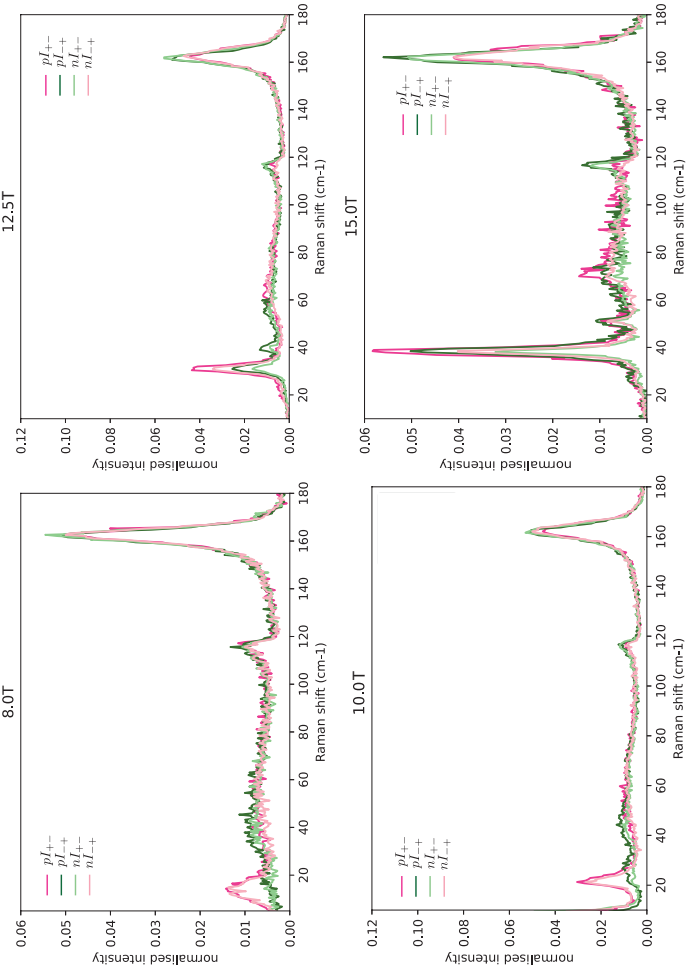

Figure 9.2: plots from all the four channels.

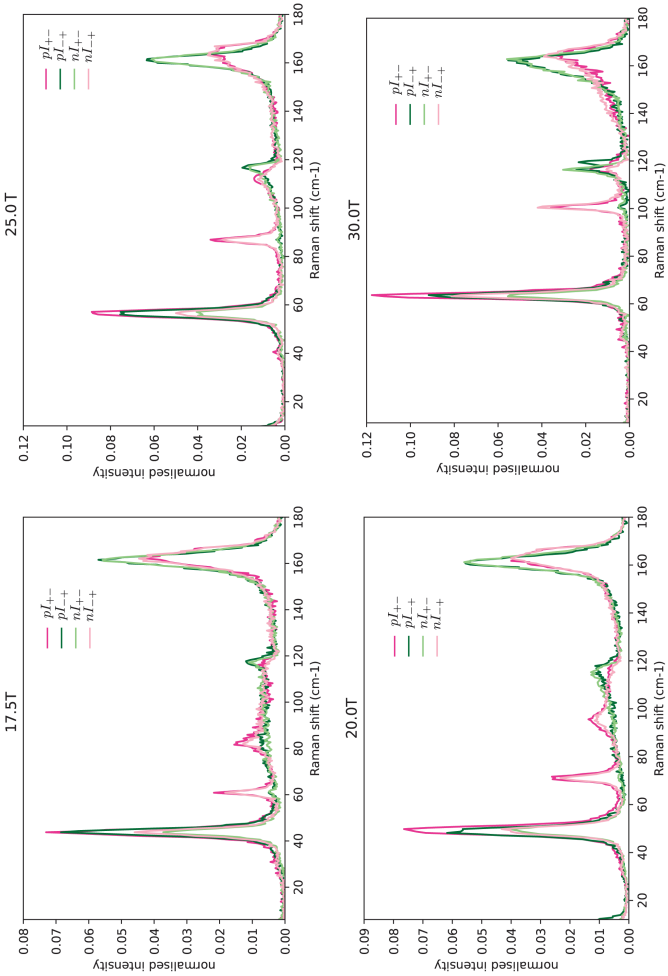

Figure 9.3: plots from all the four channels.

BIBLIOGRAPHY

[1] M. S. Zubairy. A very brief history of light. *Optics in our time*, pages 3–24, 2016.

[2] C. V. Raman and K. S. Krishnan. A new type of secondary radiation. *Nature*, 121(3048):501–502, 1928.

[3] P. W. Anderson. Basic notions of condensed matter physics. *Frontiers in physics*, 55:49, 1984.

[4] P. Coleman. *Introduction to many-body physics*. Cambridge University Press, 2015.

[5] P. W. Anderson. Resonating valence bonds: A new kind of insulator? *Materials Research Bulletin*, 8(2):153–160, 1973. ISSN 0025-5408.

[6] D. A. Huse and V. Elser. Simple variational wave functions for two-dimensional Heisenberg spin-1/2 antiferromagnets. *Physical review letters*, 60(24):2531, 1988.

[7] Z. Zhu and S. R. White. Spin liquid phase of the $s = \frac{1}{2} J_1 - J_2$ Heisenberg model on the triangular lattice. *Physical Review B*, 92(4):041105, 2015.

[8] Z. Zhu, P. A. Maksimov, S. R. White, and A. L. Chernyshev. Topography of spin liquids on a triangular lattice. *Physical review letters*, 120 (20):207203, 2018.

[9] P. W. Anderson. The resonating valence bond state in La_2CuO_4 and superconductivity. *Science*, 235(4793):1196–1198, 1987.

[10] S. A. Kivelson, D. S. Rokhsar, and J. P. Sethna. Topology of the resonating valence-bond state: Solitons and high-T_c superconductivity. *Physical Review B*, 35(16):8865, 1987.

[11] XG Wen. Mean-field theory of spin-liquid states with finite energy gap and topological orders. *Physical Review B*, 44(6):2664, 1991.

[12] R. Moessner, S. L. Sondhi, and E. Fradkin. Short-ranged resonating valence bond physics, quantum dimer models, and Ising gauge theories. *Physical Review B*, 65(2):024504, 2001.

[13] A. Y. Kitaev. Fault-tolerant quantum computation by anyons. *Annals of physics*, 303(1):2–30, 2003.

[14] A. Kitaev. Anyons in an exactly solved model and beyond. *Ann. Phys.*, 321(1):2–111, 2006.

[15] L. Balents, M. P. A. Fisher, and S. M. Girvin. Fractionalization in an easy-axis kagome antiferromagnet. *Physical Review B*, 65(22):224412, 2002.

[16] T. Senthil and O. Motrunich. Microscopic models for fractionalized phases in strongly correlated systems. *Physical Review B*, 66(20):205104, 2002.

[17] O. I. Motrunich and T. Senthil. Exotic order in simple models of bosonic systems. *Physical review letters*, 89(27):277004, 2002.

[18] G. Jackeli and G. Khaliullin. Mott insulators in the strong spin-orbit coupling limit: From Heisenberg to a quantum compass and Kitaev models. *Phys. Rev. Lett.*, 102:017205, Jan 2009.

[19] H. Takagi, T. Takayama, G. Jackeli, G. Khaliullin, and S. E. Nagler. Concept and realization of Kitaev quantum spin liquids. *Nature Reviews Physics*, 1(4):264–280, 2019.

[20] HS Kim, A. Catuneanu, and HY Kee. Kitaev magnetism in honeycomb α-$RuCl_3$ with intermediate spin-orbit coupling. *Physical Review B*, 91 (24):241110, 2015.

[21] HS Kim, V. V. Shankar, A Catuneanu, and HY Kee. Kitaev magnetism in honeycomb α-$RuCl_3$ with intermediate spin-orbit coupling. *Phys. Rev. B*, 91:241110, Jun 2015.

[22] R. D. Johnson, S. C. Williams, A. A. Haghighirad, J. Singleton, V. Zapf, P. Manuel, I. I. Mazin, Y. Li, H. O. Jeschke, R. Valentí, and R. Coldea. Monoclinic crystal structure of α-$RuCl_3$ and the zigzag antiferromagnetic ground state. *Phys. Rev. B*, 92:235119, Dec 2015.

[23] H. B. Cao, A. Banerjee, J.-Q. Yan, C. A. Bridges, M. D. Lumsden, D. G. Mandrus, D. A. Tennant, B. C. Chakoumakos, and S. E. Nagler. Low-temperature crystal and magnetic structure of α-$RuCl_3$. *Phys. Rev. B*, 93:134423, Apr 2016.

[24] A. Banerjee, P. Lampen-Kelley, J. Knolle, C. Balz, A. A. Aczel, B. Winn, Y. Liu, D. Pajerowski, J. Yan, C. A. Bridges, et al. Excitations in the field-induced quantum spin liquid state of α-$RuCl_3$. *npj Quantum Mater.*, 3(1):1–7, 2018.

[25] C. Trebst, S.and Hickey. Kitaev materials. *Physics Reports*, 950:1–37, 2022.

[26] S.-H. Do, S.-Y. Park, J. Yoshitake, J. Nasu, Y.-S. Motome, Y.and Kwon, D. T. Adroja, D. J. Voneshen, K. Kim, T. H. Jang, J. H. Park, K.-Y. Choi, and S. Ji. Majorana fermions in the Kitaev quantum spin system α-$RuCl_3$. *Nat. Phys.*, 13(11):1079–1084, 2017.

[27] S. Widmann, V. Tsurkan, D. A. Prishchenko, V. G. Mazurenko, A. A. Tsirlin, and A. Loidl. Thermodynamic evidence of fractionalized excitations in α-$RuCl_3$. *Physical Review B*, 99(9):094415, 2019.

[28] A. Banerjee, C. A. Bridges, J.-Q. Yan, A. A. Aczel, L. Li, M. B. Stone, G. E. Granroth, M. D. Lumsden, Y. Yiu, J. Knolle, S. Bhattacharjee, D. L. Kovrizhin, R. Moessner, D. A. Tennant, D. G. Mandrus, and S. E. Nagler. Proximate Kitaev quantum spin liquid behaviour in a honeycomb magnet. *Nature materials*, 15(7):733–740, 2016.

[29] A. Banerjee, J. Yan, J. Knolle, C. A. Bridges, M. B. Stone, M. D. Lumsden, D. G. Mandrus, D. A. Tennant, R. Moessner, and S. E. Nagler. Neutron scattering in the proximate quantum spin liquid α-$RuCl_3$. *Science*, 356(6342):1055–1059, 2017.

[30] L. J. Sandilands, Y. Tian, K. W. Plumb, Y.-J. Kim, and K. S. Burch. Scattering continuum and possible fractionalized excitations in α-$RuCl_3$. *Phys. Rev. Lett.*, 114(14):147201, 2015.

[31] J. Nasu, J. Knolle, D. L. Kovrizhin, Y. Motome, and R. Moessner. Fermionic response from fractionalization in an insulating two-dimensional magnet. *Nature Physics*, 12(10):912–915, 2016.

[32] A. N. Ponomaryov, E. Schulze, J. Wosnitza, P. Lampen-Kelley, A. Banerjee, J.-Q. Yan, C. A. Bridges, D. G. Mandrus, S. E. Nagler, A. K. Kolezhuk, and S. A. Zvyagin. Unconventional spin dynamics in the honeycomb-lattice material α-$RuCl_3$: High-field electron spin resonance studies. *Phys. Rev. B*, 96(24):241107, 2017.

[33] Z. Wang, S. Reschke, D. Hüvonen, S.-H. Do, K.-Y. Choi, M. Gensch, U. Nagel, T. Rõõm, and A. Loidl. Magnetic excitations and continuum of a possibly field-induced quantum spin liquid in α-$RuCl_3$. *Phys. Rev. Lett.*, 119(22):227202, 2017.

[34] J. Knolle, D. L. Kovrizhin, J. T. Chalker, and R. Moessner. Dynamics of fractionalization in quantum spin liquids. *Phys. Rev. B*, 92:115127, Sep 2015.

[35] J. Nasu, J. Knolle, D. L. Kovrizhin, Y. Motome, and R. Moessner. Fermionic response from fractionalization in an insulating two-dimensional magnet. *Nat. Phys.*, 12(10):912–915, 2016.

[36] Y. Kasahara, T. Ohnishi, Y. Mizukami, O. Tanaka, S. Ma, K. Sugii, N. Kurita, H. Tanaka, J. Nasu, Y. Motome, T. Shibauchi, and Y. Matsuda. Majorana quantization and half-integer thermal quantum Hall effect in a Kitaev spin liquid. *Nature*, 559(7713):227–231, 2018.

[37] Y. Vinkler-Aviv and A. Rosch. Approximately quantized thermal Hall effect of chiral liquids coupled to phonons. *Phys. Rev. X*, 8:031032, Aug 2018.

[38] M. Ye, G. B. Halász, L. Savary, and L. Balents. Quantization of the thermal hall conductivity at small hall angles. *Physical review letters*, 121(14):147201, 2018.

[39] S. M. Winter, A. A. Tsirlin, M. Daghofer, J. van den Brink, Y. Singh, P. Gegenwart, and R. Valentí. Models and materials for generalized kitaev magnetism. *Journal of Physics: Condensed Matter*, 29(49):493002, 2017.

[40] A. Abragam and B. Bleaney. *Electron paramagnetic resonance of transition ions*. Clarendon P., 1970.

[41] A. J. Browne, A. Krajewska, and A. S. Gibbs. Quantum materials with strong spin–orbit coupling: challenges and opportunities for materials chemists. *Journal of Materials Chemistry C*, 9(35):11640–11654, 2021.

[42] E. V. Stroganov and K. V. Ovchinnikov. Crystal structure of ruthenium trichloride. *Vestn. Leningr. Univ. Fiz. Khim*, 12:152, 1957.

[43] A. Loidl, P. Lunkenheimer, and V. Tsurkan. On the proximate Kitaev quantum-spin liquid α-$RuCl_3$: Thermodynamics, excitations and continua. *Journal of Physics Condensed Matter*, 33(44):1–24, 2021.

[44] T. T. Mai, A. McCreary, P. Lampen-Kelley, N. Butch, J. R. Simpson, J.-Q. Yan, S. E. Nagler, D. Mandrus, A. R. Hight Walker, and R. Valdés Aguilar. Polarization-resolved Raman spectroscopy of α-$RuCl_3$ and evidence of room-temperature two-dimensional magnetic scattering. *Phys. Rev. B*, 100:134419, Oct 2019.

[45] S. Reschke, F. Mayr, Zhe Wang, S.-H. Do, K.-Y. Choi, and A. Loidl. Electronic and phonon excitations in α-$RuCl_3$. *Phys. Rev. B*, 96:165120, Oct 2017.

[46] S-Y Park, S-H Do, K-Y Choi, D Jang, T-H Jang, J Schefer, C-M Wu, JS Gardner, JMS Park, J-H Park, et al. Emergence of the isotropic Kitaev honeycomb lattice with two-dimensional Ising universality in α-$RuCl_3$. *arXiv preprint arXiv:1609.05690*, 2016.

[47] A. Glamazda, P. Lemmens, S.-H. Do, Y. S. Kwon, and K.-Y. Choi. Relation between Kitaev magnetism and structure in α-$RuCl_3$. *Phys. Rev. B*, 95(17):174429, 2017.

[48] J. Wagner, R. B. Sahasrabudhe, A.and Versteeg, L. Wysocki, Z. Wang, V. Tsurkan, D. I. Loidl, A.and Khomskii, H. Hedayat, and P. H. M. van Loosdrecht. Magneto-optical study of metamagnetic transitions in the antiferromagnetic phase of α-$RuCl_3$. *npj Quantum Mater.*, 7(1):28, 2022.

[49] K. W. Plumb, J. P. Clancy, L. J. Sandilands, V. Vijay Shankar, Y. F. Hu, K. S. Burch, Hae-Young Kee, and Young-June Kim. α-$RuCl_3$: A spin-orbit assisted Mott insulator on a honeycomb lattice. *Phys. Rev. B*, 90:041112, Jul 2014.

[50] H. Suzuki, H. Liu, J. Bertinshaw, K. Ueda, H. Kim, S. Laha, D. Weber, Z. Yang, L. Wang, H. Takahashi, K. Fürsich, M. Minola, B. V. Lotsch, B. J. Kim, H. Yavaş, M. Daghofer, J. Chaloupka, G. Khaliullin, H. Gretarsson, and B. Keimer. Proximate ferromagnetic state in the Kitaev model material α-$RuCl_3$. *Nat. Commun.*, 12(1):4512, 2021.

[51] L. Binotto, I. Pollini, and G. Spinolo. Optical and transport properties of the magnetic semiconductor α-$RuCl_3$. *physica status solidi (b)*, 44 (1):245–252, 1971.

[52] P. Warzanowski, N. Borgwardt, K. Hopfer, J. Attig, T. C. Koethe, P. Becker, V. Tsurkan, A. Loidl, M. Hermanns, P. H. M. van Loosdrecht, and M. Grüninger. Multiple spin-orbit excitons and the electronic structure of α-$RuCl_3$. *Physical Review Research*, 2(4):042007, 2020.

[53] J. A. Sears, M. Songvilay, K. W. Plumb, J. P. Clancy, Y. Qiu, Y. Zhao, D. Parshall, and Y.-J. Kim. Magnetic order in α-$RuCl_3$: A honeycomb-lattice quantum magnet with strong spin-orbit coupling. *Physical Review B*, 91(14):144420, 2015.

[54] C. Epstein and N. Elliott. Magnetic susceptibilities of K_3MoCl_6 and α-$RuCl_3$. *The Journal of Chemical Physics*, 22(4):634–635

[55] Y. Kubota, H. Tanaka, T. Ono, Y. Narumi, and K. Kindo. Successive magnetic phase transitions in α-$RuCl_3$: XY-like frustrated magnet on the honeycomb lattice. *Phys. Rev. B*, 91(9):094422, 2015.

[56] P. Lampen-Kelley, S. Rachel, J. Reuther, J.-Q. Yan, A. Banerjee, C. A. Bridges, H. B. Cao, S. E. Nagler, and D. Mandrus. Anisotropic susceptibilities in the honeycomb Kitaev system α-$RuCl_3$. *Physical Review B*, 98(10):100403, 2018.

[57] R. Yadav, N. A. Bogdanov, V. M. Katukuri, S. Nishimoto, J. Van Den Brink, and L. Hozoi. Kitaev exchange and field-induced quantum spin-liquid states in honeycomb α-$RuCl_3$. *Scientific reports*, 6(1): 1–16, 2016.

[58] L. Janssen, E. C. Andrade, and M. Vojta. Magnetization processes of zigzag states on the honeycomb lattice: Identifying spin models for α-$RuCl_3$ and Na_2IrO_3. *Physical Review B*, 96(6):064430, 2017.

[59] J. A. Sears, L. E. Chern, S. Kim, P. J. Bereciartua, S. Francoual, Y. B. Kim, and Y.-J. Kim. Ferromagnetic Kitaev interaction and the origin of large magnetic anisotropy in α-$RuCl_3$. *Nat. Phys.*, 16(8):837–840, 2020.

[60] S.-H. Do, S.-Y Park, J. Yoshitake, J. Nasu, Y. Motome, Y.-S. Kwon, D. T. Adroja, D. J. Voneshen, K. Kim, TH Jang, J.-H. Park, K.-Y. Choi, and S. Ji. Majorana fermions in the Kitaev quantum spin system α-$RuCl_3$. *Nat. Phys.*, 13(11):1079–1084, 2017.

[61] C. Balz, L. Janssen, P. Lampen-Kelley, A. Banerjee, Y. H. Liu, J.-Q. Yan, D. G. Mandrus, M. Vojta, and S. E. Nagler. Field-induced intermediate ordered phase and anisotropic interlayer interactions in α-$RuCl_3$. *Phys. Rev. B*, 103:174417, May 2021.

[62] C. Balz, P. Lampen-Kelley, A. Banerjee, Ji. Yan, Z. Lu, X. Hu, S. M. Yadav, Y. Takano, Y. Liu, D. A. Tennant, M. D. Lumsden, D. Mandrus, and S. E. Nagler. Finite field regime for a quantum spin liquid in α-$RuCl_3$. *Phys. Rev. B*, 100(6):060405, 2019.

[63] T. Moriya. Theory of Light Scattering by Magnetic Crystals. *Journal of the Physical Society of Japan*, 23(3):490–500, sep 1967.

[64] H. Kuzmany. *Solid-state spectroscopy: an introduction*. Springer, 2009.

[65] M. S. Dresselhaus, G. Dresselhaus, and A. Jorio. *Group theory: application to the physics of condensed matter*. Springer Science & Business Media, 2007.

[66] B. Perreault, J. Knolle, N. B. Perkins, and F. J. Burnell. Theory of Raman response in three-dimensional Kitaev spin liquids: Application to β- andγ- Li_2IrO_3 compounds. *Physical Review B*, 92(9):094439, 2015.

[67] M. I. Aroyo, J. M. Perez-Mato, D. Orobengoa, E. Tasci, G. de la Flor, and A. Kirov. Crystallography online: Bilbao crystallographic server. *Bulg. Chem. Commun*, 43(2):183–197, 2011.

[68] M. V. Klein. Electronic Raman scattering. *Light Scattering in Solids I: Introductory Concepts*, pages 147–204, 2005.

[69] A. Zawadowski and M. Cardona. Theory of Raman scattering on normal metals with impurities. *Physical Review B*, 42(16):10732, 1990.

[70] Y. S. Ponosov and S. V. Streltsov. Measurements of raman scattering by electrons in metals: The effects of electron-phonon coupling. *Physical Review B*, 86(4):045138, 2012.

[71] Q. Cai, M. Chandrasekhar, H. R Chandrasekhar, U. Venkateswaran, S. H. Liou, and R. Li. Temperature dependence of the Raman scattering in $HgBa_2CuO_{4+\delta}$. *Solid State Communications*, 117(11):685–690, 2001. ISSN 0038-1098.

[72] S. B. Dierker, M. V. Klein, G. W. Webb, and Z. Fisk. Electronic raman scattering by superconducting-gap excitations in Nb_3Sn and V_3Si. *Physical review letters*, 50(11):853, 1983.

[73] P. A. Fleury and R. Loudon. Scattering of light by one- and two-magnon excitations. *Phys. Rev.*, 166:514–530, Feb 1968.

[74] M. G. Cottam and D. J.. Lockwood. Light scattering in magnetic solids. 1986.

[75] M. F. Thorpe. Two-magnon raman scattering and infrared absorption in MnF_2. *Journal of Applied Physics*, 41(3):892–893, 1970.

[76] C. Castellani, F. Leoni, and C. R. Natoli. A study of the two-magnon raman scattering in the heisenberg antiferromagnets CoF_2 and FeF_2 using a realistic model hamiltonian. *Journal of Physics C: Solid State Physics*, 7(7):1353, 1974.

[77] J. Knolle, GW Chern, D. L. Kovrizhin, R. Moessner, and N. B. Perkins. Raman scattering signatures of Kitaev spin liquids in A_2IrO_3 iridates with $a = \mathrm{Na}$ or Li. *Phys. Rev. Lett.*, 113:187201, Oct 2014.

[78] L. D. Barron, L. Hecht, I. H. McColl, and E. W. Blanch. Raman optical activity comes of age. *Mol. Phys.*, 102(8):731–744, 2004.

[79] K. R. Hoffman, D. J. Lockwood, and W. M. Yen. Circular dichroism and Raman optical activity in antiferromagnetic transition-metal fluorides. *Low Temp. Phys.*, 31:786–793, 2005.

[80] A. P. Cracknell. *Magnetism in crystalline materials: applications of the theory of groups of cambiant symmetry*. Elsevier, 2016.

[81] M. De Graef. Visualization of time-reversal symmetry in magnetic point groups. *Metallurgical and Materials Transactions A*, 41:1321–1329, 2010.

[82] M. De Graef. Magnetic point group renderings. URL https://mpg.web.cmu.edu/.

[83] M. Guennou. Introduction to group theory - from an experimentalist's perspective, 2023. URL https://isoe.cnrs.fr/wp-content/uploads/2021/08/Mael-Guennou_ISOE2021_lecture-1.pdf.

[84] C. Bradley and A. Cracknell. *The mathematical theory of symmetry in solids: representation theory for point groups and space groups*. Oxford University Press, 2010.

[85] A. P. Cracknell. Scattering matrices for the Raman effect in magnetic crystals. *Journal of Physics C: Solid State Physics*, 2(3):500, 1969.

[86] E. Anastassakis and E. Burstein. Morphic effects. V. Time reversal symmetry and the mode properties of long wavelength optical phonons. *Journal of Physics C: Solid State Physics*, 5(17):2468, 1972.

[87] B. Huang, J. Cenker, X. Zhang, E. L. Ray, T. Song, T. Taniguchi, K. Watanabe, M. A. McGuire, D. Xiao, and X. Xu. Tuning inelastic light scattering via symmetry control in the two-dimensional magnet CrI_3. *Nature nanotechnology*, 15(3):212–216, 2020.

[88] J. Cenker, B. Huang, N. Suri, P. Thijssen, A. Miller, T. Song, T.and Taniguchi, K. Watanabe, Mi. A. McGuire, D. Xiao, and X Xu. Direct observation of two-dimensional magnons in atomically thin CrI_3. *Nat. Phys.*, 17(1):20–25, 2021.

[89] M. A. Prosnikov, S. N. Barilo, N. A. Liubochko, R. V. Pisarev, and P. C. M. Christianen. High-Field Raman scattering in an antiferromagnet Fe_3BO_6. *Magnetochemistry*, 8(8):77, 2022.

[90] Experimental setup at high field magnet lab. URL https://www.ru.nl/hfml/use-our-facility/experimental-equipment-0/optical-experiments/.

[91] A. Glamazda, P. Lemmens, S.-H. Do, Y. S. Kwon, and K.-Y. Choi. Relation between kitaev magnetism and structure in α-$RuCl_3$. *Phys. Rev. B*, 95:174429, May 2017.

[92] J. M. Binder, A. Stark, N. Tomek, J. Scheuer, F. Frank, K. D. Jahnke, C. Müller, S. Schmitt, M. H. Metsch, T. Unden, T. Gehring, A. Huck, U. L. Andersen, L. J. Rogers, and F. Jelezko. Qudi: A modular python suite for experiment control and data processing. *SoftwareX*, 6:85–90, 2017.

[93] A. Sahasrabudhe, D. A. S. Kaib, S. Reschke, R. German, T. C. Koethe, J. Buhot, D. Kamenskyi, C. Hickey, P. Becker, V. Tsurkan, A. Loidl,

S.H. Do, K.Y. Choi, M. Grüninger, S. M. Winter, Z. Wang, R. Valentí, and P. H. M. van Loosdrecht. High-field quantum disordered state in α-$RuCl_3$: Spin flips, bound states, and multiparticle continuum. *Phys. Rev. B*, 101(14):140410, 2020.

[94] D. Wulferding, Y. Choi, S.-H. Do, C. H. Lee, P. Lemmens, C. Faugeras, Y. Gallais, and K.-Y Choi. Magnon bound states versus anyonic Majorana excitations in the Kitaev honeycomb magnet α-$RuCl_3$. *Nat. Commun.*, 11(1):1–7, 2020.

[95] K. Feng, S. Swarup, and N. B. Perkins. Footprints of Kitaev spin liquid in the Fano lineshape of Raman-active optical phonons. *Physical Review B*, 105(12):L121108, 2022.

[96] Y.-Y. Pai, C. E. Marvinney, M. A. Feldman, B. Lerner, Y. S. Phang, K. Xiao, J. Yan, L. Liang, J. Lapano, M. Brahlek, and B. J. Lawrie. Magnetostriction of α-RuCl3 flakes in the zigzag phase. *The Journal of Physical Chemistry C*, 125(46):25687–25694, 2021.

[97] S. W. Lovesey. Polar magnetism and chemical bond in α-$RuCl_3$. *Journal of Physics: Condensed Matter*, 2022.

[98] V. Reschke, S.and Tsurkan, S.-H. Do, K.-Y. Choi, P. Lunkenheimer, Z. Wang, and Al. Loidl. Terahertz excitations in α-$RuCl_3$: Majorana fermions and rigid-plane shear and compression modes. *Physical Review B*, 100(10):100403, 2019.

[99] G. Blumberg, A. Mialitsin, B. S. Dennis, N. D. Zhigadlo, and J. Karpinski. Multi-gap superconductivity in MgB_2: Magneto-Raman spectroscopy. *Physica C: Superconductivity*, 456(1-2):75–82, 2007.

[100] X. K. Chen, J. C. Irwin, H. J. Trodahl, T. Kimura, and K. Kishio. Investigation of the superconducting gap in $La_{2-x}Sr_xCuO_4$ by Raman spectroscopy. *Physical review letters*, 73(24):3290, 1994.

[101] H. Gretarsson, N. H. Sung, M. Höppner, B. J. Kim, B. Keimer, and M. Le Tacon. Two-magnon Raman scattering and pseudospin-lattice interactions in Sr_2IrO_4 and $Sr_3Ir_2O_7$. *Phys. Rev. Lett.*, 116(13):136401, 2016.

[102] J. Chaloupka and G. Khaliullin. Magnetic anisotropy in the kitaev model systems Na_2IrO_3 and α-$RuCl_3$. *Physical Review B*, 94(6):064435, 2016.

[103] K. Riedl, Y. Li, S. M. Winter, and R. Valentí. Sawtooth torque in anisotropic $j_{\text{eff}} = 1/2$ magnets: Application to α-$RuCl_3$. *Physical Review Letters*, 122(19):197202, 2019.

[104] S. V. Vonsovskii. *Ferromagnetic Resonance: The Phenomenon of Resonant Absorption of a High-Frequency Magnetic Field in Ferromagnetic Substances*. Pergamon, Oxford, 1966.

[105] S. M. Winter, K. Riedl, D. A. S. Kaib, R. Coldea, and R. Valentí. Probing α-$RuCl_3$ beyond magnetic order: Effects of temperature and magnetic field. *Phys. Rev. Lett.*, 120:077203, Feb 2018.

[106] S. M. M Winter, Y. Li, H. O. Jeschke, and R. Valentí. Challenges in design of Kitaev materials: Magnetic interactions from competing energy scales. *Physical Review B*, 93(21):214431, 2016.

[107] HS Kim and HY Kee. Crystal structure and magnetism in α-$RuCl_3$: An ab initio study. *Physical Review B*, 93(15):155143, 2016.

[108] W. Wang, Z.-Y. Dong, S.-L. Yu, and J.-X. Li. Theoretical investigation of magnetic dynamics in α-$RuCl_3$. *Physical Review B*, 96(11):115103, 2017.

[109] Y. S. Hou, H. J. Xiang, and X. G. Gong. Unveiling magnetic interactions of ruthenium trichloride via constraining direction of orbital moments: Potential routes to realize a quantum spin liquid. *Physical Review B*, 96(5):054410, 2017.

[110] A. N. Ponomaryov, L. Zviagina, J. Wosnitza, P. Lampen-Kelley, A. Banerjee, J.-Q. Yan, C. A. Bridges, D. G. Mandrus, S. E. Nagler, and S. A. Zvyagin. Nature of magnetic excitations in the high-field phase of α-$RuCl_3$. *Phys. Rev. Lett.*, 125(3):037202, 2020.

[111] T. Yokoi, S. Ma, Y. Kasahara, S. Kasahara, T. Shibauchi, N. Kurita, H. Tanaka, J. Nasu, Y. Motome, C. Hickey, S. Trebst, and Y. Matsuda. Half-integer quantized anomalous thermal Hall effect in the Kitaev material candidate α-$RuCl_3$. *Science*, 373(6554):568–572, 2021.

[112] M. Yamashita, J. Gouchi, Y. Uwatoko, N. Kurita, and H. Tanaka. Sample dependence of half-integer quantized thermal Hall effect in the Kitaev spin-liquid candidate α-$RuCl_3$. *Phys. Rev. B*, 102(22):220404, 2020.

[113] J. Nasu, J. Yoshitake, and Y. Motome. Thermal transport in the Kitaev model. *Phys. Rev. Lett.*, 119:127204, Sep 2017.

[114] É. Lefrançois, G. Grissonnanche, J. Baglo, P. Lampen-Kelley, J.-Q. Yan, C. Balz, D. Mandrus, S. E. Nagler, S. Kim, Young-June Kim, N. Doiron-Leyraud, and Louis Taillefer. Evidence of a phonon Hall effect in the Kitaev spin liquid candidate α-$RuCl_3$. *Phys. Rev. X*, 12:021025, Apr 2022.

[115] P. Czajka, T. Gao, M. Hirschberger, P. Lampen-Kelley, A. Banerjee, J. Yan, D. G. Mandrus, S. E. Nagler, and N. P. Ong. Oscillations of the

thermal conductivity in the spin-liquid state of α-$RuCl_3$. *Nat. Phys.*, 17 (8):915–919, 2021.

[116] J. A. N. Bruin, R. R. Claus, Y. Matsumoto, N. Kurita, H. Tanaka, and H. Takagi. Robustness of the thermal Hall effect close to half-quantization in α-$RuCl_3$. *Nat. Phys.*, 18(4):401–405, 2022.

[117] S. Gass, P. M. Cônsoli, V. Kocsis, L. T. Corredor, P. Lampen-Kelley, D. G. Mandrus, S. E. Nagler, L. Janssen, M. Vojta, B. Büchner, and A. U. B. Wolter. Field-induced transitions in the Kitaev material α-$RuCl_3$ probed by thermal expansion and magnetostriction. *Phys. Rev. B*, 101(24):245158, 2020.

[118] S. Bachus, D. A. S. Kaib, Y. Tokiwa, A. Jesche, V. Tsurkan, A. Loidl, S. M. Winter, A. A. Tsirlin, R. Valentí, and P. Gegenwart. Thermodynamic perspective on field-induced behavior of α-$RuCl_3$. *Phys. Rev. Lett.*, 125(9):097203, 2020.

[119] R. Schönemann, S. Imajo, F. Weickert, J. Yan, D. G. Mandrus, Y. Takano, E. L. Brosha, P. F. S. Rosa, S. E. Nagler, K. Kindo, and M. Jaime. Thermal and magnetoelastic properties of α-$RuCl_3$ in the field-induced low-temperature states. *Phys. Rev. B*, 102(21):214432, 2020.

[120] S.-H. Baek, S.-H. Do, K.-Y. Choi, Y. S. Kwon, A. U. B. Wolter, S. Nishimoto, J. Van Den Brink, and B. Büchner. Evidence for a field-induced quantum spin liquid in α-$RuCl_3$. *Phys. Rev. Lett.*, 119(3):037201, 2017.

[121] A. Pinczuk, B. S. Dennis, L. N. Pfeiffer, and K. West. Observation of collective excitations in the fractional quantum Hall effect. *Phys. Rev. Lett.*, 70:3983–3986, Jun 1993. doi: 10.1103/PhysRevLett.70.3983.

[122] M. Kang, A. Pinczuk, B. S. Dennis, L. N. Pfeiffer, and K. W. West. Observation of multiple magnetorotons in the fractional quantum Hall effect. *Phys. Rev. Lett.*, 86:2637–2640, Mar 2001.

[123] A. R. Goñi, A. Pinczuk, J. S. Weiner, B. S. Dennis, L. N. Pfeiffer, and K. W. West. Observation of magnetoplasmons, rotons, and spin-flip excitations in GaAs quantum wires. *Phys. Rev. Lett.*, 70:1151–1154, Feb 1993.

[124] D. X. Nguyen and D. T. Son. Probing the spin structure of the fractional quantum Hall magnetoroton with polarized Raman scattering. *Phys. Rev. Research*, 3:023040, Apr 2021.

[125] S.-F. Liou, F. D. M. Haldane, K. Yang, and E. H. Rezayi. Chiral gravitons in fractional quantum Hall liquids. *Phys. Rev. Lett.*, 123:146801, Sep 2019.

[126] C. Chen, X. Chen, B. Deng, K. Watanabe, T. Taniguchi, S. Huang, and F. Xia. Probing interlayer interaction via chiral phonons in layered honeycomb materials. *Phys. Rev. B*, 103:035405, Jan 2021.

[127] T. Zhang and S. Murakami. Chiral phonons and pseudoangular momentum in nonsymmorphic systems. *Phys. Rev. Research*, 4:L012024, Feb 2022.

[128] K. Jenni, S. Kunkemöller, W. Schmidt, P. Steffens, A. A. Nugroho, and M. Braden. Chirality of magnetic excitations in ferromagnetic $SrRuO_3$. *Phys. Rev. B*, 105:L180408, May 2022.

[129] R. Hisatomi, A. Noguchi, R. Yamazaki, Y. Nakata, A. Gloppe, Y. Nakamura, and K. Usami. Helicity-changing brillouin light scattering by magnons in a ferromagnetic crystal. *Phys. Rev. Lett.*, 123:207401, Nov 2019.

[130] B.B. Lyu, Y.F. Gao, Y. Zhang, L. Wang, Xi. Wu, Yani Chen, J. Zhang, G. Li, Q. Huang, N. Zhang, Y. Chen, J. Mei, H. Yan, Y. Zhao, L. Huang, and M. Huang. Probing the ferromagnetism and spin wave gap in VI_3 by helicity-resolved Raman spectroscopy. *Nano Letters*, 20(8):6024–6031, 2020.

[131] D. G. Joshi. Topological excitations in the ferromagnetic Kitaev-Heisenberg model. *Phys. Rev. B*, 98:060405, Aug 2018. doi: 10.1103/PhysRevB.98.060405.

[132] P. A. McClarty, XY Dong, M. Gohlke, J. G. Rau, F. Pollmann, R. Moessner, and K. Penc. Topological magnons in Kitaev magnets at high fields. *Phys. Rev. B*, 98:060404, Aug 2018. doi: 10.1103/PhysRevB.98.060404.

[133] L. E. Chern, E. Z. Zhang, and Y. B. Kim. Sign structure of thermal Hall conductivity and topological magnons for in-plane field polarized Kitaev magnets. *Phys. Rev. Lett.*, 126:147201, Apr 2021.

[134] M.l A. Sahasrabudhe, A.and Prosnikov, T. C. Koethe, P. Stein, V. Tsurkan, A. Loidl, M. Grüninger, H. Hedayat, and P. H. M. van Loosdrecht. Chiral excitations and the intermediate-field regime in the kitaev magnet α-$RuCl_3$. *Phys. Rev. Res.*, 6, Apr 2024.

[135] L. Zhang and Q. Niu. Chiral phonons at high-symmetry points in monolayer hexagonal lattices. *Physical review letters*, 115(11):115502, 2015.

[136] H. Chen, W. Zhang, Q. Niu, and L. Zhang. Chiral phonons in two-dimensional materials. *2D Materials*, 6(1):012002, 2018.

[137] H. Rostami, F. Guinea, and E. Cappelluti. Strain-driven chiral phonons

in two-dimensional hexagonal materials. *Physical Review B*, 105(19): 195431, 2022.

[138] E. V. Cui, J.and Boström, M. Ozerov, F. Wu, Q. Jiang, J.-H. Chu, C. Li, F. Liu, X. Xu, A. Rubio, and Q. Zhang. Chirality selective magnon-phonon hybridization and magnon-induced chiral phonons in a layered zigzag antiferromagnet. *Nature Communications*, 14(1):3396, 2023.

[139] U. Fano. Effects of configuration interaction on intensities and phase shifts. *Physical review*, 124(6):1866, 1961.

[140] A. Wysmołek, D. Plantier, M. Potemski, T. Słupiński, and Z. R. Żytkiewicz. Coupled plasmon–lo-phonon modes at high-magnetic fields. *Physical Review B*, 74(16):165206, 2006.

[141] S. Liu, A. G. Del Águila, D. Bhowmick, C. K. Gan, T. T. H. Do, M. A. Prosnikov, D. Sedmidubskỳ, Z. Sofer, P. C. M. Christianen, P. Sengupta, and Q. Xiong. Direct observation of magnon-phonon strong coupling in two-dimensional antiferromagnet at high magnetic fields. *Physical Review Letters*, 127(9):097401, 2021.

[142] T. T. Mai, K. F. Garrity, A. McCreary, J. Argo, J. R Simpson, V. Doan-Nguyen, R. V. Aguilar, and A. R. H. Walker. Magnon-phonon hybridization in 2d antiferromagnet $MnPSe_3$. *Science advances*, 7(44):eabj3106, 2021.

[143] J. Luo, S. Li, Z. Ye, H. Xu, R.and Yan, J. Zhang, G. Ye, L. Chen, D. Hu, X. Teng, et al. Evidence for topological magnon–phonon hybridization in a 2D antiferromagnet down to the monolayer limit. *Nano Letters*, 23 (5):2023–2030, 2023.

[144] C. Caloz, A. Alu, S. Tretyakov, D. Sounas, K. Achouri, and Z.L. Deck-Léger. Electromagnetic nonreciprocity. *Physical Review Applied*, 10(4): 047001, 2018.

[145] O. Sigwarth and C. Miniatura. Time reversal and reciprocity. *AAPPS Bulletin*, 32(1):23, 2022.

[146] S. Bordács, I. Kézsmárki, D. Szaller, L. Demkó, N. Kida, H. Murakawa, Y. Onose, R. Shimano, T. Rõõm, U. Nagel, S. Miyahara, N. Furukawa, and Y. Tokura. Chirality of matter shows up via spin excitations. *Nat. Phys.*, 8(10):734–738, 2012. doi: 10.1038/nphys2387.

[147] S. Bordács, V. Kocsis, Y. Tokunaga, U. Nagel, T. Rõõm, Y. Takahashi, Y. Taguchi, and Y. Tokura. Unidirectional terahertz light absorption in the pyroelectric ferrimagnet $CaBaCo_4O_7$. *Physical Review B*, 92(21): 214441, 2015.

[148] I. Kézsmárki, N. Kida, H. Murakawa, S. Bordács, Y. Onose, and Y. Tokura. Enhanced directional dichroism of terahertz light in resonance with magnetic excitations of the multiferroic $Ba_2CoGe_2O_7$ oxide compound. *Physical review letters*, 106(5):057403, 2011.

[149] M. O. Yokosuk, H. S. Kim, K. D. Hughey, J. Kim, A. V. Stier, K. R. O'Neal, J. Yang, S. A Crooker, K. Haule, SW Cheong, D Vanderbilt, and J. L. Musfeldt. Nonreciprocal directional dichroism of a chiral magnet in the visible range. *npj quantum materials*, 5(1):20, 2020.

[150] M. Saito, K. Ishikawa, K. Taniguchi, and T. Arima. Magnetic control of crystal chirality and the existence of a large magneto-optical dichroism effect in CuB_2O_4. *Physical review letters*, 101(11):117402, 2008.

[151] T-H Arima. Magneto-electric optics in non-centrosymmetric ferromagnets. *Journal of Physics: Condensed Matter*, 20(43):434211, 2008.

[152] S. Toyoda, N. Abe, S. Kimura, Y. H. Matsuda, T. Nomura, A. Ikeda, S. Takeyama, and T. Arima. One-way transparency of light in multiferroic CuB_2O_4. *Physical review letters*, 115(26):267207, 2015.

[153] P. Czajka, T. Gao, M. Hirschberger, P. Lampen-Kelley, A. Banerjee, N. Quirk, D. G. Mandrus, S. E. Nagler, and N. P. Ong. The planar thermal Hall conductivity in the Kitaev magnet α-$RuCl_3$. 2022.

[154] S. M. Winter, K. Riedl, P.l A. Maksimov, A. L. Chernyshev, A. Honecker, and R. Valentí. Breakdown of magnons in a strongly spin-orbital coupled magnet. *Nat. Commun.*, 8(1):1152, 2017.

[155] P. A. Maksimov and A. L. Chernyshev. Rethinking α-$RuCl_3$. *Phys. Rev. Research*, 2:033011, Jul 2020.

[156] S. Sekh and I. Mandal. Circular dichroism as a probe for topology in three-dimensional semimetals. *Physical Review B*, 105(23):235403, 2022.

[157] A. Chacón, D. Kim, W. Zhu, S. P. Kelly, A. Dauphin, E. Pisanty, A. S. Maxwell, A. Picón, M. F. Ciappina, D. E. Kim, et al. Circular dichroism in higher-order harmonic generation: Heralding topological phases and transitions in chern insulators. *Physical Review B*, 102(13):134115, 2020.

[158] M. Schüler, U. De Giovannini, H. Hübener, A. Rubio, M. A. Sentef, and P. Werner. Local berry curvature signatures in dichroic angle-resolved photoelectron spectroscopy from two-dimensional materials. *Science advances*, 6(9):eaay2730, 2020.

[159] E. V. Boström, T. S. Parvini, J. W McIver, A. Rubio, S. V. Kusminskiy, and M. A. Sentef. Direct optical probe of magnon topology in two-dimensional quantum magnets. *Physical Review Letters*, 130(2):026701, 2023.

Acknowledgements

"During a PhD, you are thrown into cold, deep waters; you either swim or you drown," a wise friend told me when I started.

First and foremost, I am deeply grateful to my advisor, Paul H. M. van Loosdrecht, who not only challenged me to take on this adventure but also ensured that I remained afloat with his invaluable guidance, support, and unwavering commitment throughout this research endeavor. His expertise, insightful feedback, and encouragement have been essential in shaping the direction of this work.

I would like to acknowledge Prof. Dr. Fulvio Parmigiani and Prof. Dr. Peter Schilke for agreeing to be part of my thesis committee. I extend my thanks to Dr. Evgeny Mashkovich for agreeing to take the role of minutes taker.

I would like to thank Prof. Dr. Vladimir Tsurkan, Prof. Dr. Alois Loidl, and Prof. Dr. Petra Becker-Bohatý for providing high-quality samples.

I am also profoundly thankful to my collaborators from the high magnetic field labs, Mikhail Prosnikov (HFML), Jonathan Buhot (HFML), and Clément Faugeras (LNCMI), for their expertise with the magnetic field setup. I would especially like to acknowledge Mikhail for being patient with the experimental proposal we came up with. Due to travel bans, he single-handedly performed the experiment that collected more than half the data presented in this thesis. I am indebted to you for all your support and cooperation.

I would like to sincerely thank my theory collaborators, Prof. Dr. Roser Valentí, David Kaib, Ciaran Hickey, and Aprem Joy, for always entertaining my queries.

Special thanks to Zhe Wang, Hamoon Hedayat, Thomas Koethe, and Markus Gruninger for their invaluable guidance. A special note of thanks to Hamoon for his enthusiasm towards the project, which always uplifted me and rekindled my appreciation for the complex and controversial material at hand.

I would like to extend my gratitude to Vivek Lohani, Philipp Stein, and Hamoon Hedayat for their meticulous proofreading of many parts of my thesis. Any remaining errors or typos are entirely my responsibility, as I am confident they were identified and pointed out by these diligent reviewers.

I would also like to specially thank Dr. Petra Neubauer for helping me sail through the tough times with the visa office. Kind thanks to our secretaries for being patient with me – Claudia Hazel, Charlie, and Britta Schulz.

I would like to acknowledge the assistance and friendship of my fellow graduate students, Philipp (Stein), Marco, Alessandro, Rolf, Philipp (Warzanowski), Lin, and Vivek. Their camaraderie made the academic journey more enjoyable.

I thank all the current and past group members of the OCMS group for creating a kind working environment.

I must especially mention my friends Mugdha, Tushar, and Sagar, who have been constants since my Bachelor's days. They have formed a significant support group for venting about general PhD stress, traveling around Europe, and discussing "Cryo-EM." I owe a profound debt of gratitude to my parents, Sangeeta and Anil, my sister Ankita, and her husband Jay for their unwavering support and encouragement. Their faith in me, even during the most challenging times, has been a great source of inspiration. Lastly, I am grateful to my time at the university for introducing me to my wonderful partner, Vivek.

This thesis represents the culmination of a collective effort, and I am deeply grateful to all those who have been a part of this endeavor. Thank you for helping me traverse the deep waters while making it a cherished memory!

Erklärung zur Dissertation

„Hiermit versichere ich an Eides statt, dass ich die vorliegende Dissertation selbstständig und ohne die Benutzung anderer als der angegebenen Hilfsmittel und Literatur angefertigt habe. Alle Stellen, die wörtlich oder singemäß aus veröffentlichten und nicht veröffentlichten Werken dem Wortlaut oder dem Sinn nach entnommen wurden, sind als solche kenntlich gemacht. Ich versichere an Eides statt, dass diese Dissertation noch keiner anderen Fakultät oder Universität zur Prüfung vorgelegen hat; dass sie - abgesehen von unten angegebenen Teilpublikationen und eingebundenen Artikeln und Manuskripten - noch nicht veröffentlicht worden ist sowie, dass ich eine Veröffentlichung der Dissertation vor Abschluss der Promotion nicht ohne Genehmigung des Promotionsausschusses vornehmen werde. Die Bestimmungen dieser Ordnung sind mir bekannt. Darüber hinaus erkläre ich hiermit, dass ich die Ordnung zur Sicherung guter wissenschaftlicher Praxis und zum Umgang mit wissenschaftlichem Fehlverhalten der Universität zu Köln gelesen und sie bei der Durchführung der Dissertation zugrundeliegenden Arbeiten und der schriftlich verfassten Dissertation beachtet habe und verpflichte mich hiermit, die dort genannten Vorgaben bei allen wissenschaftlichen Tätigkeiten zu beachten und umzusetzen. Ich versichere, dass die eingereichte elektronische Fassung der eingereichten Druckfassung vollständig entspricht."

Teilpublikationen

- **A. Sahasrabudhe**, D. A. S. Kaib, S. Reschke, R. German, T. C. Koethe, J. Buhot, D. Kamenskyi, C. Hickey, P. Becker, V. Tsurkan, A. Loidl, S. H. Do, K. Y. Choi, M. Grüninger, S. M. Winter, Zhe Wang, R. Valentí, and P. H. M. van Loosdrecht Phys. Rev. B 101, 140410(R) (2020)
- **A. Sahasrabudhe**, M. A. Prosnikov, T. C. Koethe, P. Stein, V. Tsurkan, A. Loidl, M. Grüninger, H. Hedayat, and P. H. M. van Loosdrecht Phys. Rev. Research 6, L022005 (2024)

Anuja Sahasrabudhe

Köln, den 5.07.2024

Finding new phases of matter elucidates fundamental physical principles and unlocks novel properties that can lead to groundbreaking technologies. In this thesis, we explore the material α-$RuCl_3$, which has the potential to stabilize the highly sought-after Kitaev Quantum Spin Liquid phase, despite its known magnetic order at low temperatures. Using the century-old technique of Raman scattering as our probe, we sweep the magnetic field to suppress the magnetic order and discover an unconventional paramagnetic phase. This field-induced phase exhibits a rich Raman spectrum, with chiral and non-reciprocal magnetic and phononic excitations.